

# Time- and Temperature-Dependent Failures of a Bonded Joint

Sangwook Sih  
Yasushi Miyano  
Stephen W. Tsai  
*Stanford University  
Palo Alto, California*

NREL technical monitor: Gunjit S. Bir



National Renewable Energy Laboratory  
1617 Cole Boulevard  
Golden, Colorado 80401-3393  
A national laboratory of the U.S. Department of Energy  
Managed by Midwest Research Institute  
for the U.S. Department of Energy  
under contract No. DE-AC36-83CH10093

Work performed under  
Subcontract No. XAF-4-14076-01

July 1997

## NOTICE

This report was prepared as an account of work sponsored by an agency of the United States government. Neither the United States government nor any agency thereof, nor any of their employees, makes any warranty, express or implied, or assumes any legal liability or responsibility for the accuracy, completeness, or usefulness of any information, apparatus, product, or process disclosed, or represents that its use would not infringe privately owned rights. Reference herein to any specific commercial product, process, or service by trade name, trademark, manufacturer, or otherwise does not necessarily constitute or imply its endorsement, recommendation, or favoring by the United States government or any agency thereof. The views and opinions of authors expressed herein do not necessarily state or reflect those of the United States government or any agency thereof.

Available to DOE and DOE contractors from:  
Office of Scientific and Technical Information (OSTI)  
P.O. Box 62  
Oak Ridge, TN 37831  
Prices available by calling (423) 576-8401

Available to the public from:  
National Technical Information Service (NTIS)  
U.S. Department of Commerce  
5285 Port Royal Road  
Springfield, VA 22161  
(703) 487-4650



## Foreword

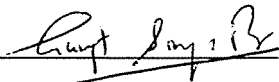
The National Wind Technology Center of the National Renewable Energy Laboratory (NREL) supports university research projects that advance wind turbine technology and provide designers with state-of-the-art analytical tools for design and analyses. This report covers Stanford University's first year effort on modeling of time-temperature-dependent behavior of tubular lap-bonded joints and formulation of a new fatigue life estimation technique.

Wind turbine designers are increasingly using composite materials to manufacture rotor blades since these materials offer excellent engineering advantages. The blades frequently operate in a complex aerodynamic environment and are subjected to severe dynamic loads. The composite-blade-to-metallic-hub interface provides the only loads transmittal path from blades to the electric generator and the rest of the wind turbine structure. This interface, usually a bonded surface joint, bears all the fluctuating bending, torsional, and axial loads over a broad frequency spectrum and over varying temperature and humidity conditions. The design of a long-fatigue-life bonded joint is a challenging problem and a topic of intense research. Researchers at the Stanford University elected to combine the time-temperature equivalence and the residual strength degradation models to estimate the fatigue life of a bonded joint under specified load and temperature variations.

The validity of the proposed fatigue life prediction methodology depends on its success in actual applications. We encourage wind turbine designers and researchers to try this methodology and provide us with their feedback. This will help the researchers in evaluating and perfecting the proposed bonded-joint life prediction techniques.

The authors deserve commendation for their broad-range effort covering new fabrication techniques, extensive study of viscoelastic behavior of adhesive materials, and formulation of fatigue life prediction techniques.

NREL and the U.S. Department of Energy are proud to support high-quality research activities represented by this report.



---

Gunjit S. Bir, Ph.D.

NREL Technical Monitor

## Abstract

This report covers time- and temperature-dependent behaviors of a tubular lap bonded joint to provide a design methodology for windmill blade structures. The tubular joint bonds a cast-iron rod and a GFRP composite pipe together with an epoxy type of an adhesive material containing chopped glass fibers. We proposed a new fabrication method to make concentric and void-less specimens of the tubular lap joint with a thick adhesive bondline in order to simulate the root bond of a blade.

For a better understanding of the behavior of the bonded joint, we studied viscoelastic behavior of the adhesive materials by measuring creep compliance of this adhesive material at several temperatures during loading period. We observed that the creep compliance depends highly on the period of loading and the temperature. We applied time-temperature equivalence of the viscoelastic property to the creep compliance of the adhesive material to obtain time-temperature shift factors.

We also performed constant-rate of monotonically increased uniaxial tensile tests to measure static strength of the tubular lap joint at several temperatures and different strain-rates. Two failure modes were observed from load-deflection curves and failed specimens. One is the brittle mode, which was caused by weakness of the interfacial strength occurring at low temperature and short period of loading. The other is the ductile mode, which was caused by weakness of the adhesive material at high temperature and long period of loading. Transition from the brittle mode of failure to the ductile mode of failure appeared as the temperature or the loading period increased.

We also performed fatigue tests by applying uniaxial tensile-tensile cyclic loadings to measure fatigue strength of the bonded joint at several temperatures, frequencies and stress ratios, and to show their dependency. The fatigue data are analyzed statistically by applying the residual strength degradation model to calculating residual strength and statistical distribution of the fatigue life. Combining the time-temperature equivalence and the residual strength degradation model enables us to estimate the fatigue life of the bonded joint at any load levels at any frequency and temperature with a certain probability. A numerical example shows how to apply the life estimation method to a structure subjected to an arbitrary load history by using rainflow cycle counting.

# Contents

<b>List of Symbols</b>	<b>x</b>
<b>1 Introduction</b>	<b>1</b>
1.1 Structural assembly . . . . .	1
1.2 Bonded joint . . . . .	1
1.3 Previous work on bonded joints . . . . .	3
1.4 Theory of viscoelasticity . . . . .	4
1.5 Life estimation of bonded joints . . . . .	4
<b>2 Fabrication of tubular lap bonded joints</b>	<b>6</b>
2.1 Problem statement . . . . .	6
2.2 Tubular lap joint . . . . .	6
2.3 Configuration of tubular lap joint . . . . .	8
2.4 Surface treatment of cast-iron rod . . . . .	10
2.5 Fabrication of tubular lap joint . . . . .	11
2.6 Testing configuration . . . . .	14
<b>3 Creep compliance of adhesive materials</b>	<b>17</b>
3.1 Problem statement . . . . .	17
3.2 Time-temperature equivalence and time-temperature shift factor . . . . .	18
3.2.1 Time-temperature equivalence . . . . .	18
3.2.2 Time-temperature shift factor . . . . .	20
3.3 Test condition for creep compliance of adhesive material . . . . .	22

3.4	Test results . . . . .	23
3.4.1	Creep compliance of adhesive material . . . . .	23
3.4.2	Master curves of creep compliance and time-temperature shift factor . . . . .	26
3.5	Conclusion . . . . .	30
<b>4</b>	<b>Static failures of bonded joints</b>	<b>31</b>
4.1	Problem statement . . . . .	31
4.2	Test conditions . . . . .	32
4.3	Test results . . . . .	32
4.3.1	Load versus deflection . . . . .	32
4.3.2	Failure modes . . . . .	35
4.3.3	Static strength . . . . .	38
4.3.4	Master curve of static strength . . . . .	39
4.3.5	Time-temperature shift factor . . . . .	44
4.4	Conclusion . . . . .	46
<b>5</b>	<b>Fatigue failures of bonded joints</b>	<b>47</b>
5.1	Problem statement . . . . .	47
5.2	Cyclic loading . . . . .	47
5.3	Statistical analysis of fatigue data . . . . .	49
5.3.1	Residual strength degradation model . . . . .	49
5.3.2	Determination of $c$ , $b$ , $K$ . . . . .	54
5.4	Test conditions . . . . .	56
5.5	Test results . . . . .	58
5.5.1	Failure modes . . . . .	58
5.5.2	Fatigue strength and S-N curve . . . . .	59
5.5.3	Dependence of fatigue strength . . . . .	60
5.5.4	Scatter of fatigue data . . . . .	65
5.5.5	Statistical distribution of fatigue data . . . . .	68
5.6	Conclusion . . . . .	73

<b>6</b>	<b>Life estimation of bonded joints</b>	<b>74</b>
6.1	Problem statement . . . . .	74
6.2	Assumptions . . . . .	76
6.3	Master curve of fatigue strength at $R_\sigma = 0$ . . . . .	77
6.4	Cumulative damage law . . . . .	83
6.5	Master curve of creep strength . . . . .	87
6.6	Dependence on stress ratio . . . . .	90
6.7	Summary . . . . .	93
6.8	Conclusion . . . . .	95
<b>7</b>	<b>Examples</b>	<b>96</b>
7.1	Problem statement . . . . .	96
7.2	Rainflow cycle counting . . . . .	96
7.3	A numerical example . . . . .	98
<b>A</b>	<b>Viscoelasticity</b>	<b>103</b>
A.1	Three descriptions of mechanical behavior . . . . .	103
A.2	Thermoviscoelasticity . . . . .	108
<b>B</b>	<b>Rainflow counting</b>	<b>111</b>
	<b>Bibliography</b>	<b>116</b>

# List of Tables

3.1	Time-temperature shift factors of adhesive materials. . . . .	26
3.2	Activation energy of the adhesive materials cured under three different conditions. . . . .	28
4.1	Time-temperature shift factors of static strength of bonded joints. . .	44
4.2	Activation energies of static strength of bonded joints and of creep compliance of adhesive material. . . . .	45
5.1	Test conditions and number of specimens for tests under cyclic loadings.	58
5.2	Constants, $c$ , $b$ and $K$ . . . . .	59
7.1	Three cycles after rainflow cycles counting. . . . .	102



# List of Figures

1.1	Joints in structural assembly. . . . .	2
2.1	Various types of bonded joints: Only tensile load is applicable to single and double lap joints, whereas tensile, compressive, and torsional loads are applicable to tubular lap joints. . . . .	7
2.2	Cross section of tubular lap bonded joint made of two adherends (a cast-iron rod and a GFRP composite pipe) and adhesive material: Surface of the cast-iron rod is coated with a primer material to increase bonding strength between the cast-iron rod and the adhesive material. . . . .	9
2.3	Variation of tensile static strength by surface treatment methods: Primer material is coated on surface of cast-iron rod by painting method and spraying method at spraying rates of 0.033 <i>gram/rev</i> and 0.085 <i>grams/rev</i> , respectively. . . . .	12
2.4	Molds and materials for fabrication of a bonded joint: The molds were designed to achieve a concentric alignment and a uniform thickness of a thick adhesive layer. . . . .	13
2.5	Configuration for tensile type of tests: Screwed ends of test specimen were held by grips of the testing machine. Displacements were recorded accurately by an extensometer that was attached to the GFRP pipe and a steel ring. . . . .	15
2.6	Load versus displacement curves of uni-axial tensile loadings when the displacements were measured with and without an extensometer. . . . .	16
3.1	Creep compliance curves for test data on measured time scale ( $t$ ), and a master curve at a reference temperature ( $T_0$ ) on shifted time scale ( $t'$ ). . . . .	19

3.2	A typical plot of time-temperature shift factors as a function of temperature. . . . .	20
3.3	Dimensions of an adhesive panel, and a testing fixture for performing three-point bending tests to measure deflection history under a constant loading. . . . .	24
3.4	Curves of creep compliance of adhesive materials ( $D_c$ ) on logged time scale ( $t$ ) at six temperatures during 20 hours. . . . .	25
3.5	Master curves of creep compliance of adhesive materials on shifted time scale ( $t'$ ) at a reference temperature ( $T_o = 40^\circ\text{C}$ ), drawn by shifting the creep compliance curves at elevated temperatures in Figure 3.4. .	27
3.6	Three master curves of creep compliance of adhesive materials under three curing conditions, Cure I, Cure II and Cure III. . . . .	28
3.7	Time-temperature shift factor of adhesive materials and their fitted lines with inflection points near the glass-transition temperature ( $T_g$ ). .	29
4.1	Configuration for static tests under a constant rate of monotonically increased uni-axial tensile loading: Both ends of the test specimen were screwed and held by grips of an Instron-type test machine. . . . .	33
4.2	Load-deflection curves under uni-axial tensile loadings at five temperatures and three strain-rates. . . . .	34
4.3	Two types of failure (brittle failure and ductile failure) categorized by load-deflection curves under static loadings. . . . .	35
4.4	A typical test specimen failed in brittle mode: Little adhesive material remained on the surface of cast-iron rod, while most adhesive material remained intact on the inner surface of GFRP pipe. . . . .	36
4.5	A typical test specimen failed in ductile mode: Most areas on the surface of cast-iron rod were covered by the adhesive material. . . . .	37
4.6	Temperature-dependent static strength of the bonded joints at three strain-rates: Empty dots and solid dots indicate the brittle failure and the ductile failure, respectively. . . . .	40

4.7	Time-dependent static strength of the bonded joints at five temperatures: Empty dots and solid dots indicate the brittle failure and the ductile failure, respectively. . . . .	41
4.8	Averages and scatters of static strength data versus original and shifted time to failure. A reference temperature was set to 40°C. . . . .	42
4.9	Average static strength versus shifted time to failure at a reference temperature (40°C): Master curves were drawn for the ductile failure. . . . .	43
4.10	Solid lines represent the time-temperature shift factors of static strength of bonded joints, whereas dotted lines represent the time-temperature shift factors of creep compliance of AM. . . . .	45
5.1	Cyclic loadings at various stress ratios ( $R_\sigma$ ). . . . .	48
5.2	A static loading as a special case of a fatigue loading at $R_\sigma = 0$ and $N_f = 1/2$ . . . . .	49
5.3	Configuration for fatigue tests under uni-axial tensile-tensile cyclic loading: Both ends of test specimen were screwed and held by grips of a Servo-pulsar testing machine. . . . .	57
5.4	Fatigue test data in Series I: At five temperatures from 40°C to 80°C with 10°C increments at a high frequency ( $f = 5$ Hz) and a low stress ratio ( $R_\sigma = 0.05$ ). . . . .	61
5.5	Fatigue test data in Series II: At two temperatures (40°C and 70°C) at $f = 5$ Hz and a high stress ratio ( $R_\sigma = 0.5$ ). . . . .	62
5.6	Fatigue test data in Series III: At two temperatures (40°C and 70°C) at $f = 5$ Hz and a high stress ratio ( $R_\sigma = 0.95$ ). . . . .	63
5.7	Fatigue test data in Series IV: At one temperature (61.9°C) at a low frequency ( $f = 0.05$ Hz), and $R_\sigma = 0.05$ . . . . .	63
5.8	Temperature-dependent behavior of fatigue strength of bonded joints. . . . .	64
5.9	Frequency-dependent behavior of fatigue strength of bonded joints. . . . .	65
5.10	Average fatigue strength versus time to fatigue failure at $f = 5$ Hz, $R_\sigma = 0.5$ and two temperatures (40°C and 70°C). . . . .	66

5.11	Measured static strength and equivalent static strength calculated from fatigue data at five temperatures from 40°C to 80°C at $f = 5$ Hz and $R_\sigma = 0.05$ . . . . .	67
5.12	Statistical distribution of measured static strength. . . . .	70
5.13	Statistical distributions of fatigue life at five temperatures from 40°C to 80°C at $f = 5$ Hz and $R_\sigma = 0.05$ . . . . .	71
5.14	Weibull distribution of measured static strength and equivalent static strength calculated from fatigue data at five temperatures from 40°C to 80°C at $f = 5$ Hz and $R_\sigma = 0.05$ . . . . .	72
6.1	Fatigue strengths of bonded joint on original and shifted time scale at five temperatures at a high frequency ( $f = 5$ Hz) and a low stress ratio ( $R_\sigma = 0.05$ ). . . . .	78
6.2	Test data of fatigue strengths of bonded joint on shifted time scale at five temperatures at a high frequency ( $f = 5$ Hz) and a low stress ratio ( $R_\sigma = 0.05$ ). . . . .	80
6.3	Master curve of fatigue strength at $R_\sigma = 0.05(\approx 0)$ at a reference temperature ( $T_o = 40^\circ\text{C}$ ). . . . .	81
6.4	Comparison of estimated and experimental K-S-N curves: The estimated curve is drawn from master curve of fatigue strength at zero stress ratio in Figure 6.3. . . . .	82
6.5	Linear cumulative damage law for a linearly increased static load. . .	85
6.6	Modification of linear cumulative damage law for a nonlinearly increased static load. . . . .	88
6.7	Master curve of creep strength at a reference temperature ( $T_o = 40^\circ\text{C}$ ). This master curve is estimated from master curve of static strength by cumulative damage law. A modification in the cumulative damage law makes better agreement with the experimental data at 70°C. . . . .	89
6.8	Estimated S-N curves drawn by Eq. (6.17) at $R_\sigma = 0.5$ for two temperatures, $T = 40^\circ\text{C}$ and $70^\circ\text{C}$ . . . . .	92
6.9	Flow chart for the fatigue life estimation method of bonded joints. . .	94
7.1	An irregular load history. . . . .	97

7.2	A sample of a load block and rainflow cycle counting. . . . .	99
7.3	An Example of rainflow cycle counting. . . . .	100
7.4	Master curve of fatigue strength at zero stress ratio. Solid dots correspond points where $N_f = t'_f$ at $f = 1$ Hz. . . . .	101
7.5	Three S-N curves at three stress ratio ( $R_\sigma = 0, 0.5, 1$ ) that are estimated for a case at $T = 40^\circ\text{C}$ and $f = 1$ Hz. At each stress ratio, we can obtain lives ( $N_f$ ) of rainflow-counted cycles during a load block. .	101
A.1	Comparison of strain response for elastic, viscous and viscoelastic material specimens under a constant stress of unit magnitude until time, $t_1$ . . . . .	106
A.2	Creep and recovery of a viscoelastic material specimen subjected to a constant stress of unit magnitude until time, $t_1$ . . . . .	108

# List of Symbols

$A$	area under a linear load-displacement curves
$A^*$	area under a nonlinear load-displacement curves
$a_{T_c}$	time-temperature shift factor
$b$	a constant determining a shape of a K-S-N curve
$c$	a constant determining a shape of degradation of residual strength
$C$	Arrhenius constant
$D$	diameter of a cast-iron rod
$D_c$	creep compliance
DM	damage
$d_s$	deflection at a maximum load ( $P_s$ ) under a static load
$E_r$	relaxation modulus
$f$	original frequency
$f'$	shifted frequency
$F_N$	probability of fatigue life
$h$	height
$H$	Heaviside step function
$i, j, k$	indices
$K$	a constant determining a shape of a K-S-N curve
$L$	length
$MR$	median ranks

$n$	number of fatigue cycles
$N$	number of cycles to failure under a fatigue load ( $N = N_f - 1/2$ )
$N^*$	characteristic fatigue life
$N_f$	number of cycles to failure under a fatigue load
$P$	load
$P_f$	maximum load level under a fatigue load
$P_s$	maximum failure load under a static load
$\mathbb{P}$	probability function
$R$	gas constant
$\mathcal{R}$	residual strength
$\mathcal{R}(0)$	equivalent static strength
$R_\sigma$	stress ratio
$S$	stress range
$S_c$	creep shear failure strength
$S_f$	fatigue shear failure strength
$S_{f:0}$	fatigue shear failure strength at zero stress ratio
$S_s$	static shear failure strength
$t$	time
$t'$	shifted time
$t_c$	original time to failure under a creep load
$t'_c$	shifted time to failure under a creep load
$t_f$	original time to failure under a fatigue load
$t'_f$	shifted time to failure under a fatigue load
$t_s$	original time to failure under a static load
$t'_s$	shifted time to failure under a static load
$T$	temperature

$T_g$	glass transition temperature
$T_o$	reference temperature
$v$	strain rate under a static load
$w$	width
$x, y$	coordinate system

### Greek Letters

$\alpha$	shape parameter of Weibull distribution
$\alpha_f$	shape parameter of Weibull distribution for fatigue strength
$\alpha_s$	shape parameter of Weibull distribution for static strength
$\beta$	scale parameter of Weibull distribution
$\beta_f$	scale parameter of Weibull distribution for fatigue strength
$\beta_s$	scale parameter of Weibull distribution for static strength
$\delta$	deflection
$\Delta H$	activation energy
$\Delta t$	time step
$\varepsilon$	strain
$\varepsilon_e$	instantaneous elastic strain
$\varepsilon_d$	delayed elastic strain
$\varepsilon_v$	viscous strain
$\sigma$	stress
$\sigma_{max}$	maximum stress level
$\sigma_{min}$	minimum stress level
$\tau$	shear stress



# Chapter 1

## Introduction

### 1.1 Structural assembly

Structures have complex shapes and multiple components to satisfy their various functions. It is often not convenient to manufacture the entire structure in one single component. Rather, simple components are made separately and then assembled to form the whole structure.

Typical assembling of components is by joining. However, these structures with joints have a disadvantage because discontinuity of the materials at the jointed area causes stress concentrations. Because such stress concentrations sometimes cause premature failures of the structure, it is critical to perform a careful analysis of such areas.

### 1.2 Bonded joint

There are various types of joints, such as bolted joints, welded joints, and bonded joints.

A bolted joint is made by drilling holes in the units and linking them with the bolts mechanically. Some structures need only few bolts and holes, but others such as airplanes require millions of holes and bolts during fabrication.

A bonded joint is made by filling adhesive material between the components,

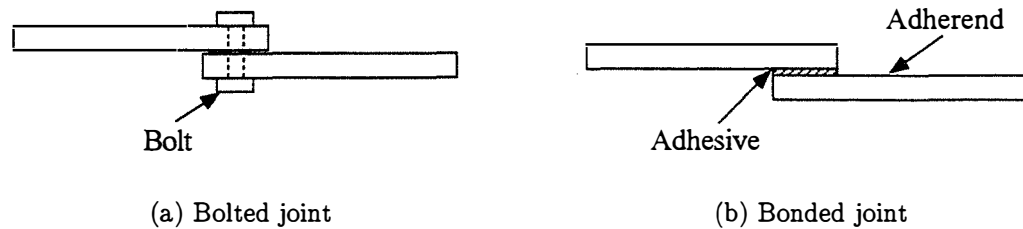


Figure 1.1: Joints in structural assembly.

which are called adherends. It requires no hole drilling, but it is critical to make the right choice of the adhesive material and processing conditions. Figure 1.1 shows configurations of typical bolted and bonded joints.

Determination of the joint type is made based on the purposes of the structure. The manufacturers choose the bonded joint in many applications because of the following advantages:

- The bonded joint adds little weight to the structure, compared with the mechanically fastened joint.
- It distributes the applied stresses over a larger bonding area.
- Because the bonded joint requires no hole drilling, no fasteners and no shims that are necessary for making the bolted joint, it requires less manufacturing. Structural assembly with this bonded joint is fast and low cost.
- When the components are made of composite materials with fibers embedded in them, hole drilling is not only a complicated operation but also may cause serious damage to the fibers. These damages may result in significant degradation of the composite materials. Because it is possible to avoid the fiber breakage and other damages by using the bonded joints, the composite materials can preserve the advantages of fiber reinforcement.
- It is easy to control the joint properties, such as stiffness and strength, by varying bondline thickness and overlap length.

### 1.3 Previous work on bonded joints

Many researchers have analyzed bonded joints for many years. However, most of the extensive work has been focused on a stress analysis.

Adams and Peppiatt [1] calculated the stress field and the stress concentration at the bondline using a finite element analysis method. Chen and Cheng [2] provided a closed-form solution using a *variation method* more than twenty years ago. Recently, Whitcomb and Woo [3] introduced an elasto-plastic analysis to calculate a debond growth of the bonded joints.

Some limited work on the strength analysis has been done recently, however. Guess and Reedy [4,5] performed a finite element analysis to calculate static strength of bonded joints under axial and flexural loadings. Choi and Kim [6,7] performed experimental work to obtain torsional strengths. This strength analysis always requires experimental verification. However, because of the difficulty in fabricating the bonded joints, the strength analysis has been limited in number. Furthermore, most work has been done for static strength only. Guess and Reedy have performed very limited tests for fatigue strength, but they tested at only two stress levels, making it difficult to even draw a S-N curve. Furthermore, because this work was done under one set of conditions, it cannot be extended to other conditions.

Nearly all of this previous work has dealt with thin adhesive bondline, in the order of a few thousandths of inches. Only Guess and Reedy have studied a thickness of hundredths of inches. However, because the bondline thickness significantly affects the behavior of the bonded joint, it is difficult to apply these results directly to structures with a thick bondline, which is of particular interest in assembly of large structures such as windmill blades.

## 1.4 Theory of viscoelasticity

Under the hypothesis of an elastic analysis, material subject to loading behaves independently of testing conditions, such as temperature and loading periods. Properties of this elastic material are assumed to be constant over a wide range of temperatures and loading conditions. The elastic analysis is adequate to describe the instantaneous behavior of the material at relatively low temperatures.

However, we do observe that the material properties actually vary with the testing conditions, especially at high temperatures or under long periods of loadings. Some materials, such as epoxy, exhibit such dependence even at low temperatures (e.g., room temperature) or under short periods of loadings. As Appendix A explains, this dependence of the material properties results from the viscosity of the material. Therefore, the theory of viscoelasticity has been introduced to model mechanical behavior combining the elastic and viscous properties of the material. Because the adhesive material of bonded joints is an epoxy type of material, we will analyze its behavior based on the theory of viscoelasticity.

## 1.5 Life estimation of bonded joints

Despite the advantages of the bonded joint as explained in Section 1.2, many designers are not confident about the strength of the bonded joint because there are no positive, mechanical links like bolts. The designer would like to know which area is critical when the bonded-jointed structure is about to fail because the failure may occur not only in the material (adhesive, adherend) but also along the interface between the adhesive and the adherend materials.

In addition to these various failure modes, the failure strength varies significantly with loading periods and temperature. Because of its viscoelasticity, the properties of the adhesive material vary with time and temperature. Because the adhesive material is highly viscoelastic in many cases, this time and temperature dependence becomes so significant that we must consider it in the design of the structure.

One simple way of analyzing the time and temperature dependence of a bonded

joint is to perform a series of experimental tests. However, we might need a large number of tests performed at various temperatures and under long periods of loadings, unless we make suitable assumptions on the time and temperature dependence. One assumption we made in this thesis is based on experimental evidence to show that the life of viscoelastic materials can be accelerated by elevating temperature under the operation condition of a structure. This experimental evidence is called *time-temperature equivalence* [8,9]. By applying this time-temperature equivalence, it is possible to estimate the behavior at low temperatures and under long-term loading conditions by performing the tests at high temperatures and for short periods. It is customary to apply this equivalence to the deformation of structures. We intend to extend this method to include the strength of bonded joints in this study.

# Chapter 2

## Fabrication of tubular lap bonded joints

### 2.1 Problem statement

To obtain meaningful experimental results performed under various conditions, we must first fabricate consistent test specimens. This chapter proposes a new method to fabricate tubular lap bonded joints. The method involves a surface treatment, a concentric alignment and a thick adhesive bondline.

### 2.2 Tubular lap joint

Various types of bonded joints include the single lap, double lap and tubular lap joint, as Figure 2.1 shows. All of these can be analyzed with two-dimensional models based on assumptions of either plane stress or plane strain for the single lap and double lap joints, or of axisymmetry for the tubular lap joint. Among these bonded joints, we chose the tubular configuration for this study for the following reasons.

First of all, because of its axisymmetric shape, we can apply more types of loadings to the tubular lap joint than to the other two joints. It is extremely difficult to apply loads other than the tensile load to the single lap and double lap joints because they become unstable easily. However, with the stable tubular configuration, it is possible

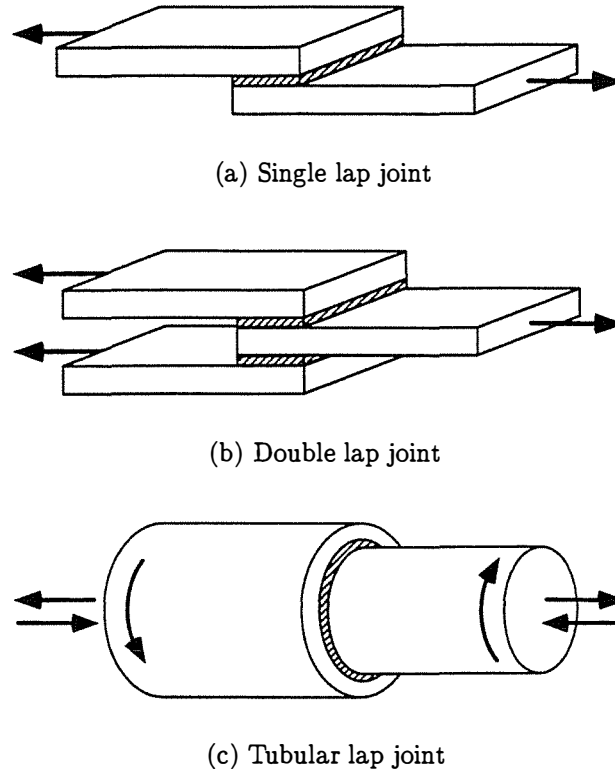


Figure 2.1: Various types of bonded joints: Only tensile load is applicable to single and double lap joints, whereas tensile, compressive, and torsional loads are applicable to tubular lap joints.

to apply the tensile, compressive and even torsional loads, as shown in Figure 2.1. This flexibility of applied loadings will enable us to study the loading effects on the behavior of the bonded joint in a future study.<sup>1</sup>

Furthermore, when we apply the loading to the single lap or double lap joint, we can observe stress concentration at the side-edges of the joint because of its finite width. Sometimes this edge effect is not localized, but affects the behavior of the bonded joint significantly, especially when failures of these joints are initiated at the side-edges. In this case, the two-dimensional model based on the plane assumptions

---

<sup>1</sup>In this study, only the tensile load is applied.

is no longer adequate because the edge effect matters with a plane perpendicular to the model plane. The analysis may require more involved calculation, such as the three-dimensional finite element method. Because the circular shape of the tubular lap joint avoids any edge effect, it is possible to perform the two-dimensional analysis based on the axisymmetry assumption. Thus, the analysis is simpler for the tubular lap joint than it is for the other joints.

### 2.3 Configuration of tubular lap joint

In building a windmill, three or four individual windmill blades are fabricated with composite materials, and attached to blade inserts of a root by bonding. The blade insert of the root is usually made of metal such as steel or cast iron. This metal insert is machined, coated with primer material, and bonded to the inner surface of the composite blades. In general, the bonding is structurally the most critical process of this blade assembly.

In this study, we chose a metal-to-composite tubular lap bonded joint to simulate such geometry and material, We used ductile cast-iron rod (FCD 600) and Glass Fiber Reinforced Plastic (GFRP) composite pipe as adherends to simulate the metal insert and the composite blade, respectively. The GFRP pipe is made from woven prepreg with layup of  $[0/90]_s$ , and wound in a winding machine to form the tubular shape. Longitudinal modulus of this GFRP pipe in the axial direction is 36.5 GPa.

An epoxy type of adhesive material is provided by Kenetech Windpower. We prepared this adhesive material for bonding by mixing two components of epoxy with 1/4 inch of chopped glass fibers. To obtain the most accurate material property information, these specimens must

- be as uniform in thickness as possible
- have as few voids as possible, and
- have well-mixed fillers so that the mixture contains the same density of fillers.

Viscosity after mixing is 13,500 cps.



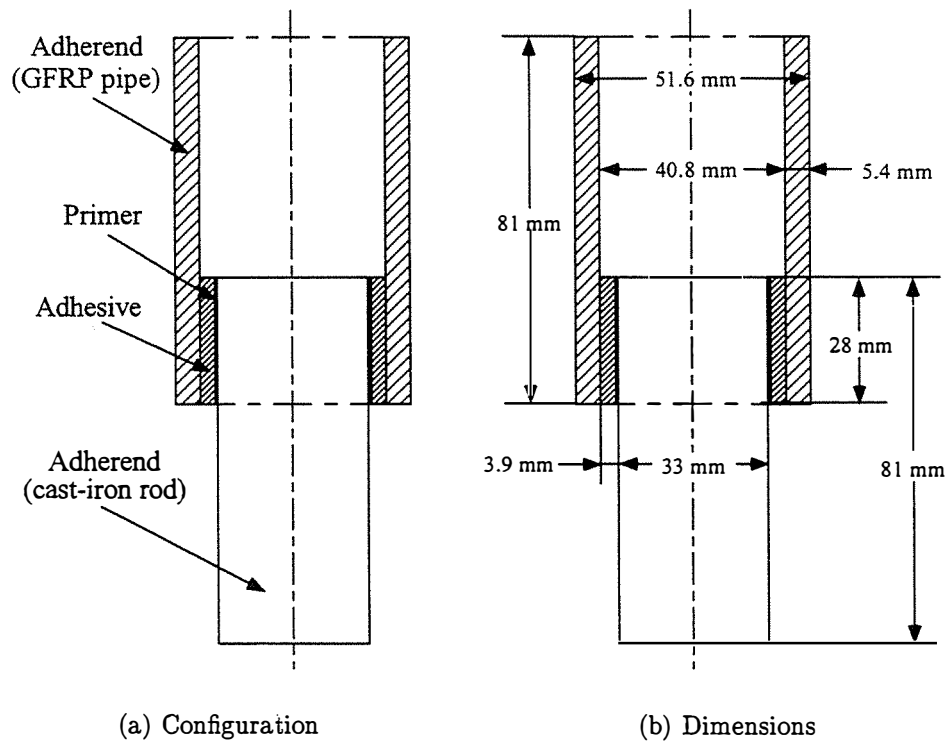


Figure 2.2: Cross section of tubular lap bonded joint made of two adherends (a cast-iron rod and a GFRP composite pipe) and adhesive material: Surface of the cast-iron rod is coated with a primer material to increase bonding strength between the cast-iron rod and the adhesive material.

This highly viscous adhesive material with the fillers enables us to have a thick bonded joint. This thick tubular lap joint can simulate the windmill structure with a thick bondline between the metal insert and the windmill blades. This thick bondline is preferred in order to facilitate assembly of the joint.

The selected materials and dimensions of the cross section of the tubular lap joint are shown in Figures 2.2(a) and 2.2(b), respectively. Properties and a curing condition of the adhesive material will be discussed later in Chapter 3.

## 2.4 Surface treatment of cast-iron rod

The GFRP pipe and the adhesive material can be well-bonded with each other without any surface treatment because both are polymeric materials. However, bonding between metal and the polymeric adhesive material is not achieved well enough to provide reasonable bonding strength. This is especially true in the case of the cast-iron rod, which has a slippery surface. For this reason, we did a surface treatment on the cast-iron rod by

- (1) roughening the surface of the rod with two types of sandpaper (Emery sandpaper #100 and #400).
- (2) wiping it with acetone solution, and
- (3) coating it with a thin primer material.

Kenetech Windpower has studied many surface treatments, and found that American Cyanamid Epoxy Primer BR 127 provided the highest bond property for this adhesive material.<sup>2</sup>

The application of the primer material (and the surface preparation prior to priming) is the most critical process of the structural assembly because the primer is coated in the area where most root bond failures begin. A suggested method is to apply the primer material uniformly with a thickness between 0.0001" and 0.0002". To achieve the uniform thin primer coating, we tried two application methods—painting and spraying. The first method is to paint the surface of the cast-iron rod with a brush, and the second method is to apply the primer with a spray gun at a constant spraying rate. For the latter, we placed the cast-iron rod on a turn table and rotated the table at a constant angular velocity. To determine an optimal condition, we performed a parametric study by varying the number of revolution, and measuring tensile static strengths of the bonded joint.<sup>3</sup> At the optimal condition, the static strengths must be as high as possible, and their scatter must be as small as possible.

Figures 2.3(a) and 2.3(b) show the results from the painting method along with those from the spraying method at spraying rates of 0.033 *grams/rev* and 0.085

---

<sup>2</sup>BR 127 is also used for corrosion protection for the entire insert surface.

<sup>3</sup>Fabrication method of this bonded joint will be treated later, in Section 2.5.

*grams/rev.* In these figures, the painting method provided high strengths and a reasonably small scatter compared to the spraying methods. For this reason, we selected the painting method to apply the primer BR 127 on the surface of the cast-iron rod.

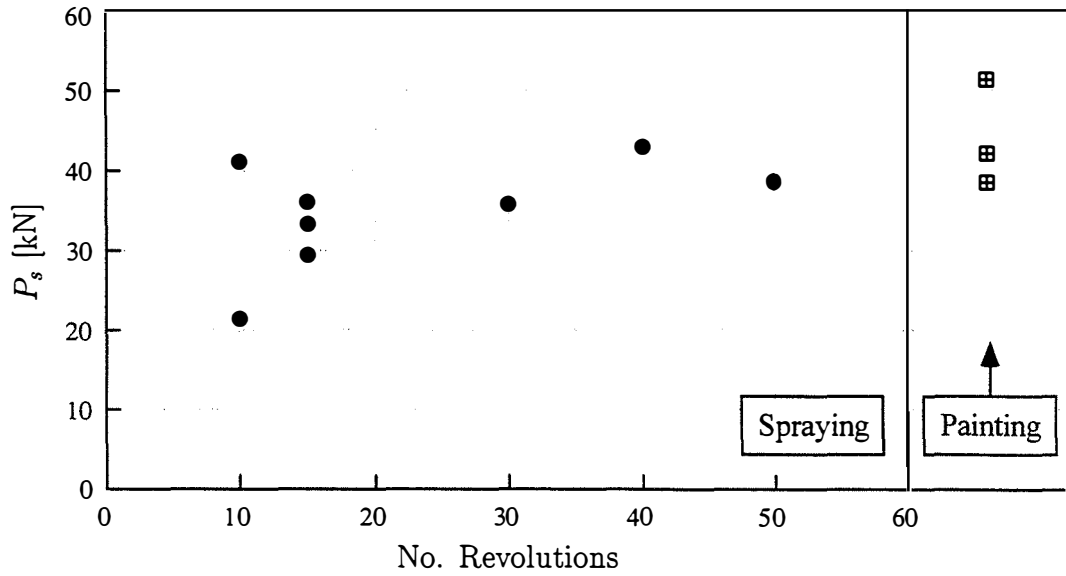
## 2.5 Fabrication of tubular lap joint

We fabricated the tubular lap joint considering two aspects:

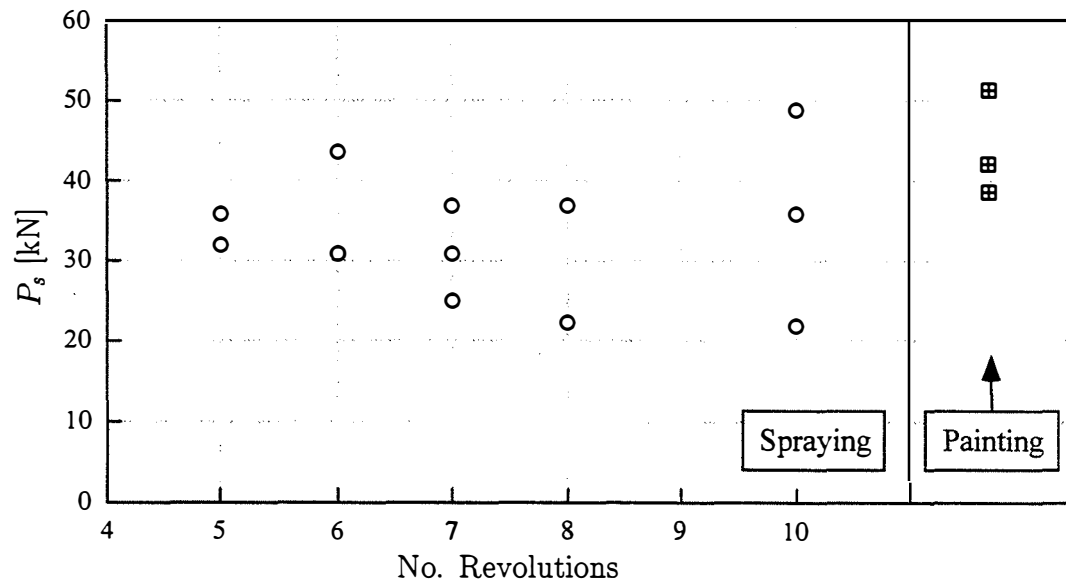
- (1) The two adherends must be aligned concentrically with respect to a center line.
- (2) The adhesive material must fill the gap between two adherends uniformly with little voids.

However, when the adhesive material with the high viscosity fills the thick bondline, it is not easy to keep the concentric alignment and to remove the voids trapped inside the bonding area. For this reason, we devised a special mold with a steel pipe, a Teflon pipe and a steel cap, with the following provisions:

- The steel pipe was machined to have an inner diameter the same as the outer diameter of the GFRP pipe. The steel pipe guides the outer boundaries of the Teflon pipe as well as the GFRP pipe for the alignment.
- The Teflon pipe was machined to have an inner diameter the same as the diameter of the cast-iron rod and an outer diameter the same as the inner one of the GFRP pipe. This Teflon pipe makes two adherends align concentrically. At the same time, this Teflon pipe prevents the adhesive material from flowing downwards out of the bonding area during curing to form a flat edge at the end of the overlap of the adhesive layer. Because the Teflon material is not apt to bond with the adhesive material, it is easy to separate them after the cure.
- The steel cap was machined to have an inner-side wall diameter the same as the outer diameter of the steel pipe, and to have a circular hole at the bottom.



(a) Spraying rate of 0.033 grams/rev



(b) Spraying rate of 0.085 grams/rev

Figure 2.3: Variation of tensile static strength by surface treatment methods: Primer material is coated on surface of cast-iron rod by painting method and spraying method at spraying rates of 0.033 gram/rev and 0.085 grams/rev, respectively.

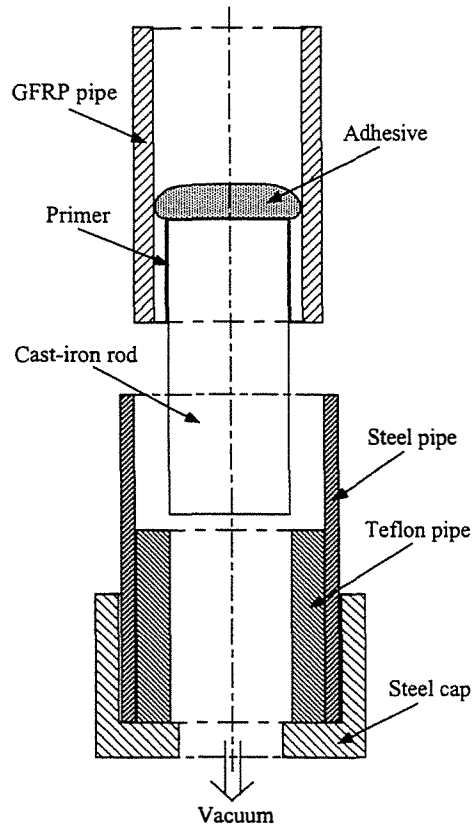


Figure 2.4: Molds and materials for fabrication of a bonded joint: The molds were designed to achieve a concentric alignment and a uniform thickness of a thick adhesive layer.

We inserted two pipes (steel pipe and Teflon pipe) into the steel cap to form the mold. Then we inserted the two adherends (cast-iron rod and GFRP pipe) into this mold, as Figure 2.4 shows.

The next step is to fill the adhesive material uniformly into the gap between two adherends with few voids. We mixed the adhesive material with chopped glass fibers and placed it on top of the cast-iron rod in the mold, as shown in Figure 2.4. Because the adhesive material contained many chopped glass fibers and was highly viscous, it was extremely difficult to fill the gap in a natural way. Furthermore, this natural flow-filling caused many voids to be trapped inside the adhesive layer. To solve this

problem, we applied a vacuum downwards through the hole of the steel cap for 3 minutes.<sup>4</sup> We then sealed the gaps of the molds with silicon rubber to prevent air leaking during the vacuuming. Also, by applying this vacuum, we tried to remove major voids that were possibly trapped inside the bonding area.

All the molds and the materials were kept at room temperature for 24 hours before the cure. They were then placed in an oven at 100°C for 24 hours and then at 60°C for an additional 24 hours. After the cure, they were once again kept at room temperature for 24 hours, and then the molds were removed.

## 2.6 Testing configuration

Among the various types of loadings applicable to the tubular lap joint, we applied only a tensile type of loadings in this study. We applied monotonically increased, uni-axial tensile loadings at several temperatures and strain-rates with an Instron-type testing machine in a temperature chamber; Chapter 4 will treat it in more detail. We also applied uni-axial tensile-tensile cyclic loadings at several temperatures, frequencies, and stress ratios with a Shimazu servo-pulsar testing machine in a temperature chamber; Chapter 5 will describe it in more detail.

For the tensile type of loadings, grips of the testing machines must hold two ends of the tubular lap joint. For this purpose, before they were bonded together, we machined the cast-iron rod and the GFRP pipe with NC machines to make screws at the ends of them.

During the tests, the test machines recorded various outputs, such as the applied loadings and displacements in the case of the monotonically increased loadings, or number of cycles in the case of the cyclic loadings. Although the test machines can record the load increase and the the number of cycles accurately, they failed to record accurate displacements because the test machines have their own compliances. The displacements recorded by the machine output differed from the real displacements of the test specimen. This discrepancy is significantly large when the specimen has a

---

<sup>4</sup>There was one minute of pause between the first two minutes of vacuuming and the second one minute of vacuuming.

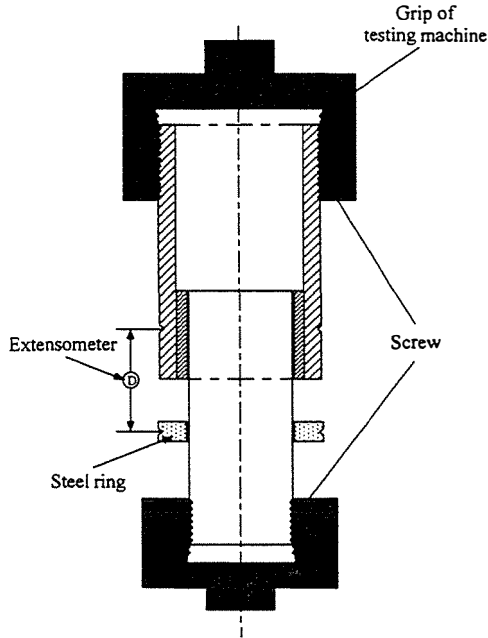


Figure 2.5: Configuration for tensile type of tests: Screwed ends of test specimen were held by grips of the testing machine. Displacements were recorded accurately by an extensometer that was attached to the GFRP pipe and a steel ring.

small deformation.

For an accurate displacement measurement, we prepared a steel ring, whose outer diameter is the same as that of the GFRP pipe, and attached it tightly to the cast-iron rod, as shown in Figure 2.5. Then we attached an extensometer to the peripheries of the steel ring and of the GFRP pipe at a distance of 50 mm to record more accurate displacements of the test specimens. Figure 2.6 shows two significantly different load-displacement curves under the uni-axial tensile loadings when the displacements were measured with the machine signal and with the extensometer.

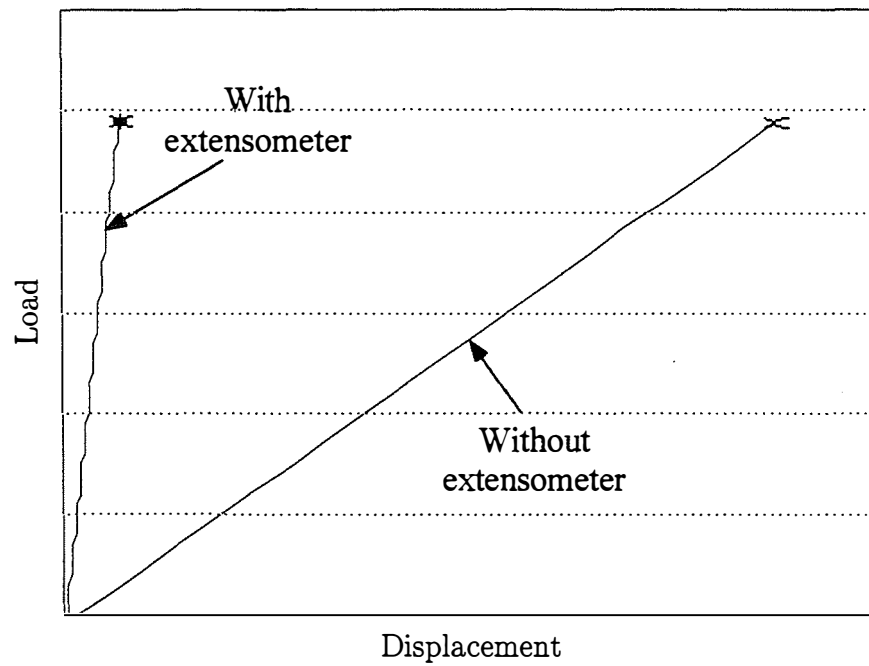


Figure 2.6: Load versus displacement curves of uni-axial tensile loadings when the displacements were measured with and without an extensometer.



# Chapter 3

## Creep compliance of adhesive materials

### 3.1 Problem statement

Properties of some materials change with time: Viscosity prevents them from behaving instantaneously. They also change with temperature because the viscosity changes significantly under different temperature conditions. This time- and temperature-dependent viscous behavior of the material is treated in the scope of viscoelasticity.

Almost all materials show this viscoelasticity under the time- and temperature-varying conditions. Polymeric materials are well known to have these viscoelastic properties not only at high temperatures, such as above their glass-transition temperature ( $T_g$ ), but also at low temperatures, such as near and even below the glass-transition temperature. These viscoelastic properties are also determined by curing conditions of the material. Because the adhesive material of the bonded joint is polymeric, it is necessary to study the time- and temperature-dependent behavior of this adhesive material, which is made under several curing conditions, before analyzing the bonded joint.

The time and temperature dependence of the adhesive material can be shown by

experimental tests for measuring either creep compliance or storage modulus performed at several temperatures during a certain period of loading. The measured creep compliance or storage modulus will be plotted on a time scale, and the curves on this plot will be shifted horizontally to be overlapped with a curve at a reference temperature. This shifting process is based on the time-temperature equivalence, which will be explained in Section 3.2.1. The shifted curve in this process is called a master curve. The smoothness of the master curve determines whether we can apply time-temperature equivalence to this adhesive material at the measured time and temperature range. Time-temperature shift factors will be calculated at each temperature during this process, which is defined by the difference between the measured and the shifted time. The next section explains details of the time-temperature equivalence and the time-temperature shift factor.

## 3.2 Time-temperature equivalence and time-temperature shift factor

### 3.2.1 Time-temperature equivalence

Time-temperature equivalence is experimental evidence that is applicable to many viscoelastic materials. This equivalence says that we can superpose the time and the temperature to describe behavior of the material. According to this time-temperature equivalence, rise and fall of the temperature corresponds to extension and contraction of the time scale. In other words, short-term behavior of material at a high temperature corresponds to its long-term behavior at a low temperature. In this way, the time and the temperature can be transformed with each other. Usually, the behavior at a high temperature corresponds to that of a long period of time and the behavior at a low temperature corresponds to that of a short period of time. By applying this equivalence, we can predict long-term behavior of the material by performing short-term tests at elevated temperatures.

This prediction process can be easily achieved by drawing a master curve, as Figure 3.1 shows. Suppose we measured a material property (such as creep compliance)

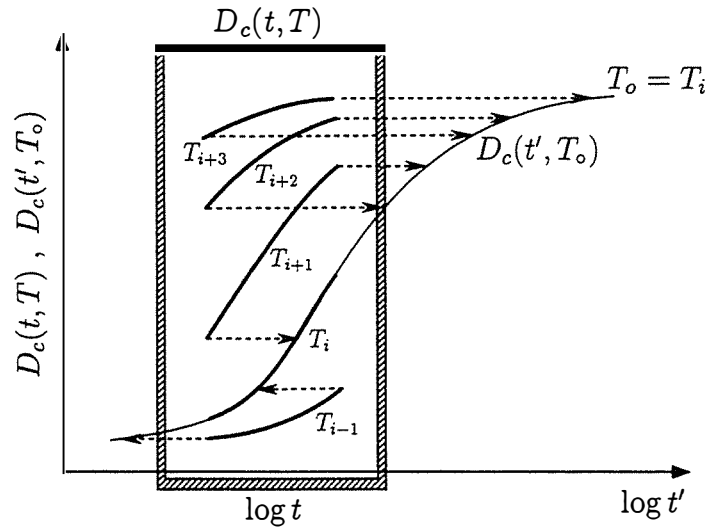


Figure 3.1: Creep compliance curves for test data on measured time scale ( $t$ ), and a master curve at a reference temperature ( $T_o$ ) on shifted time scale ( $t'$ ).

at several temperatures during some loading periods, and plotted the results in time scale ( $t$ ). We can then draw a master curve of creep compliance with the following process:

First, we can set any of the temperatures as reference temperature ( $T_o$ ). Then we can shift the curves at the temperatures other than the reference temperature horizontally so that they coalesce with a portion of the curve at the reference temperature. As shown in Figure 3.1, if we set  $T_i$  as the reference temperature, we can shift the curve for  $T_{i+1}$  to place it on the portion of the curve at  $T_i$ . This shifted curve forms a new portion of the reference curve. Then we can shift the curve for  $T_{i+2}$  to place on the new portion, and so on. The curves at higher temperatures than the reference temperature are shifted to the right side to form long-term periods, and the curves at lower temperatures are shifted to the left side to form short-time periods. The higher the temperature is, the longer the curve is shifted, and vice versa. We call the curve drawn by these shifts the *master curve* at the reference temperature, and the new time scale ( $t'$ ) *shifted time* or *reduced time*. If we can draw the master curve smoothly by these shifts, we can claim that the time-temperature equivalence

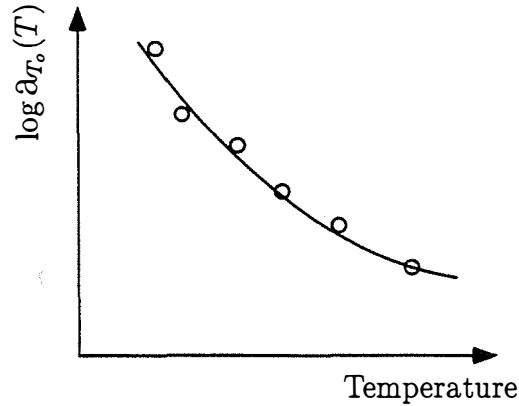


Figure 3.2: A typical plot of time-temperature shift factors as a function of temperature.

is applicable to the property of the material. Previous work has shown these smooth master curves for many polymeric materials.

This time-temperature equivalence is not a fundamental theory but an empirical one that has been verified by many experiments with the viscoelastic materials. This equivalence is very useful for predicting the long-term (a few decades) behavior of the material by performing the short-term tests at elevated temperatures.

### 3.2.2 Time-temperature shift factor

When we draw the master curve, we can calculate a ratio of the measured time ( $t$ ) to the shifted time ( $t'$ ) as

$$a_{T_0}(T) = \frac{t}{t'} \quad (3.1)$$

This ratio ( $a_{T_0}$ ) is called the time-temperature shift factor, which represents the degree of parallel movement in drawing the master curve.

Previous experiments revealed that, in many cases, the time-temperature shift factor is mainly a function of temperature. Figure 3.2 shows a typical plot on the temperature scale.

For a large class of polymeric materials, the curve for the time-temperature shift factor can be expressed by equations, such as the Williams-Landel-Ferry (WLF) equation [10] or the Arrhenius equation.

The WLF equation is written as

$$\log a_{T_0}(T) = -\frac{17.44(T - T_g)}{51.6 + T - T_g} \quad (3.2)$$

where  $T_g$  is the glass-transition temperature of the particular materials under consideration. Using this equation, we must set the reference temperature to the glass-transition temperature. It was found that this equation is valid near glass-transition temperatures, especially in the temperature ranges from  $T_g$  to  $T_g + 100^\circ\text{C}$  [11]. The numerical constants in this equation were established by experiments within this temperature range.

This simple equation is useful when the glass-transition temperature is known for the material and the temperature under consideration is near and above this glass-transition temperature. However, this equation is not applicable for the temperature range below the glass-transition temperature because it does not produce an inflection point near the glass-transition temperature, which is typically observed in the curves of many viscoelastic materials.

Another way to express the time-temperature shift factor is by using the Arrhenius equation (see Appendix A), which is written as

$$a_{T_0}(T) = \log \frac{t}{t'} = C \exp\left(\frac{\Delta H}{2.303RT}\right) \quad (3.3)$$

where  $C$ ,  $\Delta H$  and  $R$  are Arrhenius constant, activation energy and gas constant, respectively. Taking the logarithm on both sides of the equation and noting that  $a_{T_0}(T_0) = 1$  (no horizontal movement at the reference temperature), Eq. (3.3) becomes

$$\log a_{T_0}(T) = \frac{\Delta H}{2.303R} \left[ \frac{1}{T} - \frac{1}{T_0} \right] \quad (3.4)$$

where  $\Delta H$  is the activation energy in  $[J/mol]$ ,  $R$  is the gas constant,  $8.314 [J/(^\circ\text{K} \cdot$

$mol$ ]], and  $T$  and  $T_0$  are the measured and the reference temperature in degrees K, respectively. This equation enables us to evaluate the time-temperature shift factor for a wide range of temperatures not only near and above but below the glass-transition temperature. Furthermore, we do not need to know the glass-transition temperature in advance to apply this equation.

By Eq. (3.4), we can also evaluate the activation energy ( $\Delta H$ ) from a slope of a curve by plotting the time-temperature shift factor on log scale ( $\log a_{T_0}(T)$ ) in  $y$ -axis and inverse of the temperatures ( $1/T$ ) in  $x$ -axis. The physical meaning of this activation energy is a measure of energy barrier that must be overcome when molecular motion of the viscoelastic material is to occur. In many viscoelastic materials, higher activation energy is required below the glass-transition temperature and lower activation energy is required above the glass-transition temperature. For this reason, the activation energy of the viscoelastic materials changes drastically near the glass-transition temperature, so that the plot of  $\log a_{T_0}(T)$  versus  $1/T$  has an inflection point near the glass-transition temperature.

Once we evaluate the activation energy by the slopes of the curves, we can calculate the time-temperature shift factors at any intermediate temperatures by Eq. (3.4). This, in turn, enables us to calculate the original time ( $t$ ) corresponding to the shifted time ( $t'$ ) at any temperatures by Eq. (3.1). Finally, we can draw the curves for creep compliance at any temperature by shifting the master curve on the shifted time scale back to a curve on the original time scale.

### 3.3 Test condition for creep compliance of adhesive material

We performed three-point bending tests to measure the creep compliance of the adhesive material at various temperatures and to analyze the time and temperature dependence. Meanwhile, we analyzed the dependence of the curing condition for the viscoelastic adhesive material.

We prepared adhesive panels that were cured under three different conditions,

denoted as Cure I, Cure II and Cure III. The three adhesive panels under these conditions are denoted as Adhesive I, Adhesive II and Adhesive III, respectively. The curing temperature and its duration under these conditions are as follows:

(Cure I) 71°C for 1 hour

(Cure II) 99°C for 1 hour

(Cure III) 100°C for 24 hours + 60°C for 24 hours

The adhesive panels under the three curing conditions were then cut with dimensions of  $80\text{ mm} \times 15\text{ mm} \times 3\text{ mm}$  ( $L \times w \times h$ ), where  $L$ ,  $w$  and  $h$  are length, width and thickness of the panels, respectively. These panels were placed on a three-point bending fixture (located at Kanazawa Institute of Technology in Japan), as Figure 3.3 shows.

We applied a constantly applied creep load ( $P = 19.6\text{ N}$ ) to the middle of the panel. This applied load lasted for 20 hours at six temperatures ranging from 40°C to 90°C with 10°C increments.<sup>1</sup> During this period, the test machine recorded the history of the deflection at the middle point.

## 3.4 Test results

### 3.4.1 Creep compliance of adhesive material

Under the constant loads maintained during the experiment, we observed that the deflection depended on time and temperature because of the viscoelasticity of the adhesive material. Using simple beam theory [12], we can calculate histories of stresses and strains with the applied load, the deflection history and the geometry of the adhesive panel. The constantly applied load resulted in a constant stress ( $\sigma_o$ ), and the deflection history resulted in a time- and temperature-dependent strain history ( $\varepsilon(t, T)$ ). Creep compliance ( $D_c$ ), which is a ratio of the strain to the stress, was then

---

<sup>1</sup>For Adhesive I, we limited the temperature increase to 70°C because the curing temperature was 71°C.

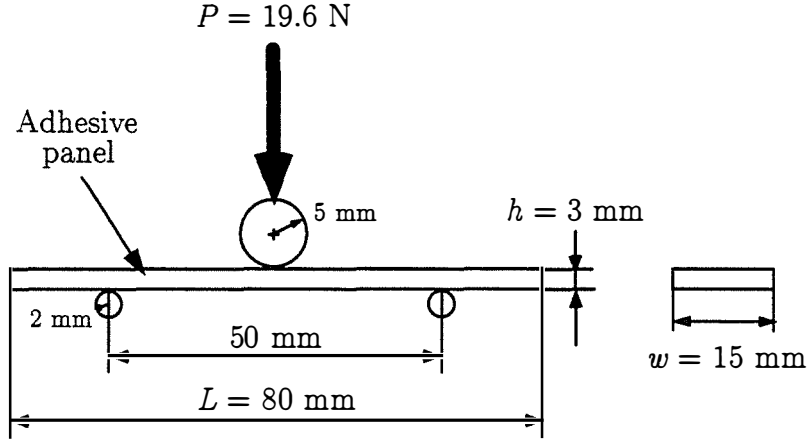


Figure 3.3: Dimensions of an adhesive panel, and a testing fixture for performing three-point bending tests to measure deflection history under a constant loading.

calculated as

$$D_c(t, T) = \frac{\varepsilon(t, T)}{\sigma_o} = \frac{4wh^3}{L^3} \frac{\delta(t, T)}{P} \quad (3.5)$$

where  $P$  is the applied load and  $\delta(t, T)$  is the deflection history.

Figure 3.4 shows the creep compliances of the adhesive material for curing conditions I, II and III at the six temperatures on a logged time scale. The creep compliances increase little at a low temperature of 40°C and at a short time for Cure I, Cure II and Cure III, but they increase significantly as the temperature and the loading period increase. The creep compliance curves of Cure I are distinctive at each temperature. For Cure II and Cure III, however, we can draw the creep compliance curves closely for temperatures at 40°C and 50°C closely for the entire loading period. Furthermore, these curves are significantly distinctive from the ones at higher temperatures. Above the glass-transition temperature, which is near 60°C, the creep compliance increased drastically as the temperature and the loading period increased for Cure I, Cure II and Cure III.



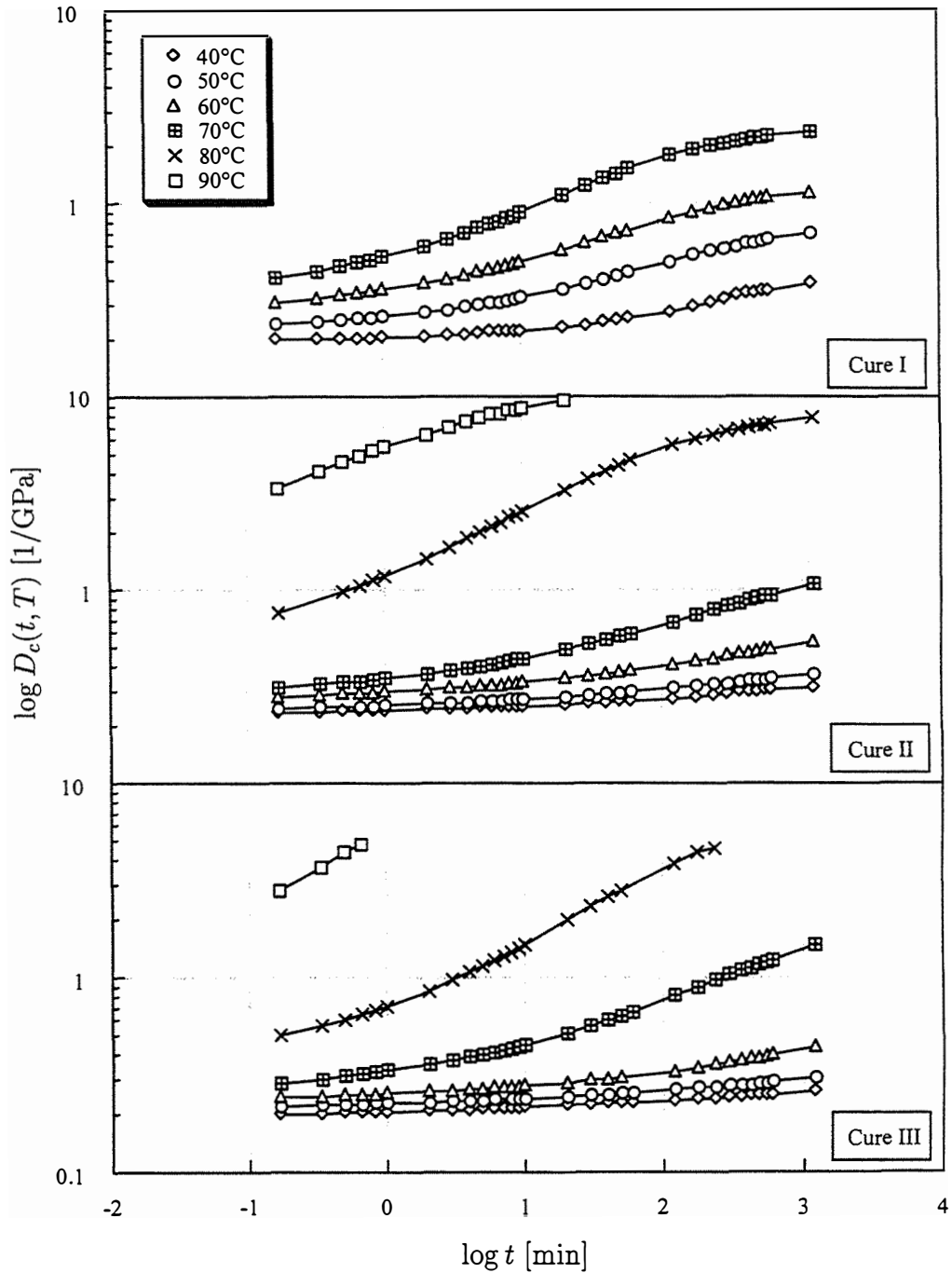


Figure 3.4: Curves of creep compliance of adhesive materials ( $D_c$ ) on logged time scale ( $t$ ) at six temperatures during 20 hours.

Table 3.1: Time-temperature shift factors of adhesive materials.

Type	$\log a_{T_0}(T)$					
	40°C	50°C	60°C	70°C	80°C	90°C
Cure I	0.00	-1.70	-2.90	-4.00	—	—
Cure II	0.00	-0.90	-2.40	-3.72	-6.92	-9.02
Cure III	0.00	-1.30	-2.65	-4.70	-6.63	-9.12

### 3.4.2 Master curves of creep compliance and time-temperature shift factor

Figure 3.5 shows the master curves of creep compliance of the adhesive materials for Cure I, Cure II and Cure III. We set the reference temperature to 40°C. Then we shifted the curves in Figure 3.4 horizontally, which are at a higher temperature than the reference temperature, to create the longer portions on the time scale.

The master curves in Figure 3.5 are plotted together in Figure 3.6. Because three master curves were drawn smoothly for all adhesive materials, we can conclude that the time-temperature equivalence is applicable to the creep compliance of the adhesive material regardless of the curing conditions. However, the smoothness of those curves is different, and we can observe that the master curve for Cure III is the smoothest of all. This shows that Cure III is the stablest curing condition for this adhesive material.

We calculated the time-temperature shift factors by Eq. (3.1) while we drew the master curves, and listed in Table 3.1. These factors were plotted with solid dots on an inverse temperature scale ( $1/T$ ) in Figure 3.7. Then we fitted these time-temperature shift factors in each figure bi-linearly to have two lines with an inflection point near the glass-transition temperature.

We calculated two activation energies,  $\Delta H_1$  and  $\Delta H_2$ , by calculating the slopes of two fitted lines, respectively. Table 3.2 lists these two activation energies of the adhesive materials for Cure I, Cure II and Cure III.

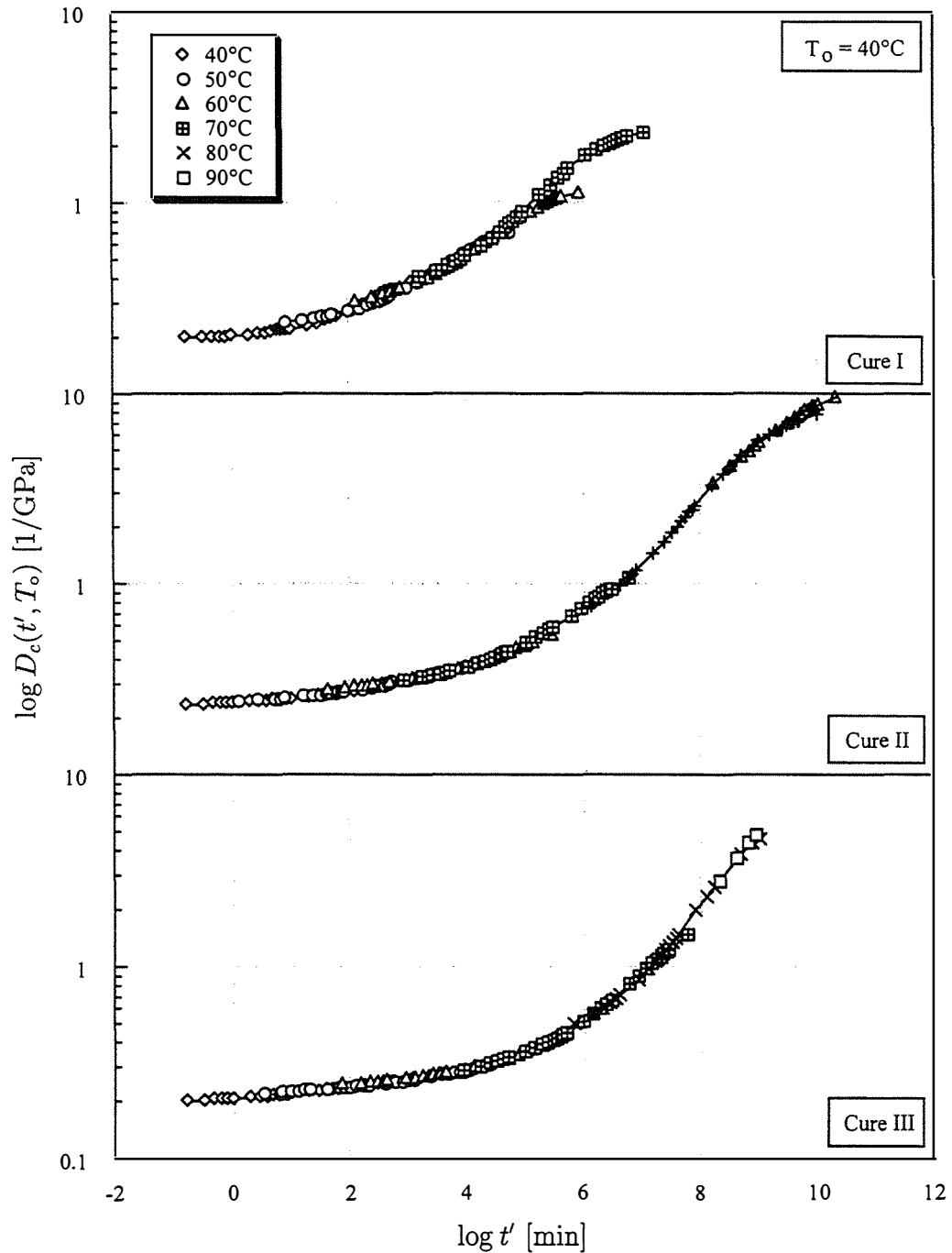


Figure 3.5: Master curves of creep compliance of adhesive materials on shifted time scale ( $t'$ ) at a reference temperature ( $T_0 = 40^\circ\text{C}$ ), drawn by shifting the creep compliance curves at elevated temperatures in Figure 3.4.

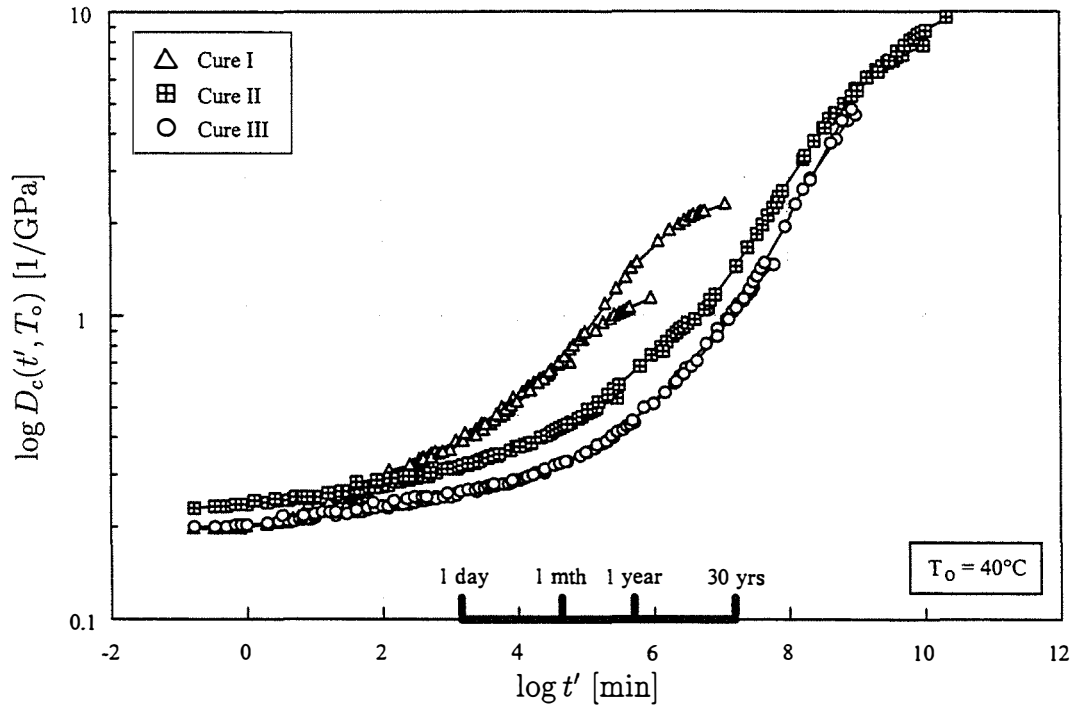


Figure 3.6: Three master curves of creep compliance of adhesive materials under three curing conditions, Cure I, Cure II and Cure III.

Table 3.2: Activation energy of the adhesive materials cured under three different conditions.

Type	Curing condition (Temperature $\times$ Duration)	Activation Energy	
		$\Delta H_1$ [KJ/mol]	$\Delta H_2$ [KJ/mol]
Cure I	71°C $\times$ 1 hour	272	—
Cure II	99°C $\times$ 1 hour	239	633
Cure III	100°C $\times$ 24 hours + 60°C $\times$ 24 hours	264	526

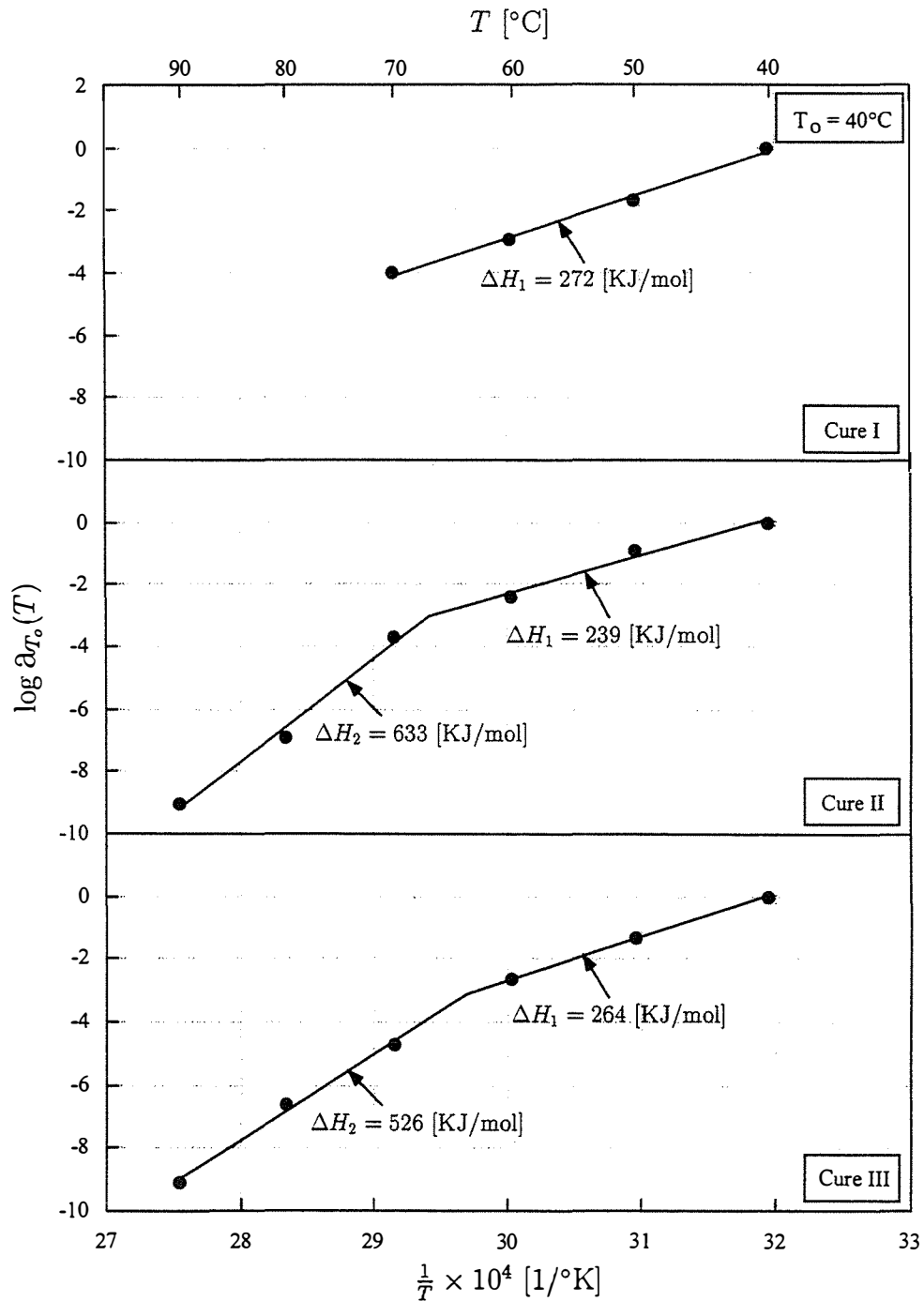


Figure 3.7: Time-temperature shift factor of adhesive materials and their fitted lines with inflection points near the glass-transition temperature ( $T_g$ ).

### 3.5 Conclusion

In this study, we measured the creep compliances of the adhesive material to show its viscoelasticity before the analysis of the bonded joint. We fabricated the adhesive panels under three different curing conditions and performed three-point bending tests by applying a constant load in the middle of the panel. Tests were performed at six temperatures during 20 hours to show the dependence of the creep compliance on temperature, loading time and curing condition.

The creep compliance increased as the temperature and the loading period increased, and this increase was significant above the glass-transition temperature and after a long period of loading. We drew the master curve of creep compliance of the adhesive material at a reference temperature by shifting the creep compliance curves at elevated temperatures. We also calculated the time-temperature shift factors at each temperature as the ratio of the measured time to the shifted time.

The smoothness of the master curves enable us to conclude that the time-temperature equivalence is applicable to the creep compliance of this adhesive material regardless of the curing condition. However, because Cure III, which cured at  $100^{\circ}\text{C} \times 24$  hours +  $60^{\circ}\text{C} \times 24$  hours, provided more stable adhesive material than Cure I or Cure II at a wide range of temperatures and loading periods, we selected this curing condition for fabricating the bonded joints.

# Chapter 4

## Static failures of bonded joints

### 4.1 Problem statement

Because the behavior of the adhesive material highly depends on time and temperature as concluded in Chapter 3, the behavior of the bonded joint is also expected to depend on time and temperature. For this reason, we can relate the dependence on the nondestructive property of the adhesive material (e.g., storage modulus, creep compliance) to that of the bonded joint (e.g., stiffness, compliance). In the meantime, such a relationship has also been observed between the destructive and nondestructive properties in several viscoelastic materials [9], even though the relationship is not fully backed up by a theory. In most cases, because it is much more difficult to obtain the destructive property (e.g., failure strength) than the nondestructive one, it will be helpful to prove such a relationship between them.

In this chapter, we will examine static behavior of the bonded joint to obtain destructive and nondestructive properties. In dealing with perfectly elastic materials, the static properties do not depend on time and temperature. However, the static properties of the bonded joint are expected to be dependent on time and temperature because of the viscoelasticity of the adhesive material.

We performed experiments at several strain-rates and temperatures to understand the failure mechanism and the time and temperature dependences of the static behavior. The time-temperature equivalence of the nondestructive property of the adhesive

material (creep compliance) is compared with that of the destructive property of the bonded joint (failure strength) under this type of loading. We then applied the time-temperature equivalence of the static failure strength of the bonded joint to draw a master curve and to calculate time-temperature shift factors.

## 4.2 Test conditions

For the static test, we applied a monotonically increased uni-axial tensile loading to the ends of the bonded joint at a temperature and a constant strain-rate. Grips of an Instron-type machine, which is located at Kanazawa Institute of Technology in Japan, held the screwed ends of the test specimen, as shown in Figure 4.1. Then both the grips and the specimen were placed in a temperature chamber. The bonded joint was placed in the temperature chamber for an additional 30 minutes after the temperature met the test condition.

Tests were performed at five temperatures ranging from 40°C to 80°C with 10°C increments. At each temperature, three different loading rates were applied at the stroke speeds of 100, 1 and 0.01 mm/min. Under each condition, five specimens were tested making the total number of specimens 75. During the tests, we recorded monotonically increased load and deflection until the load increase stopped as soon as the specimen had failed.

## 4.3 Test results

### 4.3.1 Load versus deflection

Figure 4.2 shows the load-deflection curves under the uni-axial tensile loadings at five temperatures at each loading rate. All the curves have linear slopes initially, then become nonlinear because of the viscosity of either the adhesive material or the resin in the composite pipe. As the temperature increased, the viscous property increased, and this caused a decrease in the maximum failure load as well as the initial slope of the curve. In the case of the slow strain-rate (0.01 mm/min), the curves showed



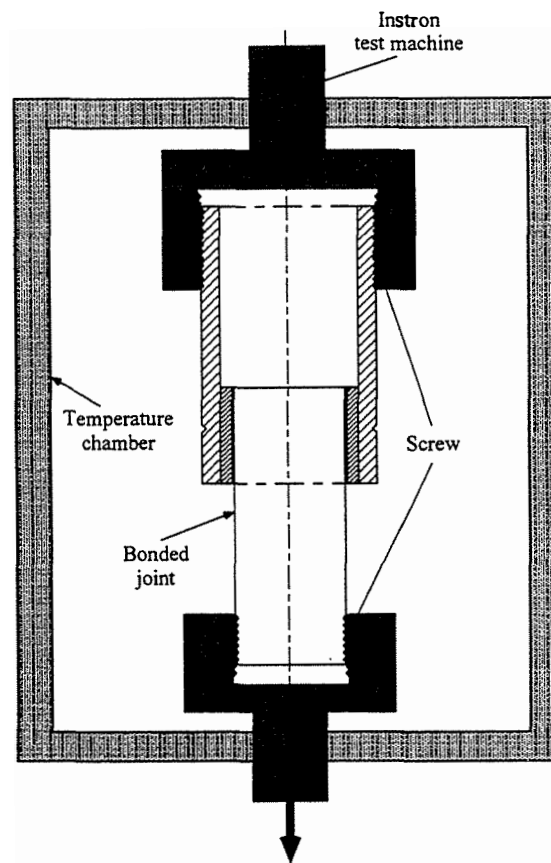


Figure 4.1: Configuration for static tests under a constant rate of monotonically increased uni-axial tensile loading: Both ends of the test specimen were screwed and held by grips of an Instron-type test machine.

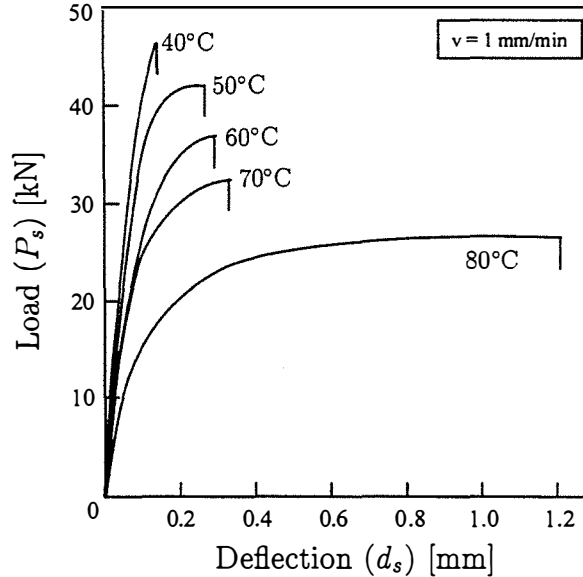


Figure 4.2: Load-deflection curves under uni-axial tensile loadings at five temperatures and three strain-rates.

more inelastic ductile behavior than in the other two cases, so that the maximum loads decreased significantly. Thus, the stiffness (nondestructive property) and the strength (destructive property) of the bonded joint show the dependence on time and temperature.

When we examined the load-deflection curves in Figure 4.2, we were able to separate them into two categories, as shown in Figure 4.3. One kind of curve is drawn smoothly up to the maximum failure loads and drops suddenly at the moment of failure without being further carried out the loads. These curves indicate *brittle failure* of the bonded joints. Meanwhile, the other kind of curve is drawn smoothly before and after the maximum loads, and this curves indicate *ductile failure* of the bonded joints.

The brittle failures may occur during the load increase before the maximum failure point, whereas the ductile failures may occur once it had reached the maximum load. For this reason, the strength data of five specimens under each condition tend to be more scattered in the case of the brittle failure than the ductile failure. We

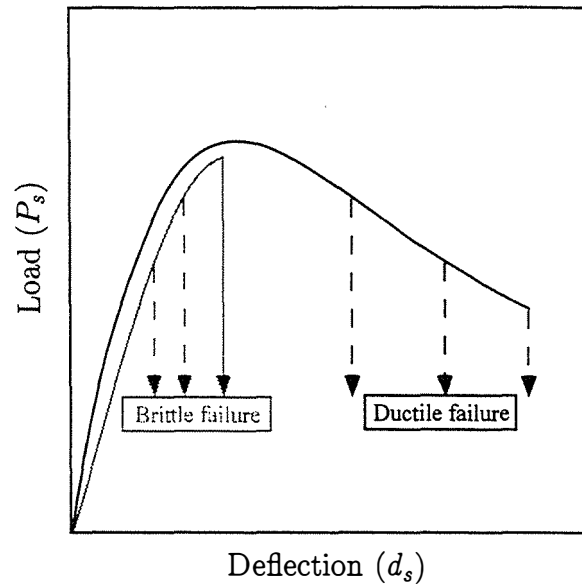


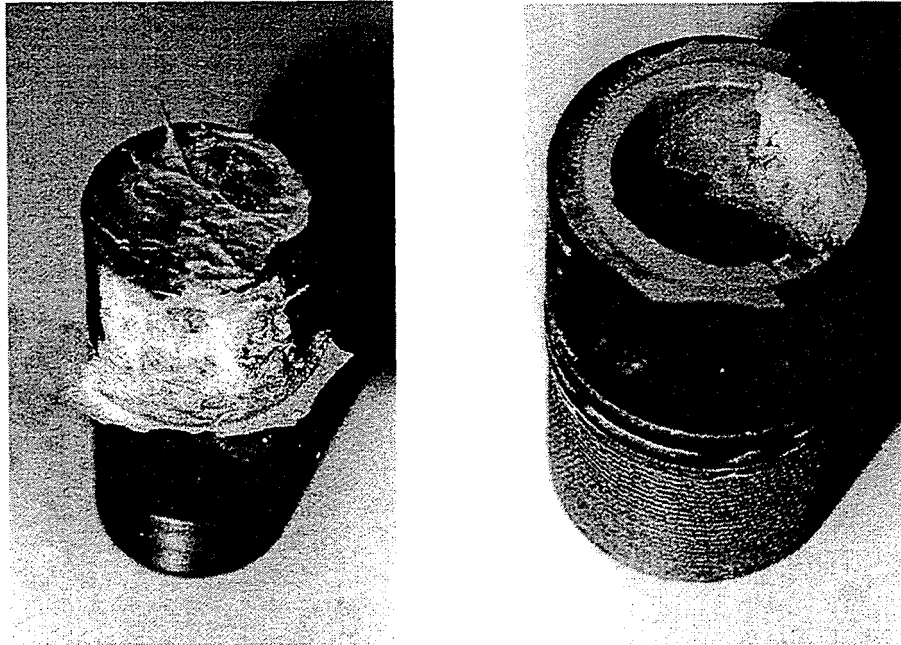
Figure 4.3: Two types of failure (brittle failure and ductile failure) categorized by load-deflection curves under static loadings.

also observed that the brittle failures occurred mainly at low temperatures and low strain-rates, whereas the ductile failures occurred mainly at low temperatures and high strain-rates.

### 4.3.2 Failure modes

We can distinguish the two types of failures not only from the load-deflection curves, as Section 4.3.1 explains, but from the failed specimens. All the specimens failed not in any of the adherends (cast-iron rod, GFRP pipe), but in the adhesive material. When a specimen had failed, we separated two adherends from each other to examine the adhesive material remaining on their surfaces. Because the bonding between polymeric materials is usually better than that between metal and polymeric material, the failed adhesive material remained less on the surface of the cast-iron rod than on the inner surface of the GFRP pipe, as shown in Figures 4.4 and 4.5.

We induced possible failure mechanisms under the static loading condition by



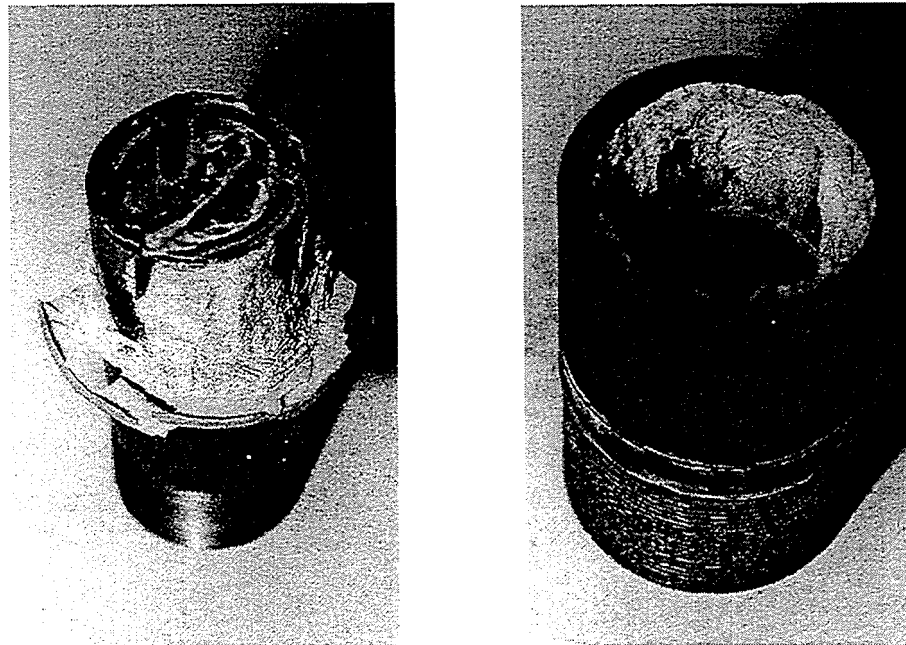
(a) Cast-iron rod

(b) GFRP pipe

Figure 4.4: A typical test specimen failed in brittle mode: Little adhesive material remained on the surface of cast-iron rod, while most adhesive material remained intact on the inner surface of GFRP pipe.

examining the bonding area on the surface of the cast-iron rod. Some portion on the surface of the cast-iron rod was still covered by the failed adhesive material, whereas the other portion was completely peeled off with little adhesive material on it. The former indicates *cohesive* failure of the adhesive material, whereas the latter indicates *interfacial* failure.

In the case of the cohesive failure, the adhesive material remained on the surface of the cast-iron rod at a slanted angle of almost  $45^\circ$ , as Figures 4.4(a) and 4.5(a) show. This cohesive failure resulted from weakness in the adhesive material when the applied load exceeded the material strength. In the meantime, the interfacial failure resulted from weakness in the interface between the adhesive material and the cast-iron rod, when concentrated stress by material discontinuity exceeded the interfacial bonding strength, even though the adhesive material still had high modulus and strength



(a) Cast-iron rod

(b) GFRP pipe

Figure 4.5: A typical test specimen failed in ductile mode: Most areas on the surface of cast-iron rod were covered by the adhesive material.

enough to carry the load. Any initial defects during fabrication caused formation and growth of the cracks under the concentrated stress. Especially, the cracks that had been formed near the ends of the overlap propagated along the interface.

Actual failures of the bonded joints occurred in brittle failure mode or ductile failure mode, as stated in Section 4.3.1. These failure modes can be explained with the combination of the cohesive failure and interfacial failure, as follows: The brittle failure tends to be more interfacial than cohesive and contains more interfacial area on the surface of the cast-iron rod, whereas the ductile failure tends to be more cohesive containing more failed adhesive material, as shown in Figures 4.4 and 4.5, respectively.

This observation is consistent with the previous categorization by the load-deflection curves in Section 4.3.1. The ductile failure is mainly a material failure, occurring at

high temperatures and low strain-rates. Because the adhesive material becomes ductile under these conditions, the load-deflection curve was drawn smoothly even after it reached the maximum failure load. Meanwhile, the brittle failure is mainly an interfacial failure, occurring at low temperatures or high strain-rates. In this failure mode, the adhesive material still has high strength but the concentrated stress becomes critical. Because the crack propagation along the interface is very fast, the load-deflection curve dropped suddenly at the maximum failure load.

Because the bonding strength between polymeric materials is usually high, it was rare to observe the interfacial failure between the GFRP pipe and the adhesive material—only one specimen out of 75 failed in this failure mode. Excluding this rare case, we considered brittle failure and ductile failure as the two main modes, and analyzed the test results based on them.

### 4.3.3 Static strength

The failures under the uni-axial tensile loadings were caused mainly by the shear stress because of the axisymmetric configuration of the bonded joint. We observed these failures mostly along the interface between the cast-iron rod and the adhesive material. Although the shear stresses are not distributed constantly along the interface but change significantly near the ends of the overlap resulting from the stress concentration, most parts of the distribution are almost constant or close to the average. For this reason, we consider this average shear stress at the moment of failure as a static failure strength by taking the bonded surface of the cast-iron rod as the average area. The static failure strength ( $S_s$ ) is then calculated by  $S_s = P_s/(\pi DL)$ , where  $P_s$  is the maximum failure load,  $D$  is the diameter of the cast-iron rod and  $L$  is the overlap length of the bonded area in the axial direction.

The average static strengths for five temperatures at each strain-rate are plotted on a temperature scale of the  $x$ -axis in Figure 4.6. In this and later figures, empty dots and solid dots indicate the brittle failure and the ductile failure, respectively. Most of the bonded joints failed in brittle mode at low temperatures, and their strengths in this mode depended little on the temperature. Meanwhile, most of the bonded

joints failed in the ductile mode at high temperatures, and the strengths decreased significantly as the temperature increased.

The static strengths for three strain-rates at five temperatures are replotted on the logged time scale of  $x$ -axis in Figure 4.7. Time to failure ( $t_s$ ) is calculated by  $t_s = d_s/v$ , where  $d_s$  is the deflection at the maximum load and  $v$  is the loading rate. Orders of magnitude of these elapsed times to failure were 0.01 min at 100 mm/min, 1 min at 1 mm/min and one to two hundred minutes at 0.01 mm/min.

At 40°C, most of the specimens failed in the brittle mode except the ones subject to long periods of loadings. Their strengths in the brittle mode are almost constant. At 50°C and 60°C, the brittle failure appeared only under short periods of loadings, and most of the specimens failed in the ductile mode under longer periods of loadings. Under these conditions, the strengths in ductile mode decreased as the loading time increased. At higher temperatures, 70°C and 80°C, only ductile failure appeared at all loading rates, and the strengths decreased significantly as the loading period increased.

From the two figures, we can draw a conclusion that the bonded joints under the static loading failed in the brittle mode at low temperatures and under short periods of loadings, whereas these failed in the ductile mode at high temperatures and during long periods of loadings. We can also conclude that the static strengths of brittle failure depend little on the temperature and the loading period, but decrease significantly as they increase. This time and temperature dependence indicates that the static strengths of the bonded joints are influenced by the viscoelasticity.

#### 4.3.4 Master curve of static strength

Averages and scatters of the static strengths for five temperatures were redrawn on a logged time scale of  $x$ -axis on the left-hand side of Figure 4.8.

After a reference temperature ( $T_0$ ) was set to 40°C, the curves at higher temperatures were shifted horizontally into that at the reference temperature. The shifted averages and scatters were drawn on the right-hand side of Figure 4.8, and the shifted data points were drawn in Figure 4.9. The data points in the ductile mode were fitted

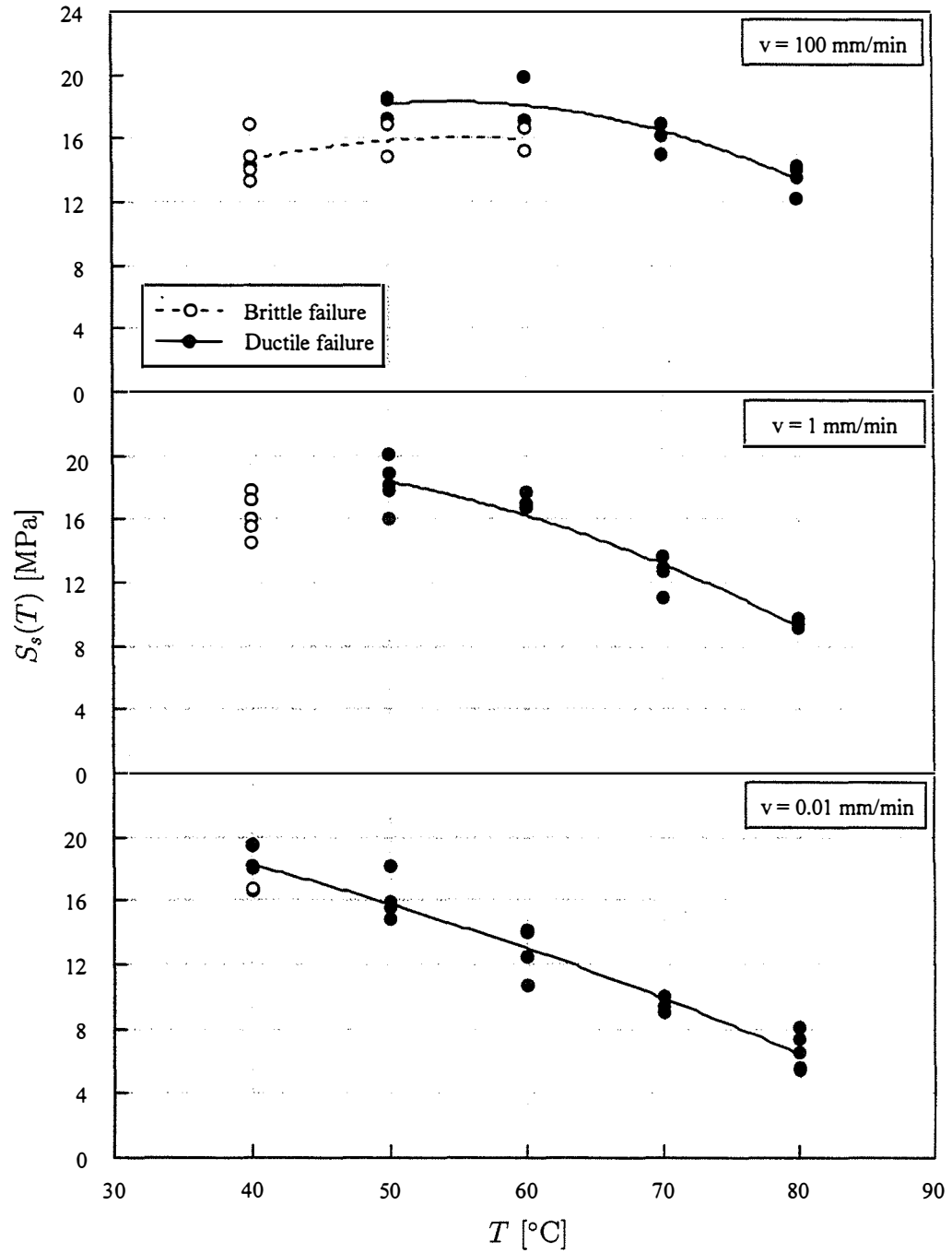


Figure 4.6: Temperature-dependent static strength of the bonded joints at three strain-rates: Empty dots and solid dots indicate the brittle failure and the ductile failure, respectively.



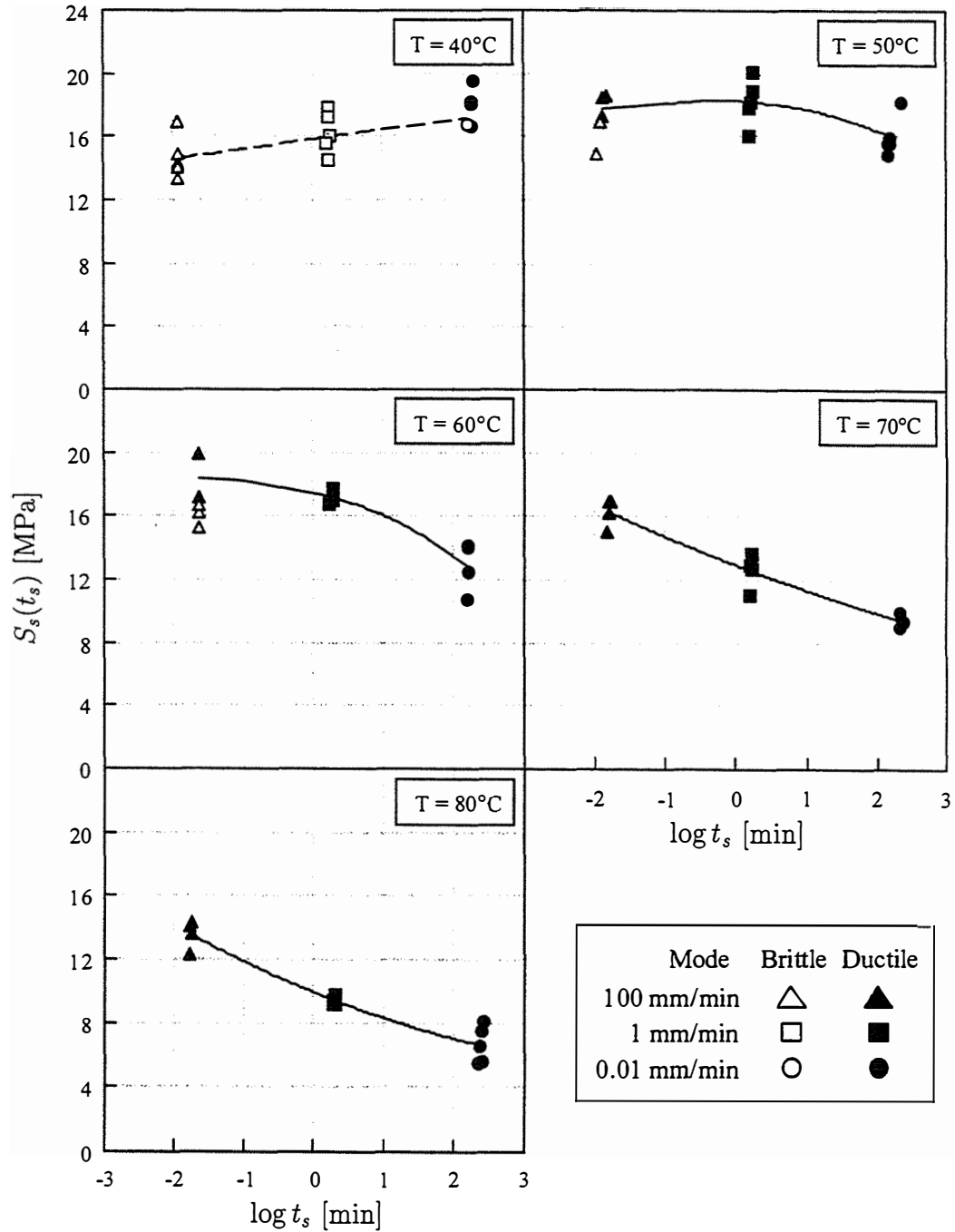


Figure 4.7: Time-dependent static strength of the bonded joints at five temperatures: Empty dots and solid dots indicate the brittle failure and the ductile failure, respectively.

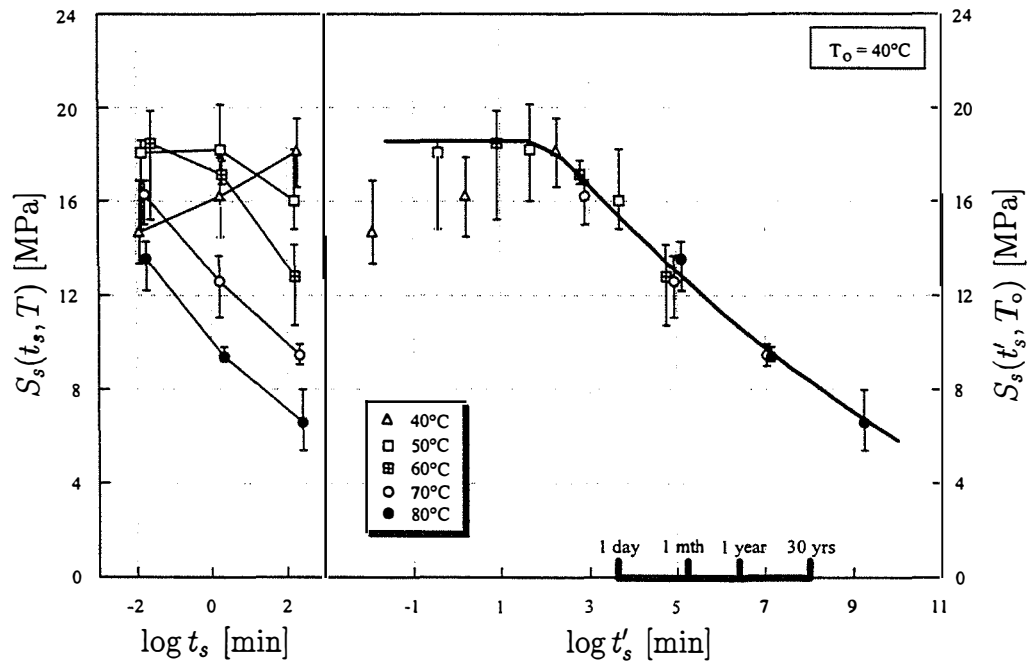


Figure 4.8: Averages and scatters of static strength data versus original and shifted time to failure. A reference temperature was set to 40°C.

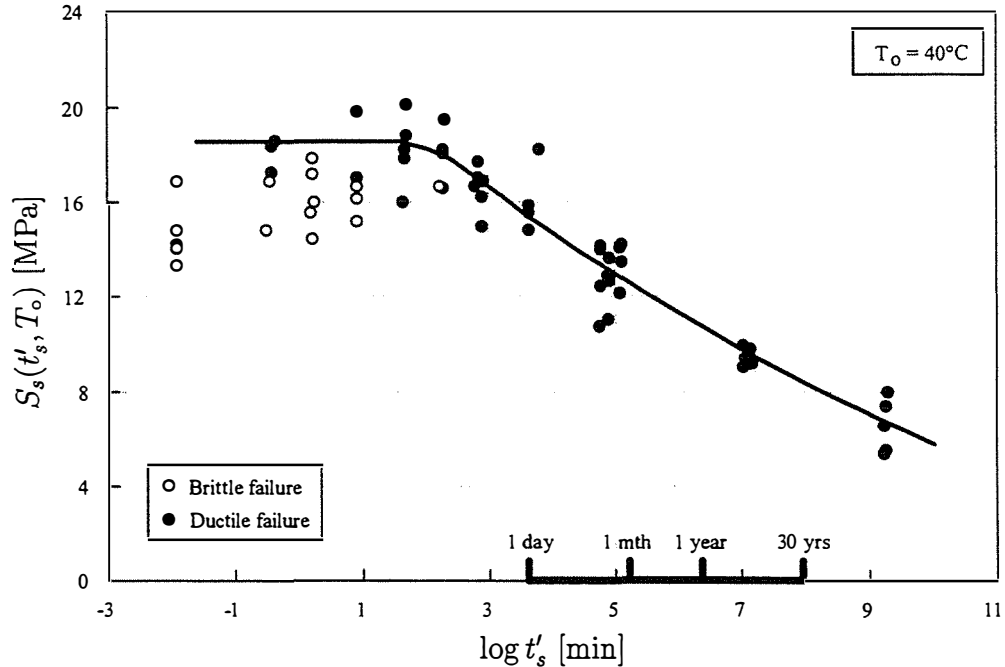


Figure 4.9: Average static strength versus shifted time to failure at a reference temperature ( $40^\circ\text{C}$ ): Master curves were drawn for the ductile failure.

with the least-square method, and a fitted curve was drawn in two figures.

Because the shifted data lie along the fitted curve fairly well and a fairly smooth curve appears, especially for the long-term period of loading, we can claim that the time-temperature equivalence can be applied for the static strength of the bonded joint. Furthermore, we can consider the fitted curve as the master curve of the static strength of the bonded joint.

Figure 4.9 shows that the brittle failure turned to ductile failure as the loading period increased when the strengths of the adhesive material became lower than the bonding strengths at the interface. When the failures were determined by the interfacial strength, the static strengths were kept almost constant or increased little during the loading period. However, when the failures were determined by the strength of the adhesive material, the static strengths decreased significantly as the loading period increased. Known these failure modes, we can conclude that the static strength

Table 4.1: Time-temperature shift factors of static strength of bonded joints.

$T$ [°C]	40	50	60	70	80
$\log a_{T_0}$	0.00	-1.45	-2.55	-4.70	-6.85

of the bonded joint is influenced by the viscoelastic behavior of the adhesive material.

We can also observe from Figure 4.9 that the strength data of the brittle failure are more scattered than those of the ductile failure. This wide scatter in the brittle failure indicates that the bonding at the interface was not well established during fabrication. This was caused by several factors such as voids and cracks, and the nonuniformity of the primer material coated on the surface of the cast-iron rod. It should be noted that it was difficult to remove these defects completely during fabrication because of the high viscosity of the adhesive material, and the extreme thinness of the primer coating.

### 4.3.5 Time-temperature shift factor

We calculated the time-temperature shift factors of the static strength by plugging the original time ( $t_s$ ) and the shifted time ( $t'_s$ ) into Eq. (3.1), and listed in Table 4.1.

These factors were plotted with solid dots on an inverse of temperature scale ( $1/T$ ) in Figure 4.10. Then we fitted these time-temperature shift factors bi-linearly to have two lines with an inflection point near the glass-transition temperature. This inflection point was also observed in creep compliance of adhesive material, as in Figure 3.7.

In Figure 4.10, solid circles indicate the time-temperature shift factors for the static strength of the bonded joint, whereas rectangles indicates those for the creep compliance of the adhesive material calculated in Section 3. Because two shift factors almost coincide, we can conclude that the time and temperature dependence of the static strength of the bonded joint were significantly influenced by that of the creep compliance of the adhesive material.

We calculated the activation energies ( $\Delta H$ ) by Eq. (3.4), and listed in Table 4.2, with those of the Adhesive III (cured under curing condition III in Section 3.3).

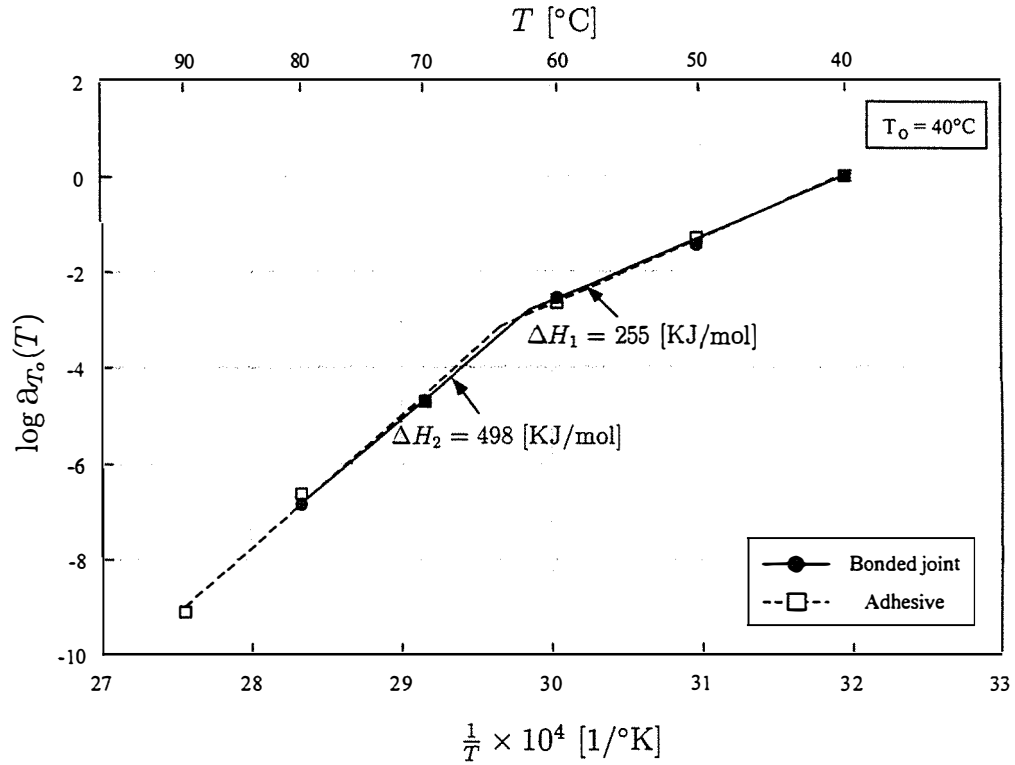


Figure 4.10: Solid lines represent the time-temperature shift factors of static strength of bonded joints, whereas dotted lines represent the time-temperature shift factors of creep compliance of AM.

Table 4.2: Activation energies of static strength of bonded joints and of creep compliance of adhesive material.

	$\Delta H_1$ [KJ/mol]	$\Delta H_2$ [KJ/mol]
Bonded joint	255	498
Adhesive III	265	526

In general, this relationship between the destructive property (static strength) and the nondestructive property (creep compliance) does not hold true for all structures and materials. However, once the relationship is verified, it is not necessary to perform the series of static tests at several temperatures and loading rates to obtain new time-temperature shift factors of the bonded joint when the adhesive material is to be changed. One can obtain the shift factors from the creep compliance tests of the new adhesive material, which are much easier tasks.

## 4.4 Conclusion

We performed uni-axial tension tests to measure the static strengths of the bonded joint. The tests were performed at five temperatures and at three strain-rates to show the dependence of temperature and time.

We observed that the static strength depended little on time at low temperatures and on temperatures at short periods of loadings. However, the time and temperature dependence became significant as the temperature and the loading period increased, which made the static strength decrease. In particular, the temperature dependence became significant above the glass-transition temperature.

When the bonding strength at the interface between the cast-iron rod and the adhesive material was weaker than the strength of the adhesive material, the bonded joints failed in the brittle type of failure mode. When the strength of the adhesive material got weaker and weaker, they were likely to fail in the ductile type of failure mode. The brittle failures were observed mostly at low temperatures and short periods of loadings, whereas the ductile failures were observed mostly at high temperatures and long periods of loadings.

The time-temperature equivalence can be applied for the static strength of the bonded joint. The time-temperature shift factors for the static strength of the bonded joint (destructive property) almost coincided with those for the creep compliance of the adhesive material (nondestructive property). This coincidence indicates that the static strength of the bonded joint is significantly influenced by the creep compliance of the adhesive material.

# Chapter 5

## Fatigue failures of bonded joints

### 5.1 Problem statement

Many structures have failed not only under static loadings but also fatigue loadings, especially when they have been subject to repeated cyclic loadings. Because of the viscoelasticity of the adhesive material, the fatigue behavior of the bonded joint is expected to depend on time and temperature, as the static behavior is, as described in Chapter 4. In this chapter, we will analyze fatigue properties of the bonded joint to understand such dependences. We performed experiments at several temperatures, frequencies and stress ratios to understand the failure mechanism and the time and temperature dependences of the fatigue behavior. Then we treated the experimental data statistically to obtain a statistical distribution of the fatigue life and to find a relationship between the fatigue and the static failure strengths.

### 5.2 Cyclic loading

The life of a structure under cyclic loadings is determined by several operational conditions, such as frequency of the cycle, maximum and minimum magnitudes of the load, etc. This life is usually represented by either number of cycles to failure ( $N_f$ ) or time to failure ( $t_f$ ). Under fixed magnitudes of the loads, the three parameters— $f$ ,

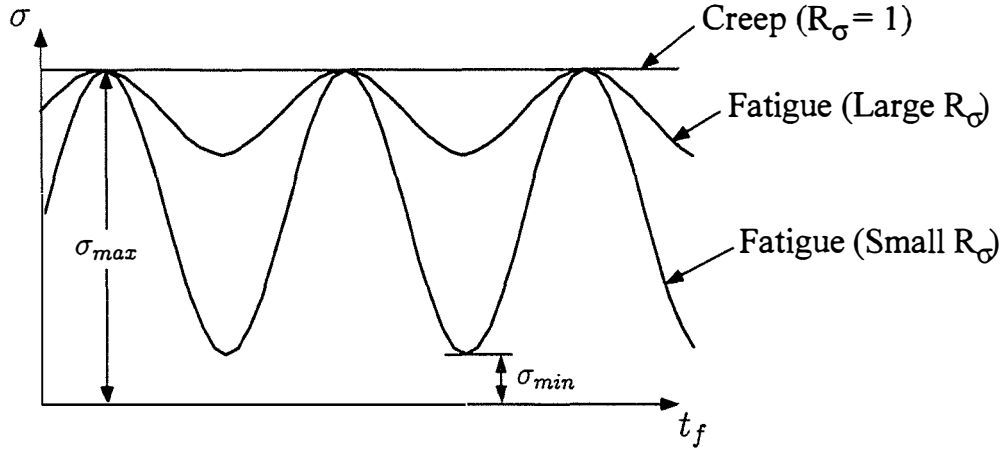


Figure 5.1: Cyclic loadings at various stress ratios ( $R_\sigma$ ).

$N_f$  and  $t_f$ —are related by

$$f = \frac{N_f}{t_f} \quad (5.1)$$

At a given  $N_f$  of the structure, the higher the frequency is, the shorter the life is.

Meanwhile, the maximum and minimum magnitudes of the load determine degree of fluctuation of the cycle, and are usually represented by one parameter—stress ratio ( $R_\sigma = \sigma_{min}/\sigma_{max}$ ). The higher the stress ratio is, the less the cycles fluctuate, as shown in Figure 5.1.

In particular, when  $R_\sigma$  is equal to one, the load becomes a constant magnitude of *creep* load. The stress ratio becomes positive under tensile-tensile or compressive-compressive cyclic loadings, and becomes negative under tensile-compressive ones. Because the tensile loadings usually have more influence on the damages in the structure because of the crack opening and propagation than the compressive loadings do, only the tensile-tensile fatigue loadings ( $0 \leq R_\sigma \leq 1$ ) were considered in this study. Also, when  $R_\sigma = 0$  and  $N_f = 1/2$ , the fatigue loading approximates a monotonically increased uni-axial tensile loading, as shown in Figure 5.2.



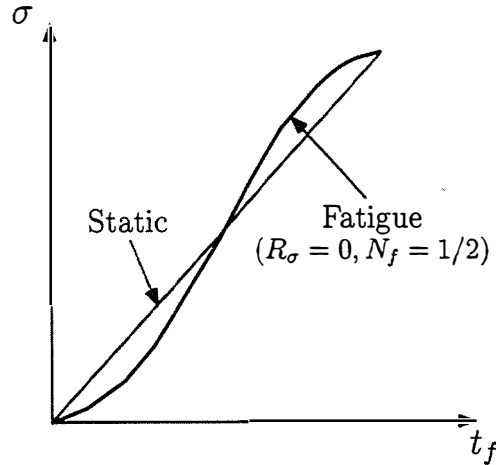


Figure 5.2: A static loading as a special case of a fatigue loading at  $R_\sigma = 0$  and  $N_f = 1/2$ .

### 5.3 Statistical analysis of fatigue data

The fatigue data can be plotted with the applied stress on one axis and the number of cycles to failure on another axis. A curve can then be drawn on this plot by fitting the data, which is called a S-N curve. Because the fatigue data usually contain large scatters, we should treat them statistically.

For the statistical analysis, the fatigue data are assumed to follow two-parameter Weibull distribution with a shape parameter ( $\alpha$ ) and a scale parameter ( $\beta$ ). These data are fitted by a modified form of the S-N curve—the K-S-N curve. And the *residual strength degradation model* is applied to calculate both *residual strength* and the statistical distribution function of the fatigue life.

#### 5.3.1 Residual strength degradation model

When a material is homogeneous, such as metal or ceramic, its fatigue behavior is characterized by initiation and propagation of a dominant crack. In this case, the fatigue life can be determined by knowing the initial size of the crack and its growing

behavior. However, when the material is not homogeneous, such as composite laminate, damages occur in the form of matrix cracking, delamination and fiber breakage, so it is difficult to identify and monitor the growth of a dominant crack that controls the fatigue behavior. In this case, statistical approaches have been introduced instead. One of these approaches is the *residual strength degradation model*.

The residual strength degradation model has been proposed by Yang et al. [13–15] to calculate a statistical distribution of fatigue life. This model has been verified for many composite laminates since then. Because the damages of the bonded joints occur in complex forms such as the cohesive failure and the interfacial failure, which are similar to the complex damages of the composite laminates (matrix cracking and delamination), we tried to apply this residual strength degradation model to characterize the fatigue behavior of the bonded joints.

This model was proposed based on an assumption that there must be a close relation between the static strength and the fatigue strength, such as

- Statically strong specimens must also be strong under fatigue loadings.
- The scatter of the static data has a strong influence on that of the fatigue data.

According to this model, the static strength is considered as a fatigue strength when the test specimen fails at zero number of cycle ( $N = 0$ ) under the fatigue loading—strictly speaking, it fails at  $N = N_f - 1/2 = 0$  when it takes the half cycle to reach the maximum. When the fatigue loading is applied at a lower stress level than the static strength, the initial (static) strength of the specimen degrades as the number of fatigue cycles ( $n$ ) increases. The degraded strength remaining in the test specimen when the fatigue test stops at a certain number of cycles ( $n \leq N$ ) is called *residual strength* ( $\mathcal{R}(n)$ ).

Previous experiments on composite laminates under the fatigue loadings [14, 16] showed that the residual strength decreased monotonically as the number of fatigue cycles ( $n$ ) increased, which leads to

$$\frac{d\mathcal{R}(n)}{dn} = -\frac{f(S, R_\sigma)}{c} \mathcal{R}(n)^{c-1} \quad (5.2)$$

where  $S$  is the stress range ( $\sigma_{max} - \sigma_{min}$ ),  $R_\sigma$  is the stress ratio ( $\sigma_{min}/\sigma_{max}$ ),  $c$  is a constant to be determined and  $f(S, R_\sigma)$  is a function of  $S$  and  $R_\sigma$ . Integrating Eq. (5.2) from 0 to  $n$  cycles, one obtains

$$\mathcal{R}(n)^c = \mathcal{R}(0)^c - f(S, R_\sigma) n \quad (5.3)$$

This equation shows that as the number of cycles increases, the residual strength decreases from the initial (static) strength ( $\mathcal{R}(0)$ ), depending on the function,  $f(S, R_\sigma)$ . The constant ( $c$ ) determines the shape of the degradation of the residual strength, and is obtained from the experimental data.

Assuming that the fatigued specimen failed when its residual strength is reduced to reach the applied maximum stress level ( $\sigma_{max}$ ), the number of cycles to fatigue failure ( $N$ ) can be calculated by imposing the fracture conditions ( $\mathcal{R}(n) = \sigma_{max}$  and  $n = N$ ) into Eq. (5.3), as follows:

$$N = \frac{\mathcal{R}(0)^c - \sigma_{max}^c}{f(S, R_\sigma)} \quad (5.4)$$

Under the reasonable assumption [13, 16] that the initial static strength ( $\mathcal{R}(0)$ ) follows a two-parameter Weibull distribution, the statistical distribution of the static strength can then be expressed as

$$F_{\mathcal{R}(0)}(x) = \mathbb{P}[\mathcal{R}(0) \leq x] = 1 - \exp[-(\frac{x}{\beta_s})^{\alpha_s}] \quad (5.5)$$

where  $F_{\mathcal{R}(0)}(x)$  is the probability of the static strength being lower than  $x$ . In this equation,  $\alpha_s$  and  $\beta_s$  are the shape and the scale parameters of the Weibull distribution for the static strength. The scale parameter ( $\beta_s$ ) scales the static strength ( $x$ ), and is also called *characteristic* static strength. Because the static strength is assumed to be a statistical variable, the number of cycles to fatigue failure ( $N$ ) is also assumed to be the statistical variable from Eq. (5.4). The statistical distribution function of the fatigue life can then be expressed by Eq. (5.4) and Eq. (5.5), as follows:

$$F_N(n) = \mathbb{P}[N \leq n]$$

$$\begin{aligned}
&= \mathbb{P}\{[\mathcal{R}(0)^c - \sigma_{max}^c]/f(S, R_\sigma) \leq n\} \\
&= \mathbb{P}\{\mathcal{R}(0) \leq \{nf(S, R_\sigma) + \sigma_{max}^c\}^{1/c}\} \\
&= 1 - \exp\left\{-\left[\frac{n + \sigma_{max}^c/f(S, R_\sigma)}{\beta_s^c/f(S, R_\sigma)}\right]^{\alpha_s/c}\right\}
\end{aligned} \tag{5.6}$$

where  $F_N(n)$  is the probability of the fatigue life being lower than  $n$ . Eq. (5.6) indicates that the statistical distribution of fatigue life follows a three-parameter Weibull distribution with a shape parameter  $(\alpha_s/c)$ , a scale parameter  $(\beta_s^c/f(S, R_\sigma))$  and a lower bound  $(-\sigma_{max}^c/f(S, R_\sigma))$ .

If we consider a case under a low stress-level loading condition such that  $(\sigma_{max}/\beta_s)^c \ll 1$ , Eq. (5.6) can be approximated as [13]

$$F_N(n) \simeq 1 - \exp\left\{-\left[\frac{n}{\beta_s^c/f(S, R_\sigma)}\right]^{\alpha_s/c}\right\} \tag{5.7}$$

indicating that the statistical distribution of fatigue life approximately follows a two-parameter Weibull distribution with the shape parameter  $(\alpha_s/c)$  and the scale parameter  $(\beta_s^c/f(S, R_\sigma))$ . In this equation, the scale parameter  $(\beta_s^c/f(S, R_\sigma))$  scales the fatigue life ( $n$ ), and is also called *characteristic* fatigue life.

Meanwhile, we assume that the fatigue data are fitted by a K-S-N curve, which is a modified S-N curve, such as

$$KS^bN^* = 1 \tag{5.8}$$

where  $N^*$  is the characteristic life at the stress range ( $S$ ), and  $b$  and  $K$  are constants. This equation can be written as

$$N^* = \frac{1}{KS^b} \tag{5.9}$$

Comparison of the characteristic lives in Eq. (5.7) and in Eq. (5.9) results in

$$\beta_s^c/f(S, R_\sigma) = \frac{1}{KS^b} \tag{5.10}$$

and in turn determines the function ( $f(S, R_\sigma)$ ), as follows:

$$f(S, R_\sigma) = \beta_s^c K S^b \quad (5.11)$$

The residual strength and the number of cycles to fatigue failure under the constant-amplitude cyclic loadings can be calculated by substituting Eq. (5.11) into Eq. (5.3) and Eq. (5.4), as follows:

$$\mathcal{R}(n)^c = \mathcal{R}(0)^c - \beta_s^c K S^b n \quad (5.12)$$

and

$$N = \frac{\mathcal{R}(0)^c - \sigma_{max}^c}{\beta_s^c K S^b} \quad (5.13)$$

where the constants ( $c$ ,  $b$  and  $K$ ) are determined from the experimental data.

We must note that Eqs. (5.12) and (5.13) are derived on the assumption of

$$(\sigma_{max}/\beta_s)^c \ll 1 \quad (5.14)$$

When  $(\sigma_{max}/\beta_s)^c$  is not negligible, it can be shown in a similar fashion [13] that the residual strength degradation model still leads to the same form as Eqs. (5.12) and (5.13), except that the constants ( $K$  and  $b$ ) have different values.

From Eqs. (5.6) and (5.13), the statistical distribution function of fatigue life can be expressed as follows:

$$\begin{aligned} F_N(n) &= P[N \leq n] = P[\{\mathcal{R}(0) \leq (n\beta_s^c K S^b + \sigma_{max}^c)^{1/c}\}] \\ &= 1 - \exp \left\{ - \left[ \frac{n + (\sigma_{max}^c / \beta_s^c K S^b)}{1/K S^b} \right]^{\alpha_s/c} \right\} \end{aligned} \quad (5.15)$$

Because it is physically impossible to have a negative fatigue life, Eq. (5.15) should

be rewritten as [13]

$$F_N(n) = \begin{cases} 0 & \text{for } n < 0 \\ 1 - \exp \left\{ - \left[ \frac{n + (\sigma_{max}^c / \beta_s^c K S^b)}{1/K S^b} \right]^{\alpha_s / c} \right\} & \text{for } n \geq 0 \end{cases} \quad (5.16)$$

### 5.3.2 Determination of $c$ , $b$ , $K$

The constants in Eqs. (5.12) and (5.13) are determined by the experimental fatigue data. There are several methods of determining the constants, such as *maximum likelihood method* and *minimization technique* [13]. The former method is used in this study.

#### Static Weibull parameters

Suppose that the static tests were performed at a certain temperature ( $T$ ) at  $k$  loading rates ( $v_i$  for  $i = 1, 2, \dots, k$ ). Let the number of test specimens at a loading rate ( $v_i$ ) be  $l_i$ , and the static data (static strength) be  $X_{i1}, X_{i2}, \dots, X_{il_i}$  for  $i = 1, 2, \dots, k$ .

At the temperature ( $T$ ), the static strengths are assumed to follow two-parameter Weibull distribution with a shape parameter ( $\alpha_{si}$ ) and a scale parameter ( $\beta_{si}$ ) at the loading rate ( $v_i$ ). Even though the two parameters usually have different values at different loading rates, the shape parameter is assumed to be independent of the loading rates, so that only one shape parameter ( $\alpha_s$ ) represents all loading rates at the temperature.

With normalized static data ( $Y_{ij}$ ) as

$$Y_{ij} = \frac{X_{ij}}{\beta_{si}} \quad \text{for } i = 1, 2, \dots, k \quad (5.17)$$

the maximum likelihood equation is derived as follows [13]:

$$\frac{\sum_{i=1}^k \sum_{j=1}^{l_i} Y_{ij}^{\alpha_s} \ln Y_{ij}}{\sum_{i=1}^k \sum_{j=1}^{l_i} Y_{ij}^{\alpha_s}} - \frac{1}{\alpha_s} - \frac{\sum_{i=1}^k \sum_{j=1}^{l_i} \ln Y_{ij}}{\sum_{i=1}^k l_i} = 0 \quad (5.18)$$

and

$$\beta_{si} = \left[ \frac{1}{l_i} \sum_{j=1}^{l_i} X_{ij}^{\alpha_s} \right]^{1/\alpha_s} \quad \text{for } i = 1, 2, \dots, k \quad (5.19)$$

The shape parameter ( $\alpha_s$ ) and the scale parameters ( $\beta_{si}$ ) can then be calculated by solving Eqs. (5.18) and (5.19), with iteration techniques such as a Newton-Raphson method.

### Fatigue Weibull parameters

Suppose that the fatigue tests were performed at a certain temperature ( $T$ ) at  $m$  stress levels ( $S_i$  for  $i = 1, 2, \dots, m$ ). Let the number of the test specimens at a stress level ( $S_i$ ) be  $n_i$ , and the fatigue data (number of cycles to fatigue failure) be  $N_{i1}, N_{i2}, \dots, N_{in_i}$  for  $i = 1, 2, \dots, m$ .

Eq. (5.7) indicates that the fatigue data follow two-parameter Weibull distribution. Even though the shape parameter ( $\alpha_{fi}$ ) and the scale parameter ( $\beta_{fi}$ ) usually have different values at different stress levels ( $S_i$ ), the shape parameter is assumed to be independent of the stress levels, so that only one shape parameter ( $\alpha_f$ ) represents all stress levels at the temperature.

With normalized fatigue data ( $M_{ij}$ ) as

$$M_{ij} = \frac{N_{ij}}{\beta_{fi}} \quad \text{for } i = 1, 2, \dots, m \quad (5.20)$$

the maximum likelihood equation is derived as follows [13]:

$$\frac{\sum_{i=1}^m \sum_{j=1}^{n_i} M_{ij}^{\alpha_f} \ln M_{ij}}{\sum_{i=1}^m \sum_{j=1}^{n_i} M_{ij}^{\alpha_f}} - \frac{1}{\alpha_f} - \frac{\sum_{i=1}^m \sum_{j=1}^{n_i} \ln M_{ij}}{\sum_{i=1}^m n_i} = 0 \quad (5.21)$$

and

$$\beta_{fi} = \left[ \frac{1}{n_i} \sum_{j=1}^{n_i} N_{ij}^{\alpha_f} \right]^{1/\alpha_f} \quad \text{for } i = 1, 2, \dots, m \quad (5.22)$$

The shape parameter ( $\alpha_f$ ) and the scale parameters ( $\beta_{fi}$ ) can then be calculated by solving Eqs. (5.21) and (5.22), by the similar iteration techniques as in the static case.

### Constants, $c$ , $b$ and $K$

The constants,  $b$  and  $K$ , can be determined from the S-N curve equation in Eq. (5.8). In the equation, we can replace the characteristic fatigue life ( $N^*$ ) at a stress level ( $S_i$ ) with the scale parameter ( $\beta_{fi}$ ) of the fatigue Weibull distribution function, obtained from Eq. (5.22). By taking natural logarithms on Eq. (5.8), we can obtain

$$\ln \beta_{fi} = -b \ln S_i - \ln K \quad \text{for } i = 1, 2, \dots, m \quad (5.23)$$

The values of  $b$  and  $K$  can then be calculated with the fatigue data by a least-square linear-regression method.

The constant,  $c$ , can be determined by comparing the shape parameter ( $\alpha_f$ ) of the fatigue Weibull distribution function with the one in Eq. (5.7), which leads to

$$c = \frac{\alpha_s}{\alpha_f} \quad (5.24)$$

where  $\alpha_s$  is the shape parameter of the static Weibull distribution function obtained from Eq. (5.18).

## 5.4 Test conditions

For a fatigue test, we applied a uni-axial tensile-tensile cyclic loading to the ends of the bonded joint at a temperature, a frequency and a stress ratio. The screwed ends of the test specimen were held by grips of a Shimazu servo-pulsar testing machine,



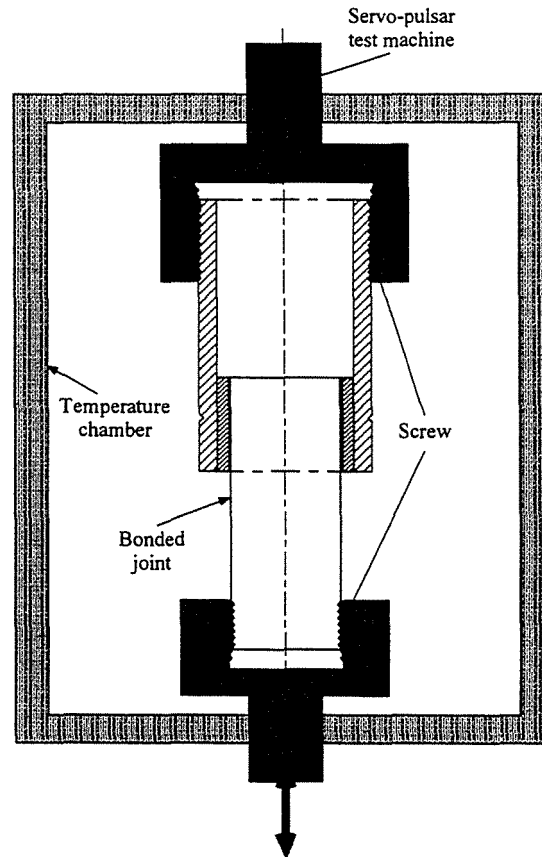


Figure 5.3: Configuration for fatigue tests under uni-axial tensile-tensile cyclic loading: Both ends of test specimen were screwed and held by grips of a Servo-pulsar testing machine.

which is located at Kanazawa Institute of Technology in Japan, as shown in Figure 5.3. Both the grips and the specimen were placed in a temperature chamber. The bonded joint was placed in the temperature chamber for an additional 30 minutes after the temperature met the test condition. The cyclic loadings were input in a sine wave form.

We selected four series of test conditions, as listed in Table 5.1. At each test condition, three or four maximum load levels were selected, and at each stress level, three to five specimens were tested to measure the number of cycles to fatigue failure.

Table 5.1: Test conditions and number of specimens for tests under cyclic loadings.

Series	$f$ [Hz]	$R_\sigma$	$T$ [°C]	No. of specimens
I		0.05	40, 50, 60, 70, 80	74
II	5	0.5	40, 70	27
III		0.95	40, 70	14
IV	0.05	0.05	61.9	15

The total number of specimens were 130.

Because of frictional heating during the cyclic loadings, the temperature of the specimens usually rises, especially at high frequencies. Because the properties of the adhesive material depend significantly on the temperature, it was necessary to measure its accurate temperature in addition to the chamber temperature, as the chamber temperature was measured away from the test specimen. We attached a thermocouple to one end of the bonding area to measure the temperature of the test specimen. At the high-frequency tests, there were temperature increases up to 1.5°C, which means that the actual temperature of the adhesive material is slightly higher than that listed in Table 5.1.

## 5.5 Test results

### 5.5.1 Failure modes

After examining the failed specimens, we were able to observe the failures similar to those observed under the static loadings—cohesive failure and interfacial failure. The actual fatigue failure modes of the bonded joints (brittle failure and ductile failure) occurred with the combination of these cohesive and interfacial failures. Although most of the specimens failed in the ductile mode, some specimens failed in the brittle mode at low temperatures and high frequencies.

As in the static loading case, because the bonding strength between polymeric materials is usually high in the fatigue loading case, we rarely observed the interfacial failure between the GFRP pipe and the adhesive material—only two specimens out

Table 5.2: Constants,  $c$ ,  $b$  and  $K$ .

$f$ [Hz]	$R_\sigma$	$T$ [°C]	$c$	$b$	$K$	$\alpha_s$	$\alpha_f$
5	0.05	40	16.55	16.19	9.56E-21	14.09	0.84
		50	11.67	16.78	1.79E-21	14.51	1.24
		60	12.27	16.14	7.18E-21	13.38	1.09
		70	20.04	11.01	2.92E-14	24.75	1.24
		80	10.40	9.40	1.94E-11	10.31	0.99
0.05	0.05	61.9	16.04	10.98	2.59E-14		0.83
5	0.95	70	22.91	13.29	0.411		1.08
	0.5	40	7.64	3.86	1.52E-08		1.82
	0.5	70	24.25	12.24	7.00E-14		1.02

of 129 failed in this failure mode. Excluding this rare case, we considered the brittle failure and the ductile failure as the two main modes, and analyzed the test results based on them.

### 5.5.2 Fatigue strength and S-N curve

The failures under the uni-axial tensile-tensile cyclic loadings were caused mainly by the shear stress resulting from the axisymmetric configuration of the bonded joint. For this reason, we can observe the failure mostly along the interface between the cast-iron rod and the adhesive material, as explained earlier. Using the analogy of the static loading case in Chapter 4, we can consider the average shear stress at the maximum load level as a fatigue failure strength ( $S_f$ ). This fatigue failure strength can be calculated by  $S_f = P_f/(\pi DL)$ , where  $P_f$  is the maximum load level,  $D$  is the diameter of the cast-iron rod, and  $L$  is the overlap length of the bonded area in the axial direction.

The constants ( $c$ ,  $b$  and  $K$ ) of the K-S-N curves are evaluated by the method explained in Section 5.3.2. These constants and the Weibull shape parameters of the static and fatigue data ( $\alpha_s$  and  $\alpha_f$ ) under each condition are listed in Table 5.2.

Figures 5.4 to 5.7 show the fatigue data and the corresponding K-S-N curves under each test series. The  $y$ -axis and  $x$ -axis indicate the average fatigue strength and the number of cycles to failure on the logged scale, respectively. In these figures, empty

dots and solid dots indicate the brittle failure and the ductile failure, respectively.

Figure 5.4 shows the results for Series I, which were tested at five temperatures from 40°C to 80°C, at a high frequency ( $f = 5$  Hz) and a low stress ratio ( $R_\sigma = 0.05$ ). The brittle failure appeared at some load levels at low temperatures (40°C and 50°C), whereas only ductile failure appeared at all stress levels at higher temperatures (60°C, 70°C and 80°C).

Figure 5.5 shows the results for Series II, which were tested at two temperatures (40°C and 70°C) at  $f = 5$  Hz and  $R_\sigma = 0.5$ ; only ductile failure appeared at all load levels.

Figure 5.6 shows the data for Series III, which were tested at two temperatures (40°C and 70°C) at  $f = 5$  Hz and  $R_\sigma = 0.95$ . At 40°C, only two data points were available at one load level; most of the specimens failed during load increase to the maximum load level, and two specimens were run out after one million cycles under this condition. When the maximum load level was set higher, the test specimens failed immediately: When the maximum load level was set lower, they survived after one million cycles. This explains that the test specimens failed dominantly in the brittle failure mode at the low temperature (40°C). However, this result did not happen at the high temperature (70°C), when all the specimens failed in ductile failure mode at all load levels.

Figure 5.7 shows the results for Series IV, which were tested at 61.9°C at a low frequency ( $f = 0.05$  Hz) and  $R_\sigma = 0.05$ . Only ductile failure occurred at all load levels. Two specimens that were tested at a low load level were run out after  $10^6$  number of cycles.

### 5.5.3 Dependence of fatigue strength

The K-S-N curves of the fatigue data at five temperatures at  $f = 5$  Hz and  $R_\sigma = 0.05$  are plotted together in Figure 5.8. The curves extend backwards to the points at  $N_f = 1/2$ , when the first cycle reaches a maximum load level. With  $R_\sigma = 0.05 \approx 0$ , these points approximately represent the static failure strengths as explained in Section 5.2. The curves change little at the temperatures below 60°C, which is near

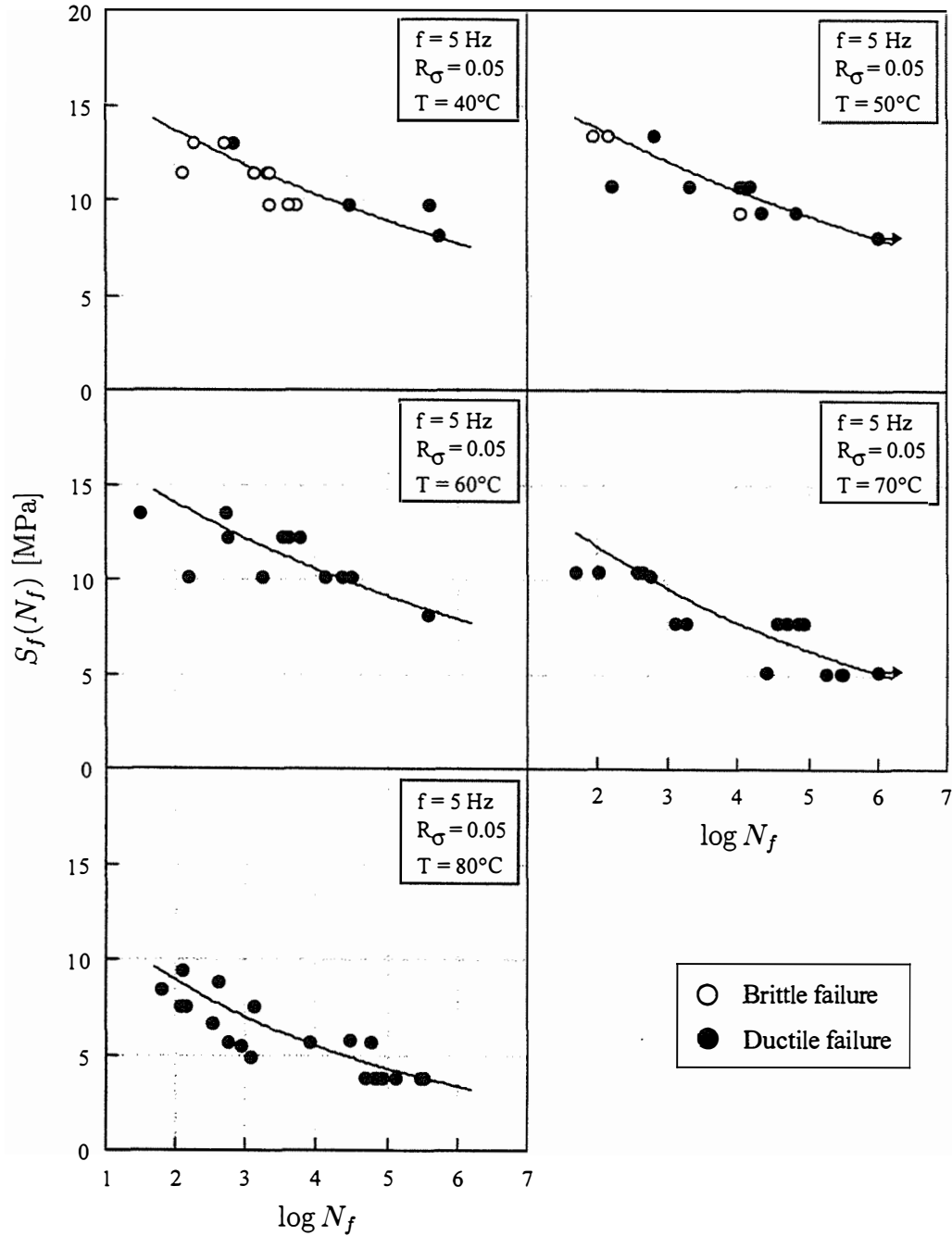


Figure 5.4: Fatigue test data in Series I: At five temperatures from  $40^\circ\text{C}$  to  $80^\circ\text{C}$  with  $10^\circ\text{C}$  increments at a high frequency ( $f = 5$  Hz) and a low stress ratio ( $R_\sigma = 0.05$ ).

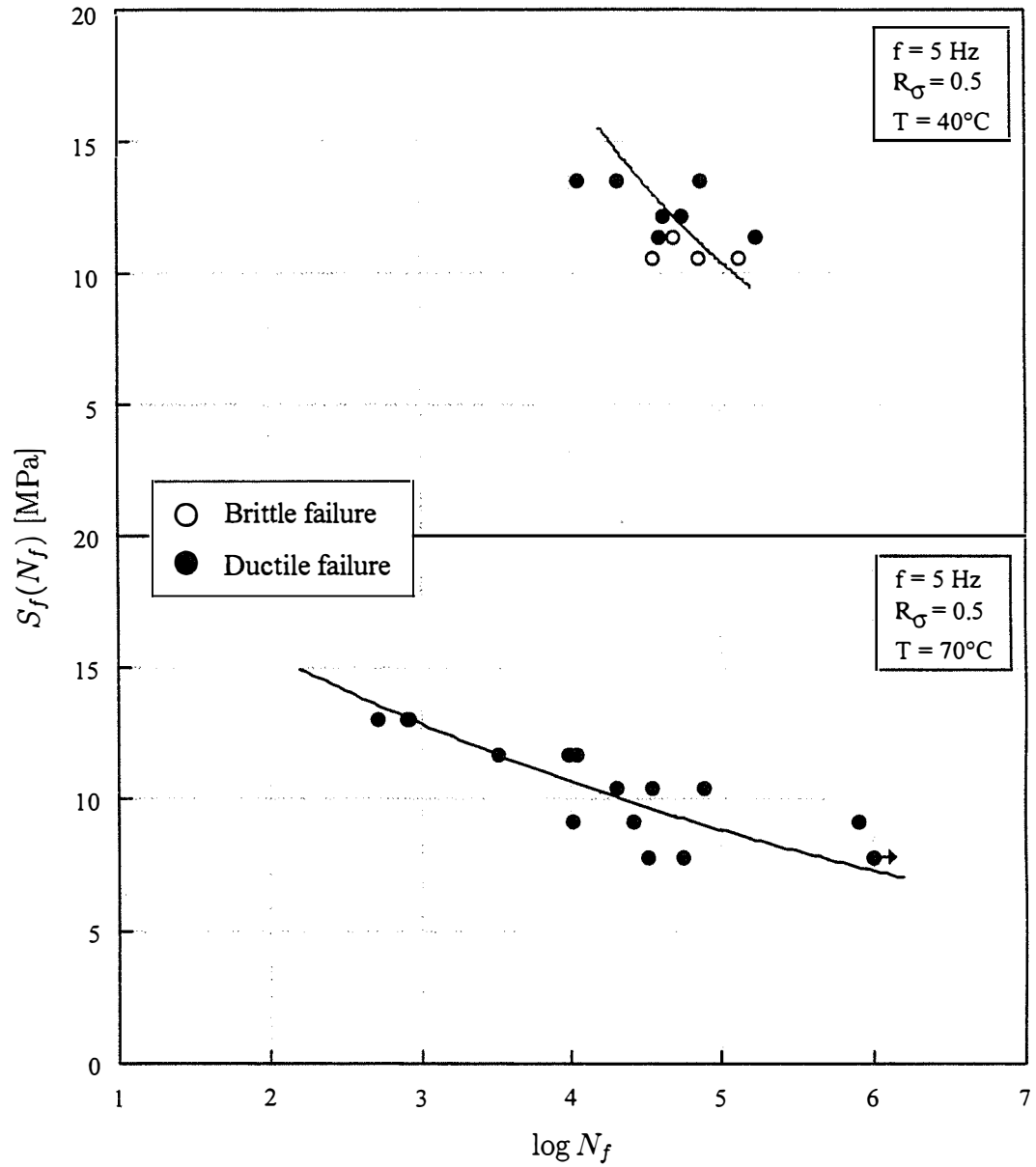


Figure 5.5: Fatigue test data in Series II: At two temperatures ( $40^\circ\text{C}$  and  $70^\circ\text{C}$ ) at  $f = 5\text{ Hz}$  and a high stress ratio ( $R_\sigma = 0.5$ ).

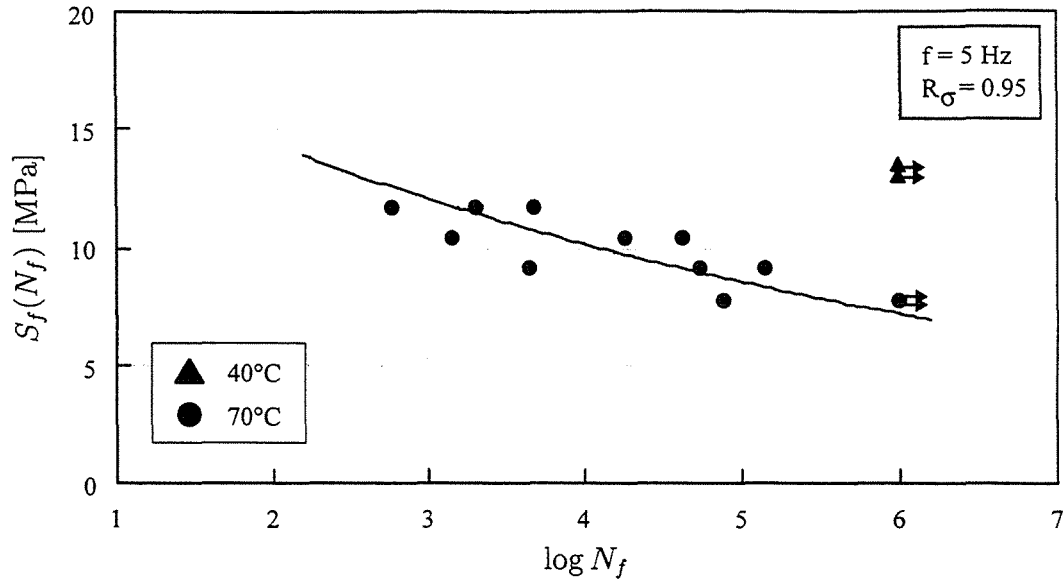


Figure 5.6: Fatigue test data in Series III: At two temperatures (40°C and 70°C) at  $f = 5$  Hz and a high stress ratio ( $R_\sigma = 0.95$ ).

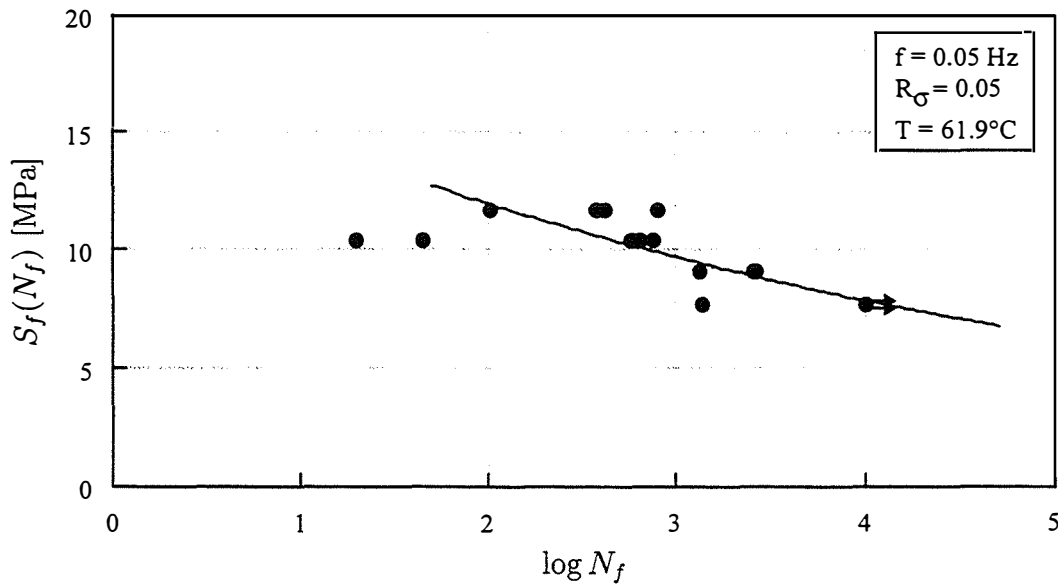


Figure 5.7: Fatigue test data in Series IV: At one temperature (61.9°C) at a low frequency ( $f = 0.05$  Hz), and  $R_\sigma = 0.05$ .

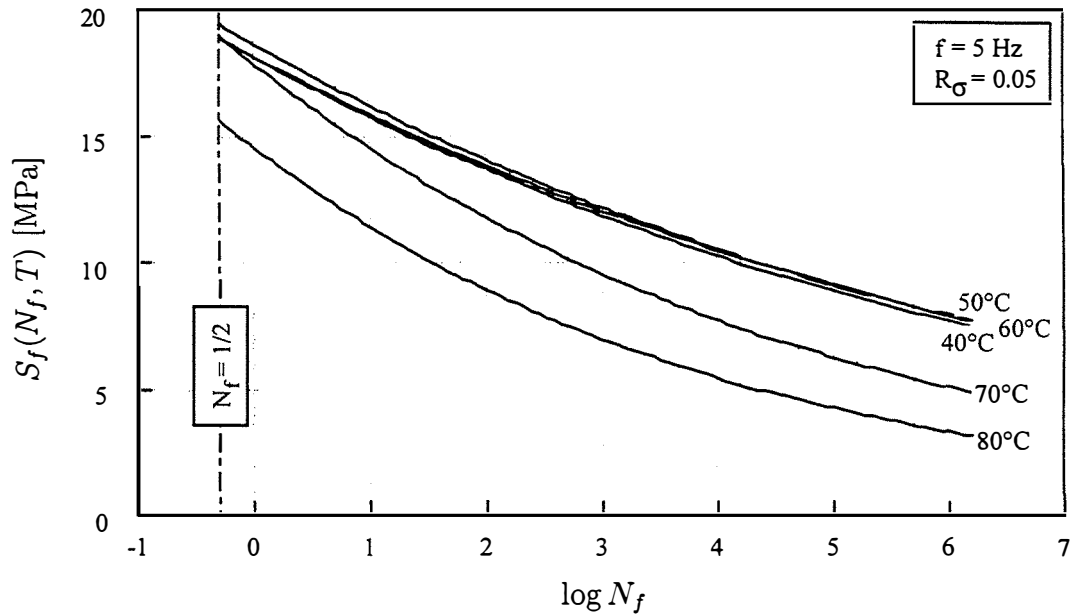


Figure 5.8: Temperature-dependent behavior of fatigue strength of bonded joints.

the glass-transition temperature. However, the curves decrease significantly at higher temperatures of 70°C and 80°C. This shows that the fatigue strength of the bonded joint under the cyclic loading is hardly affected by the temperature below the glass-transition temperature when many specimens failed in brittle mode. However, the fatigue strength depends significantly on the temperature over the glass-transition temperature when the failure occurred mainly in the ductile mode.

The K-S-N curve for the low-frequency fatigue data ( $f = 0.05 \text{ Hz}$ ) are plotted together with those for the high-frequency data ( $f = 5 \text{ Hz}$ ) in Figure 5.9. The curve for the low-frequency data at 61.9°C is drawn more closely to that for the high-frequency data at 70°C rather than at 60°C. This figure shows the frequency dependence of the fatigue strength.

Figure 5.10 shows the K-S-N curves at three different stress ratios,  $R_\sigma = 0.05, 0.5, 0.95$  at  $f = 5 \text{ Hz}$  and two temperatures (40°C and 70°C). The curves at 40°C were drawn distinctively as the stress ratio changes. These curves decrease significantly as the stress ratio decreases under more fluctuating cyclic loading conditions. At 70°C,



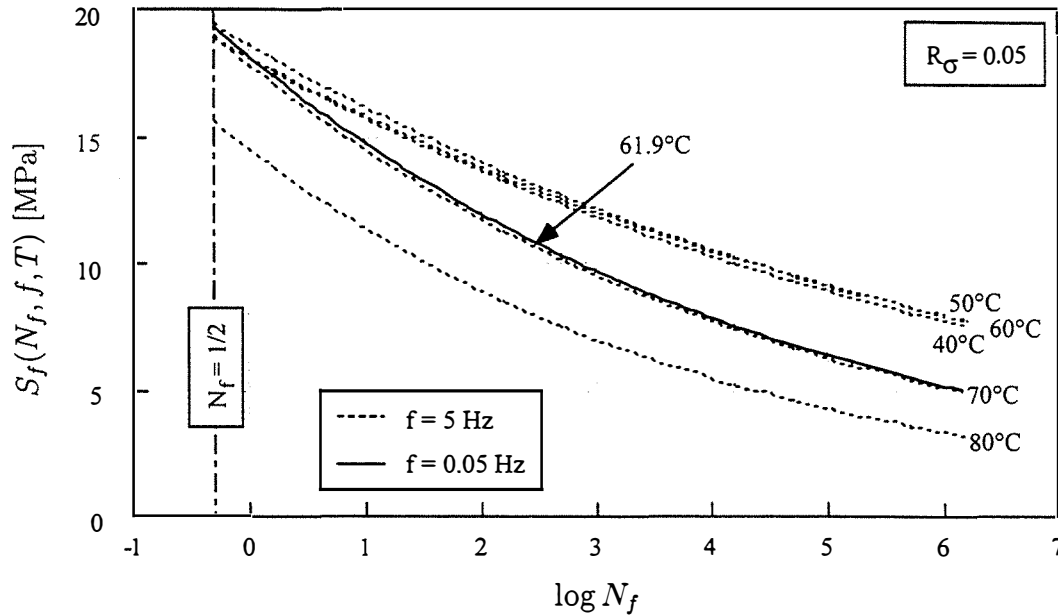


Figure 5.9: Frequency-dependent behavior of fatigue strength of bonded joints.

however, the curves at  $R_\sigma = 0.5$  and  $0.95$  were drawn closely together, but distinctively from the curve at  $R_\sigma = 0.05$ . These figures indicate that the fatigue strength also depends on the stress ratio, but the degree of the dependency changes with the temperature.

#### 5.5.4 Scatter of fatigue data

Although we can determine the characteristic fatigue lives by the K-S-N curves at any stress levels, we found that the actual test data are scattered away from the curves. We can determine the degree of these scatters by the residual strength degradation model, as explained in Section 5.3.1.

According to the model, the scatter of the fatigue strength results from that of the static strength. The residual strength of the test specimen, which fails at the first maximum load level ( $N_f = 1/2$  or  $N = 0$ ) under the cyclic loading at  $R_\sigma = 0$ , can be considered as a static strength. We also call this residual strength an *equivalent* static strength. This equivalent static strength ( $\mathcal{R}(0)$ ) can be calculated from Eq. (5.12) by

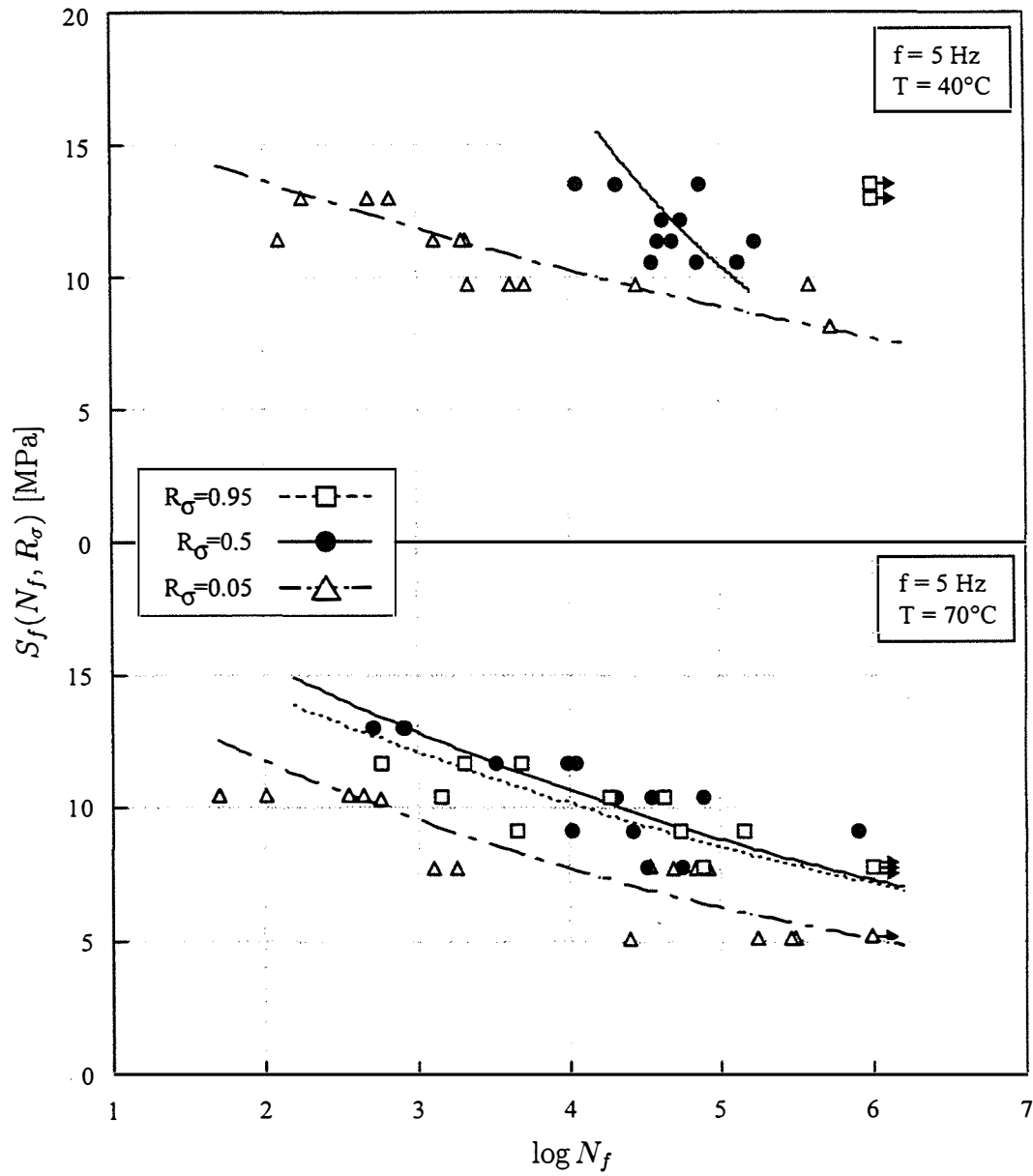


Figure 5.10: Average fatigue strength versus time to fatigue failure at  $f = 5$  Hz,  $R_\sigma = 0.5$  and two temperatures ( $40^\circ\text{C}$  and  $70^\circ\text{C}$ ).

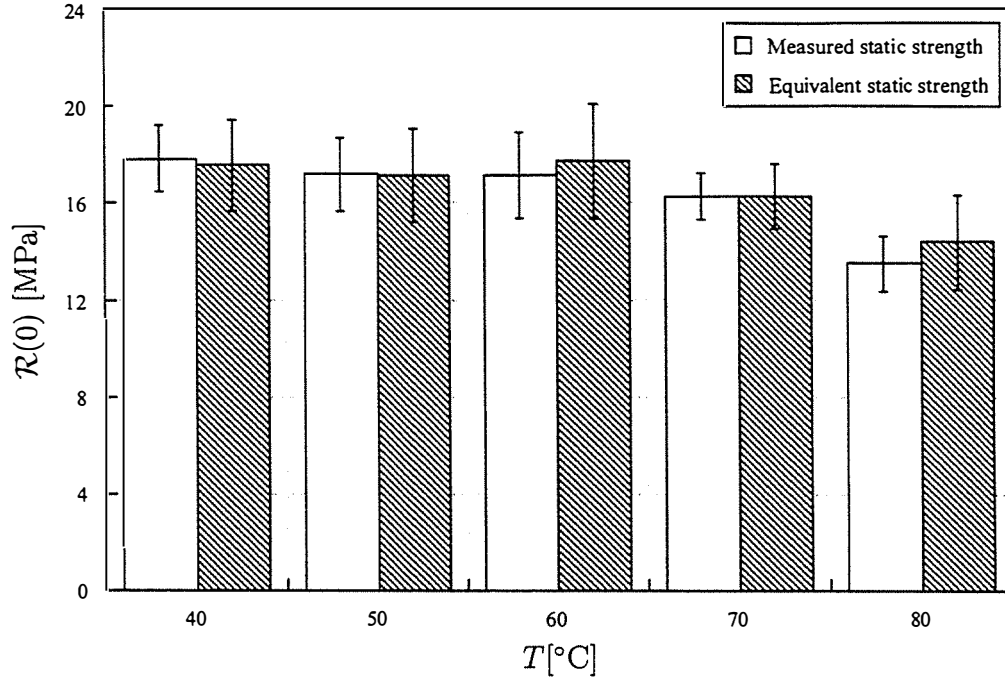


Figure 5.11: Measured static strength and equivalent static strength calculated from fatigue data at five temperatures from 40°C to 80°C at  $f = 5$  Hz and  $R_\sigma = 0.05$ .

setting  $\mathcal{R}(n) = \sigma_{max}$  and  $n = N$ , which leads to

$$\mathcal{R}(0) = [\sigma_{max}^c + \beta^c K \sigma_{max}^b N]^{1/c} \quad (5.25)$$

Figure 5.11 shows averages and scatters of these equivalent static strengths for the fatigue data at five temperatures at  $f = 5$  Hz and  $R_\sigma = 0$ , with those for the measured static strength ( $S_s$ ) obtained in Chapter 4. This figure shows that averages and scatters of the equivalent static strengths are fairly close to those of the measured static strengths.

### 5.5.5 Statistical distribution of fatigue data

In addition to the averages and scatters, statistical distributions of the test data for both the measure and the equivalent static strengths must be close to be able to apply the residual strength degradation model for the the statistical analysis.

The statistical distributions can be represented by median ranks (MR) of either the measured or the equivalent static strengths, as follows:

$$MR = \frac{j - 0.3}{i + 0.4} \quad (5.26)$$

where  $i$  is total number of the specimens tested at each temperature, and  $j$  is ranking of the static strengths among the  $i$  specimens.

Figure 5.12 shows the statistical distribution of the measured static-strength data. The static strength was normalized by the characteristic static strength ( $\beta_{si}$ ) in Eq. (5.19). In these figures, solid lines represent the Weibull distribution functions, which were calculated by Eq. (5.5) with the shape and the scale parameters listed in Table 5.2. As in the figure, the test data follow the solid lines fairly well at all temperatures. This agreement indicates that the two-parameter Weibull function can reasonably represent the statistical distribution of the measured static strength.

Figure 5.13 shows the median ranks of the equivalent static strength (solid dots) as well as the measured one (empty dots). At all temperatures, the two strength data follow the Weibull distribution functions fairly well. This agreement indicates that the statistical distribution of the equivalent static strength, which is the initial fatigue strength, is similar to that of the measured static strength. This agreement of the statistical distribution of both strengths enables us to apply the residual strength degradation model to the statistical analysis for the fatigue data of the bonded joint.

Under the assumption that the fatigue strength at  $N = 0$  is close to the static strength in terms of the average, scatter and distribution, it is possible to shift the K-S-N curves of the fatigue strength upwards or downwards by the amount of the scatter of the measured static strength. These shifts explain that the degree of the scatter of the K-S-N curves can be represented by the statistical distribution function of the static strength ( $F_{\mathcal{R}(0)}(x)$ ).

We calculated the statistical distribution function of the fatigue life ( $F_N$ ) by Eq. (5.16), and plotted in solid lines at each stress level in Figure 5.14. We also calculated the median ranks of the fatigue test data by Eq. (5.26), where  $j$  is ranking of the fatigue lives ( $N_f$ ) among the  $i$  specimens at each temperature. In this figure, the experimental data follow the Weibull distribution fairly well at all temperatures. This agreement indicates that the residual strength degradation model can be applied to the statistical analysis for the fatigue behavior of the bonded joint.

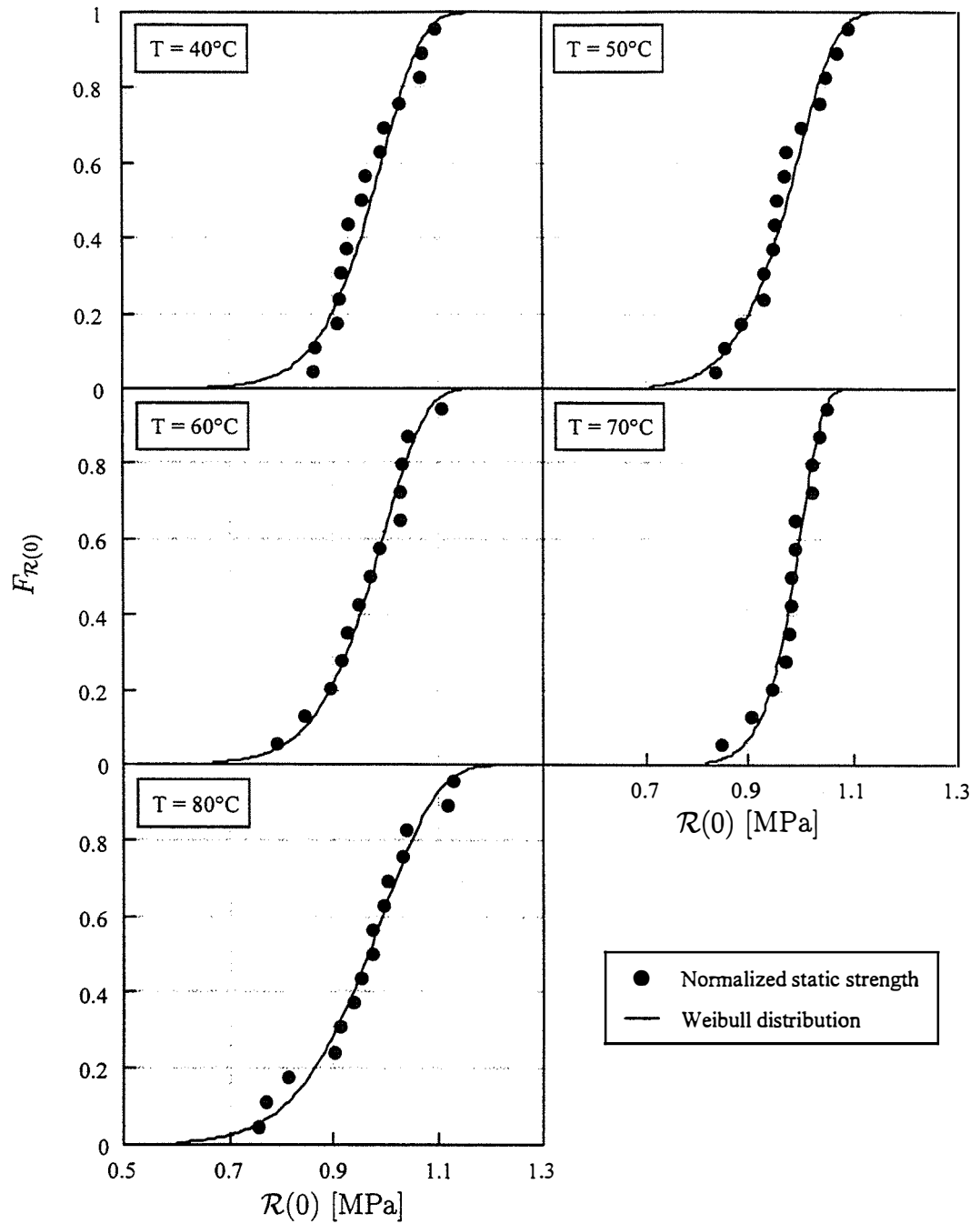


Figure 5.12: Statistical distribution of measured static strength.

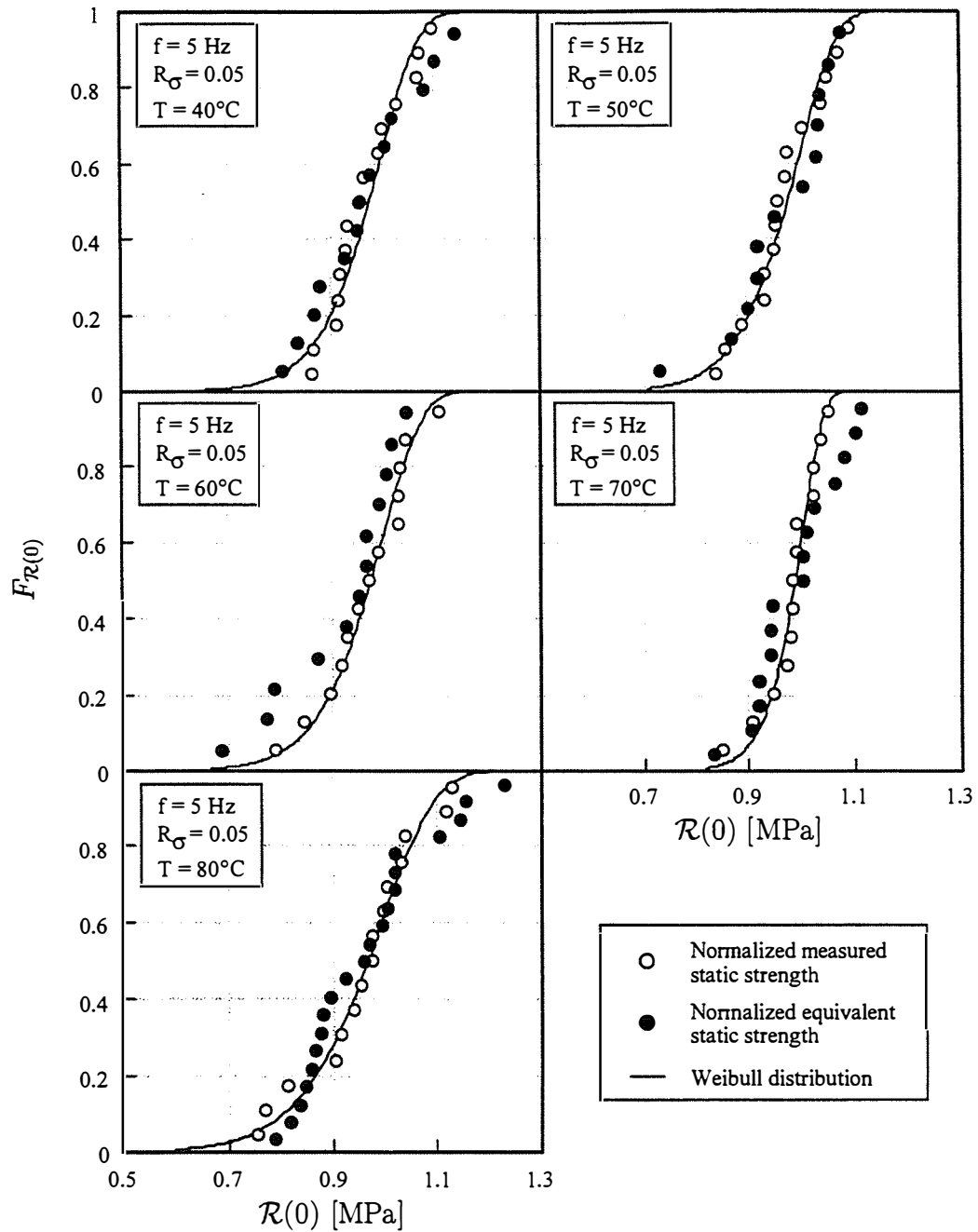


Figure 5.13: Statistical distributions of fatigue life at five temperatures from 40°C to 80°C at  $f = 5$  Hz and  $R_\sigma = 0.05$ .

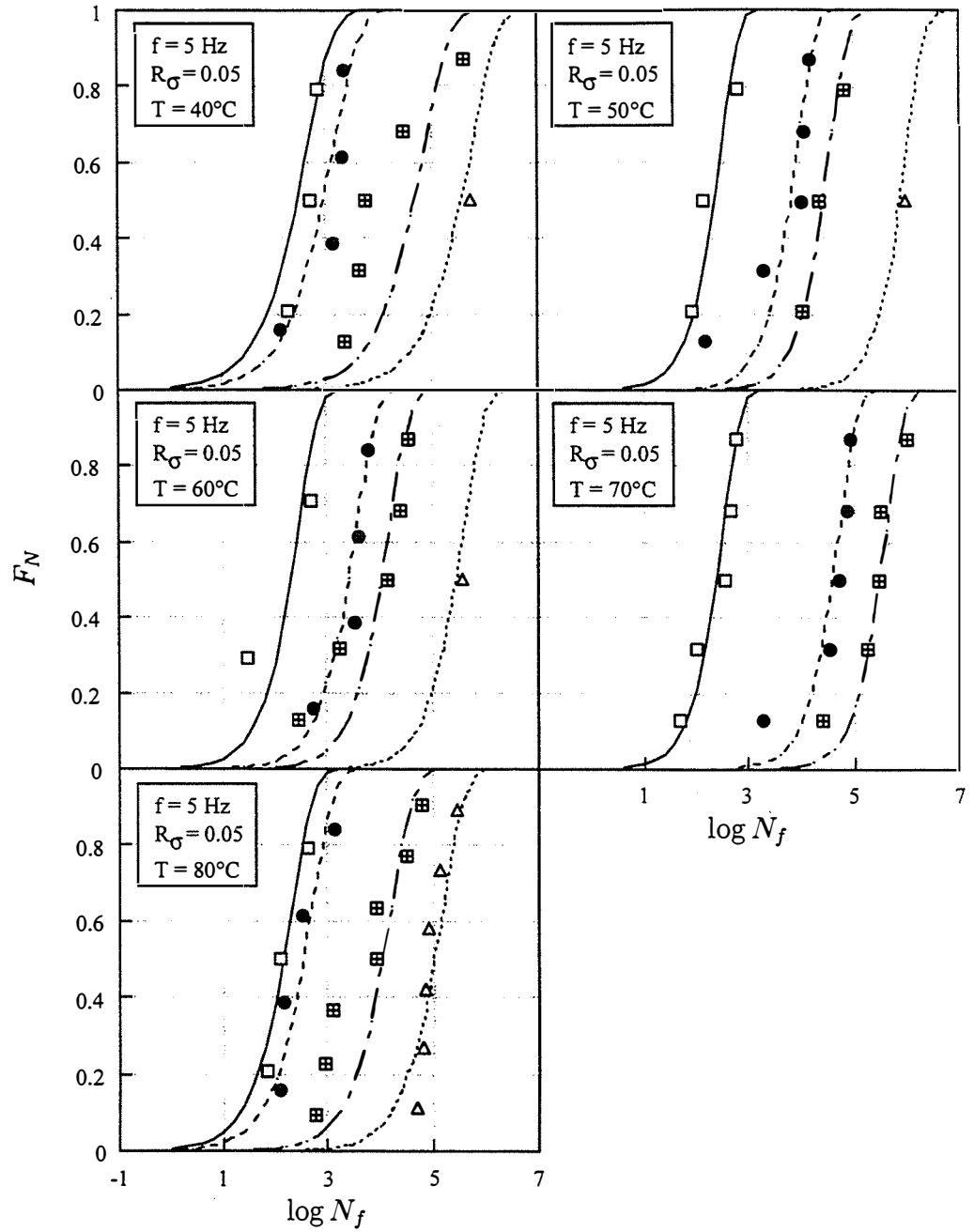


Figure 5.14: Weibull distribution of measured static strength and equivalent static strength calculated from fatigue data at five temperatures from 40°C to 80°C at  $f = 5$  Hz and  $R_\sigma = 0.05$ .



## 5.6 Conclusion

We performed tests under uni-axial tensile-tensile cyclic loadings to measure the fatigue life of the bonded joint. The experiments were performed under various conditions at several temperatures, frequencies and stress ratios.

We observed that the fatigue lives significantly depended on the test conditions, especially over the glass-transition temperature, and the degree of dependency changed when the other conditions changed.

As in the case of the static loading, when the bonding strength at the interface between the cast-iron rod and the adhesive material was weaker than the strength of the adhesive material itself, the bonded joints failed in the brittle type of failure mode. When the strength of the adhesive material got weaker and weaker, the bonded joints were likely to fail in the ductile type of failure mode. Some specimens failed in brittle failure mode at high load levels at low temperatures and high frequencies, but most of the specimens failed in ductile failure mode.

We applied the residual strength degradation model to describe the fatigue behavior of the bonded joint statistically. Using this model, we can estimate the fatigue life (number of cycles to failure) at any load level with a certain probability, and vice versa. Although it was not tried in this study, it is highly recommended that, in future works, the residual strength be measured to verify its validity more carefully.

# Chapter 6

## Life estimation of bonded joints

### 6.1 Problem statement

Life prediction is an essential process in designing a structure, especially when it is operated under long-term fatigue and creep loadings. Several methods have been proposed to predict the long-term fatigue life.

One of the methods is to accelerate the fatigue life by performing tests at a high frequency rather than at an operational frequency. This method is applicable when the structures under the long-term loadings are generally operated at moderately low frequencies. However, this method costs time and equipment because the tests usually go beyond  $10^7$ - $10^8$  cycles. Furthermore, there is a limitation in increasing the frequency. Tests at too high a frequency overheat the test machine as well as the test specimens, and sometimes cause the machine to break down. An even bigger problem of this method is that it results in wide scatters because the tests are usually performed at low stress levels. Consequently, these wide scatters in the test data make the design of the structures almost impossible. Another disadvantage of this method is that a series of additional tests are required to obtain new S-N curves if there are changes in any of the test conditions, such as frequency, stress ratio or temperature.

Another method for the fatigue life prediction is to extrapolate the fatigue data to the long-term range with statistical analyses. Among many statistical analyses, researchers have studied the residual strength degradation model to describe the

fatigue behavior and to predict the fatigue life of the composite laminates [13–18], as explained in Chapter 5. This method enables us to calculate residual strength, which is the strength remaining in an intact test specimen after a certain number of cyclic loadings, and statistical distribution function of the fatigue life. With this method, we can treat the scatter of the fatigue data statistically. This method is suitable for a point design for one set of the loading conditions, but cannot be extended to different conditions without additional series of tests.

The other method is based on the theory of viscoelasticity. Every material shows some viscoelastic behavior whose properties change with loading time and temperature. Schapery [8] had performed many experiments and found that the loading time and the temperature are equivalent for a large class of polymeric materials. This time-temperature equivalence can be used to describe long-term behavior of materials at a certain temperature by performing short-term tests at several elevated temperatures. The life prediction of the materials by time-temperature equivalence was studied by Williams, Landel and Ferry [10] and Miyano and McMurray [9]. Miyano in particular proposed a methodology to predict fatigue and creep lives of viscoelastic material under various conditions without performing additional series of tests. This prediction method has been applied to many polymeric materials, including composite laminates of polymeric resin material and fibers. This method has also been verified by experiments. Considering that the bonded joint shows viscoelastic behavior because of the polymeric adhesive material, we will apply this method in this study.

In this chapter, we will apply the prediction methodology to estimate the fatigue and the creep lives of the bonded joint. One series of static and fatigue tests for generating master curves are used to estimate the lives of the bonded joint subject to a certain loading, or to determine an operational load for designated lives. These master curves are also used to estimate the life of the bonded joint under arbitrary test conditions—frequencies, temperatures and stress ratios—without performing additional series of tests.

## 6.2 Assumptions

The life estimation of the bonded joint using the time-temperature equivalence of the viscoelastic material is based on the following four assumptions:

1. Failure mechanism of the bonded joint does not depend on the type of loadings.
2. Time-temperature equivalence is applicable to the behavior of the bonded joint.
3. Cumulative damage law holds true for the behavior of the bonded joint.
4. Fatigue strengths depend linearly on stress ratio.

The first assumption is that the failure mechanism of the bonded joint does not depend on the loading type, whether it is static or fatigue loading. As studied in Chapters 4 and 5, the bonded joint failed in two types of modes—brittle and ductile. These failure modes were determined by test conditions such as temperature and loading period. No matter what the loading types were, the brittle mode of failure usually appeared at low temperatures and after short periods of loadings when the interfacial failure dominated, and the ductile mode of failure usually appeared at high temperatures and after long periods of loadings when the cohesive failure dominated.

The second assumption is the time-temperature equivalence of the viscoelastic materials is applicable to not only nondestructive but destructive properties of the bonded joint. According to the time-temperature equivalence, long-term behavior at a low temperature is equivalent to short-term behavior at a high temperature, so that the life can be accelerated by elevating the temperature. In Chapters 3 and 4, we have drawn smooth master curves for the creep compliance of the adhesive material and for the static strength of the bonded joint. Furthermore, the time-temperature shift factors of the creep compliance were close to those of the static strength, even though the former is a nondestructive property and the latter is a destructive one. Under this assumption, we can draw the master curve of the static strength of the bonded joint with the time-temperature shift factor of the adhesive material if sufficient static data were not available. By the same token, we can draw a master curve of the fatigue strength of the bonded joint by shifting the K-S-N curves at several elevated temperatures with the time-temperature shift factor of the static strength.

Thirdly, it is assumed that damages on the bonded joint subject to multiple sets of loadings are cumulated to cause total failure regardless of the order of the loadings. This assumption is known as *cumulative damage law* or *Miner's rule*. Under this assumption, creep strength of the bonded joint subject to a constantly applied loading can be related to its static strength subject to the monotonically increased loading.

The last assumption is that the fatigue strengths of the bonded joint depend linearly on stress ratio at the same frequency and temperature. This assumption enable us to avoid additional series of fatigue tests when the test condition of the stress ratio needs to be changed.

The first assumption, regarding the same failure mechanism under the same test conditions, is the most essential one for this life estimation method, and was proven in Chapters 4 and 5. The second assumption about the time-temperature equivalence is also an important one. Applicability of the time-temperature shift factor to the fatigue strength of the bonded joint will be verified later in this chapter. Although the previous work verified the above two fundamental assumptions for many viscoelastic materials, this work will focus on the bonded joint. The last two assumptions regarding the cumulative damage law and the linear dependence of the stress ratio are not fundamental but empirical, and may not be true for the behavior of the bonded joint. With a possible modification of these assumptions, we can still estimate the life under various test conditions as an approximation without performing additional series of tests.

### 6.3 Master curve of fatigue strength at $R_\sigma = 0$

In Figure 5.8, five K-S-N curves were drawn for five temperatures at a high frequency ( $f = 5$  Hz) and a low stress ratio ( $R_\sigma = 0.05$ ) on a log scale. The curves extended backwards so that they started at  $N_f = 1/2$ . Under the conditions of  $R_\sigma = 0.05 \approx 0$ , the fatigue strengths at these starting points can approximate the static strengths at the temperature, as explained in Chapter 5. The curves can be replotted on the time scale ( $t_f = N_f/f$ ) on the left-hand side of Figure 6.1.

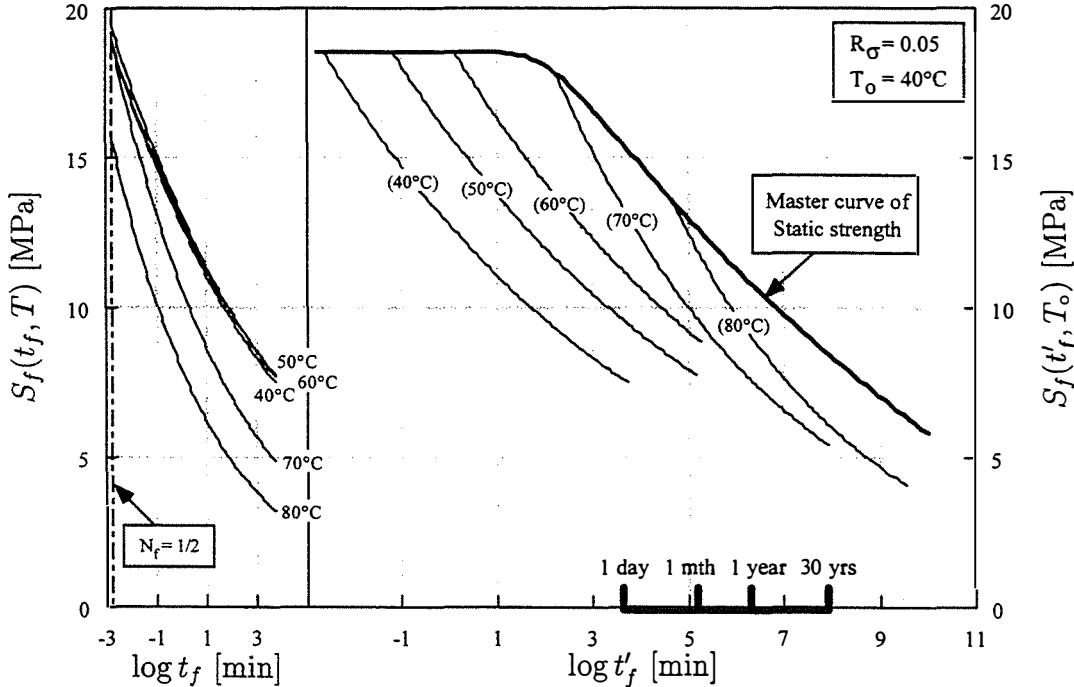


Figure 6.1: Fatigue strengths of bonded joint on original and shifted time scale at five temperatures at a high frequency ( $f = 5$  Hz) and a low stress ratio ( $R_\sigma = 0.05$ ).

Under the first and second assumptions, the time-temperature equivalence is applied to the fatigue strength of the bonded joint, because the curves on the logged time scale at elevated temperatures can be shifted with the time-temperature shift factor of the static strength. We set a reference temperature ( $T_o$ ) to 40°C, and shifted the curves at higher temperatures horizontally onto a shifted time scale ( $t'_f$ ), which can be calculated by

$$t'_f = \frac{t_f}{a_{T_o}(T)} = \frac{N_f/f}{a_{T_o}(T)} \quad (6.1)$$

where  $t_f$  is the original time to failure and  $a_{T_o}$  is the time-temperature shift factor of the static strength of the bonded joint, which varies with the temperature. The shifted curves are shown on the right-hand side of Figure 6.1. Because the starting points correspond to the static strengths, these points lie on the master curve of static strength that was drawn in Figure 4.8.

In Figure 6.2, the fatigue test data are plotted with the shifted curves. Empty dots and solid dots indicate the brittle failure and the ductile failure, respectively. The figure shows that brittle failure and ductile failure distinctively appear under short and long periods of loadings, respectively. The first assumption in Section 6.2 can be backed up by this distinct appearance of two failure modes under both the static and the fatigue loadings.

On each shifted curve, we can pick several points for  $N_f = 10^1, 10^2, \dots$ . We can draw master curves of fatigue strength by connecting these points of the same number of cycles to failure on all shifted curves, as Figure 6.3 shows. These master curves are only valid for  $R_\sigma = 0$ . We can draw the master curves for any number of cycles to failure ( $N_f$ ) by this method.

Using the master curves, we can estimate the fatigue lives ( $N_f$  or  $t'_f$ ) for any load levels at zero stress ratio ( $S_{f:0}$ ) at the reference temperature, and vice versa. Because we can set the reference temperature to any temperature, we can perform this estimation for any temperature. Furthermore, because  $N_f$  and  $t'_f$  are related to the frequency ( $f$ ) as in Eq. (6.1), the estimation can be done for any frequencies if either of  $N_f$  or  $t'_f$  is a given variable of a design.

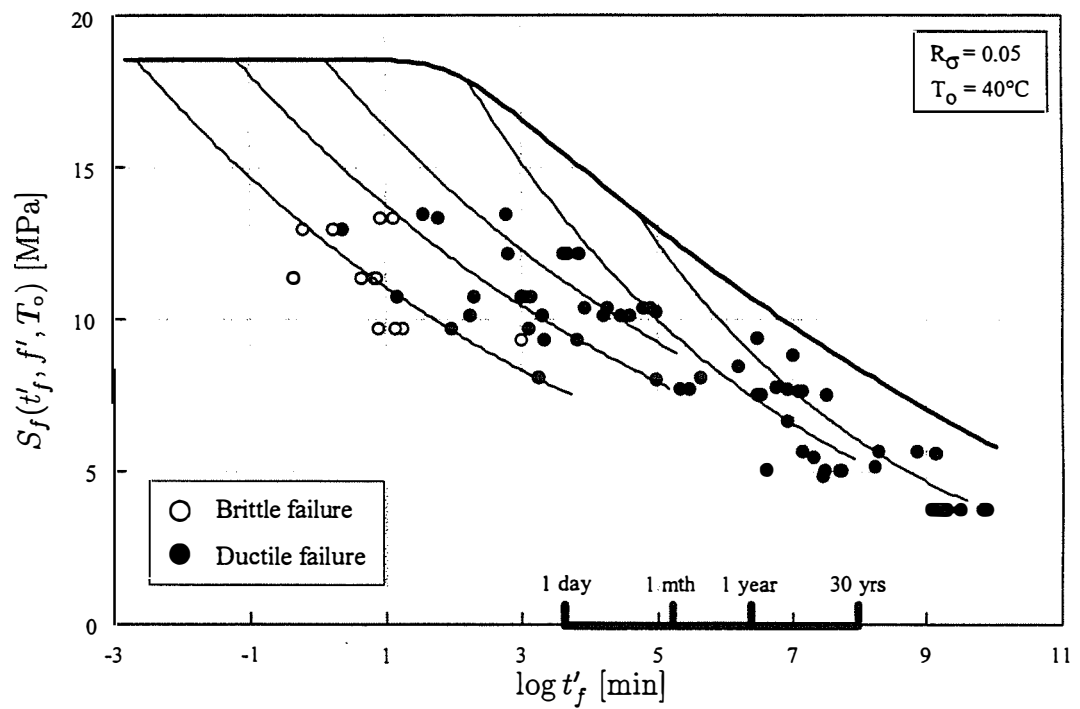


Figure 6.2: Test data of fatigue strengths of bonded joint on shifted time scale at five temperatures at a high frequency ( $f = 5$  Hz) and a low stress ratio ( $R_\sigma = 0.05$ ).



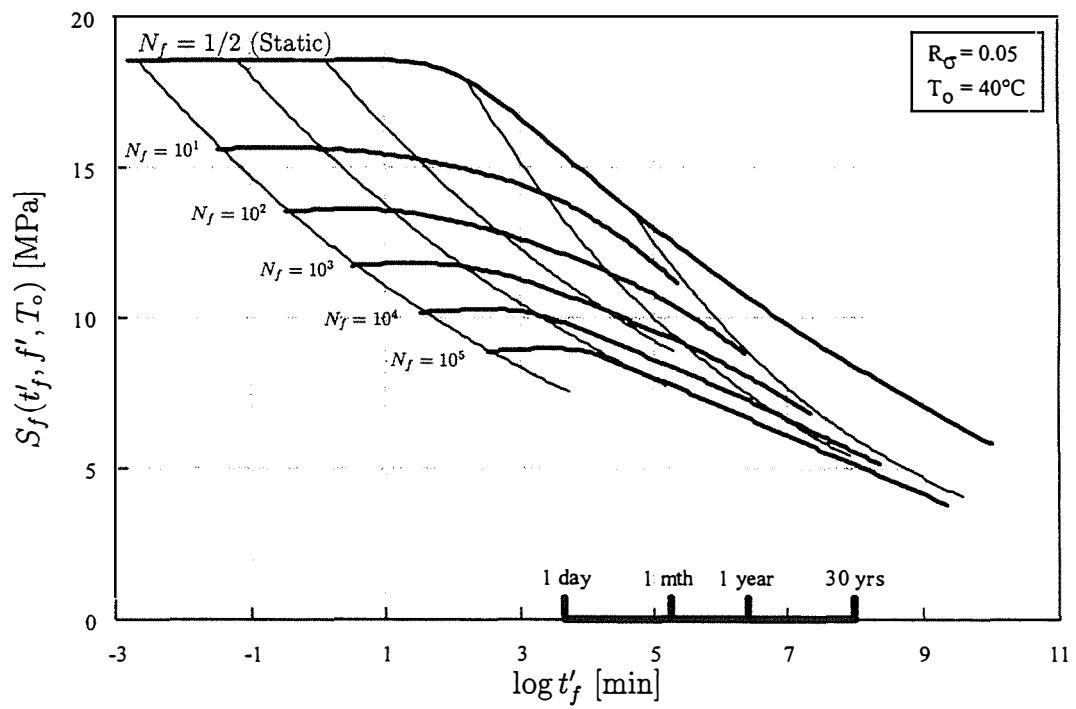


Figure 6.3: Master curve of fatigue strength at  $R_\sigma = 0.05(\approx 0)$  at a reference temperature ( $T_0 = 40^\circ\text{C}$ ).

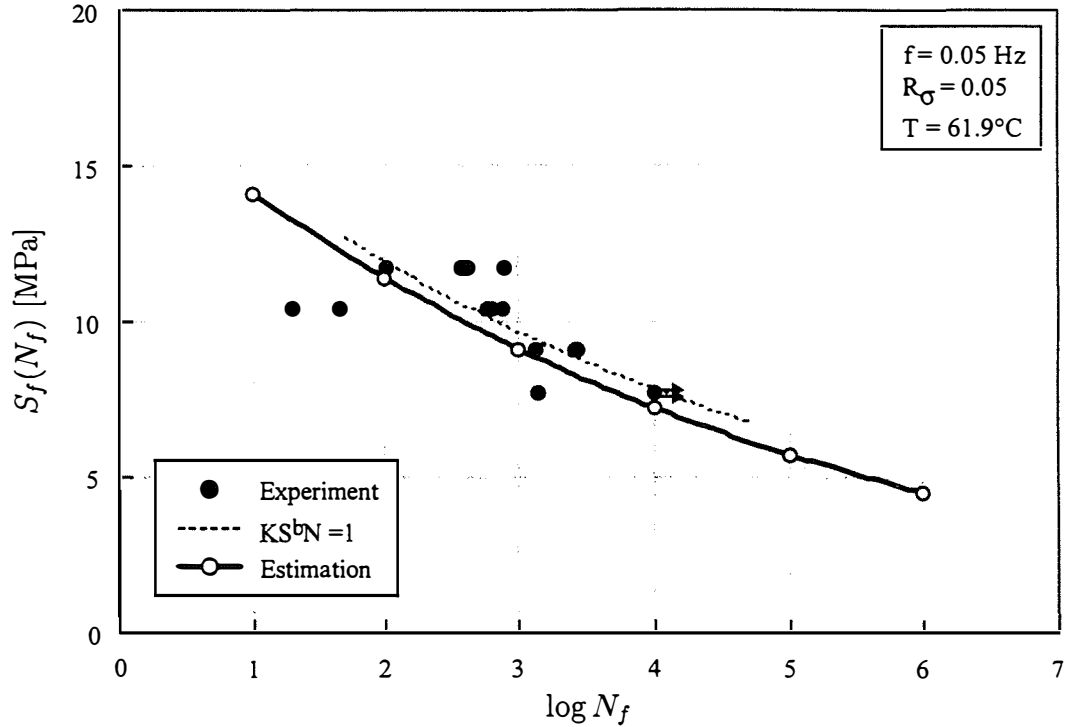


Figure 6.4: Comparison of estimated and experimental K-S-N curves: The estimated curve is drawn from master curve of fatigue strength at zero stress ratio in Figure 6.3.

As an example, we estimated the fatigue life at zero stress ratio at a low frequency ( $f = 0.05$  Hz) and at  $T = 61.9^\circ\text{C}$ . This estimation is compared with the experimental data of Series IV in Table 5.1 as follows: For each line for  $N_f = 10^1, 10^2, \dots, 10^5$ , we can calculate the shifted time to fatigue failure ( $t'_f$ ) by plugging  $f = 0.05$  Hz and  $T = 61.9^\circ\text{C}$  into Eq. (6.1). In this equation, the time-temperature shift factor at this temperature can be obtained by interpolating the lines in Figure 3.7, which is

$$\log a_{T_o}(61.9^\circ\text{C}) = -2.88 \quad (6.2)$$

By reading the values for  $S_{f:0}$  and  $t'_f$  on the master curves, we can draw an estimated S-N curve as in Figure 6.4.

The test data and the K-S-N curves in Series IV were drawn with dots and a dotted line, whereas the estimated S-N curve was drawn with a solid line. The figure shows that the estimated S-N curve is close in magnitude and shape to the experimental one. This agreement indicates that the master curves, drawn by shifting the original curves with the time-temperature shift factors of the static strength, can be used to estimate the fatigue life or fatigue strength at zero stress ratio at any temperatures and frequencies.

Because the master curves were drawn by shifting the original curves with the time-temperature shift factors of the static strength, we can conclude that the time-temperature equivalence is applicable to the destructive property of the bonded joint under both the static and fatigue loading conditions, which backs up the second assumption.

In Figure 6.3, the master curves were drawn to a time range of  $t'_f = 10^9$  [min]. This range corresponds to a few decades. It is almost impossible to estimate the fatigue life up to this time range without using these master curves, as explained in Section 6.1. Therefore, the master curves can be used to estimate the fatigue life not only under various loading conditions but under long-term periods of loadings.

## 6.4 Cumulative damage law

Material often fails under a constant magnitude of *creep* load even though the load is lower than the failure strength of the material. The creep failure usually occurs under long-term period loadings, so the structure design must consider this creep failure as well as the long-term fatigue failure. Because this long-term creep failure is caused by the time dependence of the viscoelastic materials, we can apply the time-temperature equivalence to accelerate the creep life by elevating the temperature. This can be done by drawing a master curve of creep strength at the reference temperature extended to a long-term period.

Under the third assumption about the cumulative damage law, we can draw the master curve of creep strength from the master curve of static strength obtained in Section 4.3.4. On the master curve of static strength, the  $x$ -axis represents the

(shifted) time to failure under the monotonically increased static loadings. This static loading can be approximated as multiple steps of constant amplitude loadings, as shown in Figure 6.5(a). In the figure, we can divide the static failure load ( $S_s$ ) into  $(2n)$  steps so that the time to static failure ( $t_s$ ) is equal to a sum of  $n$  time steps ( $\Delta t^{(i)}$  for  $i = 1, 3, \dots, 2n - 1$ ). Then the monotonically increased static loading at a load level of  $\sigma_{i+1}$  can be approximated as a sum of constant amplitude of creep loads up to  $\sigma_i$ . For example, a static load at  $\sigma_2$  is approximated as a creep load ( $\sigma_1$  during time  $\Delta t^{(1)}$ ), and a static load at  $\sigma_4$  is approximated as a sum of two creep loads ( $\sigma_1$  during  $\Delta t^{(1)}$  and  $\sigma_3$  during  $\Delta t^{(3)}$ ).

Meanwhile, time to creep failure at a load level of  $\sigma_i$  is denoted by  $t_c^{(i)}$ , as Figure 6.5(b) shows. Because total failure at a load level of  $\sigma_i$  occurs at  $t_c^{(i)}$ , damage ( $DM^{(i)}$ ) occurring at this load level during the time step ( $\Delta t^{(i)}$ ) can be calculated as

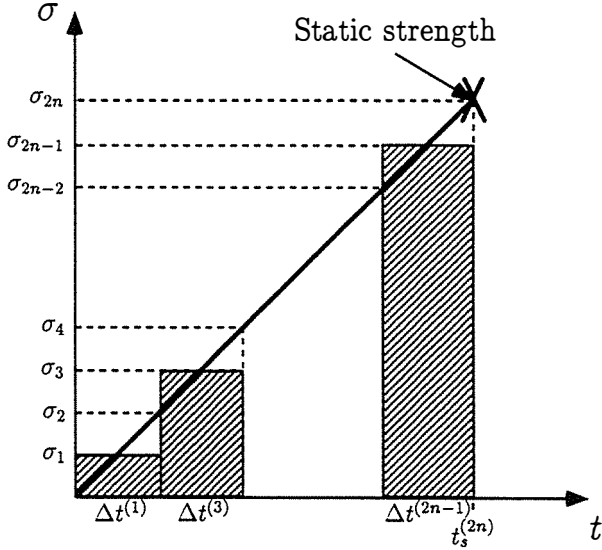
$$DM^{(i)} = \frac{\Delta t^{(i)}}{t_c^{(i)}} \quad (6.3)$$

According to the linear cumulative damage law, damages are cumulated by applied loadings so that total damage during the several loadings can be approximated as a sum of damage caused by each loading. As shown in Figure 6.5(a), the total damage (DM) caused by static failure during  $t_s^{(2n)}$  is then considered as a sum of the damages during each time step, which leads to

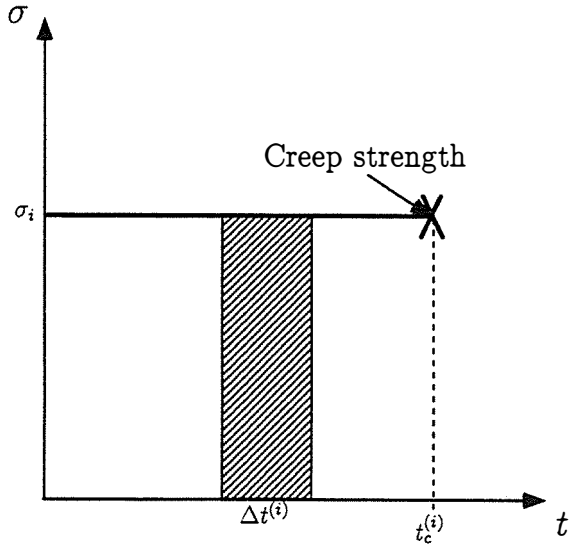
$$DM = \sum_{i=1}^n DM^{(2i-1)} = \sum_{i=1}^n \frac{\Delta t^{(2i-1)}}{t_c^{(2i-1)}} \quad (6.4)$$

Suppose that the failure occurs when DM reaches one, a failure condition becomes

$$DM = \frac{\Delta t^{(1)}}{t_c^{(1)}} + \frac{\Delta t^{(3)}}{t_c^{(3)}} + \dots + \frac{\Delta t^{(2n-1)}}{t_c^{(2n-1)}} = 1 \quad (6.5)$$



(a) Static strength



(b) Creep strength

Figure 6.5: Linear cumulative damage law for a linearly increased static load.

**Linearly increased static load case**

If the static load increased linearly until the failure, which was mostly observed in brittle mode of failure, the time steps become equally spaced so that

$$\Delta t^{(1)} = \Delta t^{(3)} = \dots = \Delta t^{(2n-1)} = \frac{t_s^{(2n)}}{n} \quad (6.6)$$

Then Eq. (6.5) becomes

$$\frac{t_s^{(2n)}}{n} \left[ \frac{1}{t_c^{(1)}} + \frac{1}{t_c^{(3)}} + \dots + \frac{1}{t_c^{(2n-3)}} + \frac{1}{t_c^{(2n-1)}} \right] = 1 \quad (6.7)$$

By multiplying and dividing by  $(n-1)/t_s^{(2n-2)}$ ,

$$\frac{t_s^{(2n)}}{n} \left[ \frac{n-1}{t_s^{(2n-2)}} \cdot \frac{t_s^{(2n-2)}}{n-1} \left\{ \frac{1}{t_c^{(1)}} + \frac{1}{t_c^{(3)}} + \dots + \frac{1}{t_c^{(2n-3)}} \right\} + \frac{1}{t_c^{(2n-1)}} \right] = 1 \quad (6.8)$$

If we replace  $n$  with  $(n-1)$ , Eq. (6.7) becomes

$$\frac{t_s^{(2n-2)}}{n-1} \left[ \frac{1}{t_c^{(1)}} + \frac{1}{t_c^{(3)}} + \dots + \frac{1}{t_c^{(2n-3)}} \right] = 1 \quad (6.9)$$

Then Eq. (6.8) becomes

$$\frac{t_s^{(2n)}}{n} \left[ \frac{n-1}{t_s^{(2n-2)}} + \frac{1}{t_c^{(2n-1)}} \right] = 1 \quad (6.10)$$

And, finally,

$$t_c^{(2n-1)} = \frac{t_s^{(2n)} t_s^{(2n-2)}}{n t_s^{(2n-2)} - (n-1) t_s^{(2n)}} \quad (6.11)$$

Because we approximate the time to static failure at load level of  $\sigma_2$  as time to creep failure at  $\sigma_1$ , we can calculate the time to creep failure at any load level by the recursive formula, Eq. (6.10), as follows:

$$t_c^{(1)} = t_s^{(2)} \quad (6.12)$$

$$t_c^{(2n-1)} = \frac{t_s^{(2n)} t_s^{(2n-2)}}{n t_s^{(2n-2)} - (n-1) t_s^{(2n)}} \quad \text{for } n \geq 2 \quad (6.13)$$

### Nonlinearly increased static load case

If the static load increased nonlinearly until failure, which was mostly observed in ductile mode of failure, it is necessary to correct the load level for the time step ( $\Delta t^{(i)}$ ). As shown in Figure 6.6(a), the load level ( $\sigma_i$ ) evaluated on the linear curve underestimates the actual load level ( $\sigma_i^*$ ) on the nonlinear curve. This difference becomes bigger if the nonlinearity becomes higher, resulting from the high viscoelasticity appearing such at high temperatures. Such a big difference may cause error in the estimation. A ratio of two load levels can be calculated by areas formed by  $\Delta t^{(i)}$ , such as

$$\frac{\sigma_i^*}{\sigma_i} = \frac{\Delta A^*}{\Delta A} \quad (6.14)$$

Assuming that this ratio is preserved during the static loading until the failure, the load levels for the nonlinear loading can be modified such as

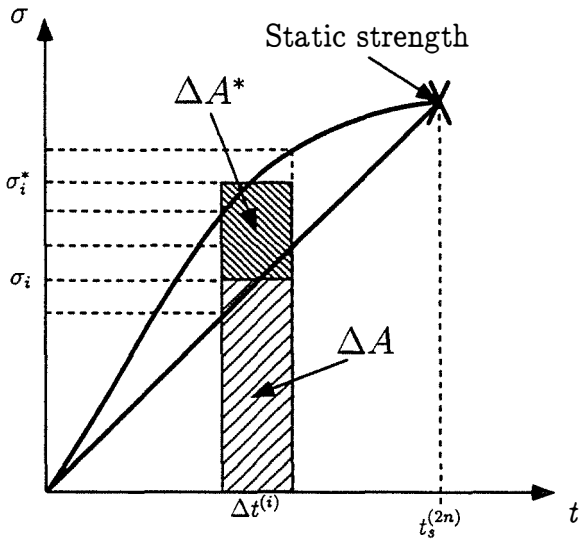
$$\begin{aligned} \sigma_i^* &= \frac{A^*}{A} \sigma_i \\ &= \frac{A^*}{S_s t_s / 2} \sigma_i \end{aligned} \quad (6.15)$$

where  $A^*$  is the area occupied by the nonlinear load-displacement curve with an interval from 0 to  $t_s$ , as Figure 6.6(b) shows.

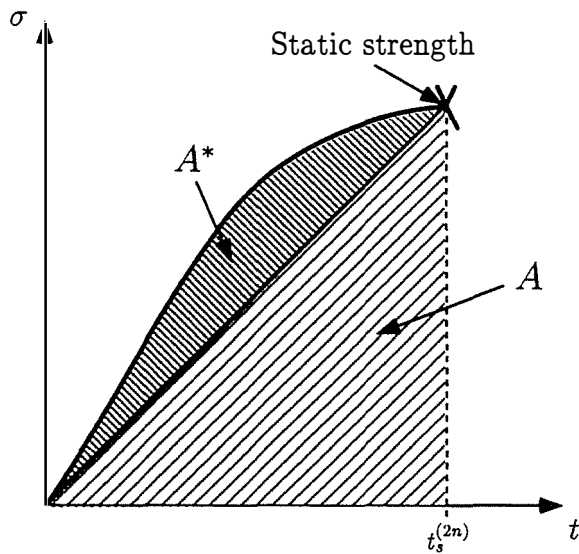
## 6.5 Master curve of creep strength

We can draw the master curve of creep strength by calculating the time to creep failure ( $t_c$ ) at any load level by Eq. (6.13), when the time to static failure ( $t_s$ ) at the load level is taken from the master curve of static strength. Figure 6.7 shows these master curves of creep and static strengths at the reference temperature ( $T_o = 40^\circ\text{C}$ ).

The dashed-dotted line represents the master curve of static strength, whereas



(a)



(b)

Figure 6.6: Modification of linear cumulative damage law for a nonlinearly increased static load.



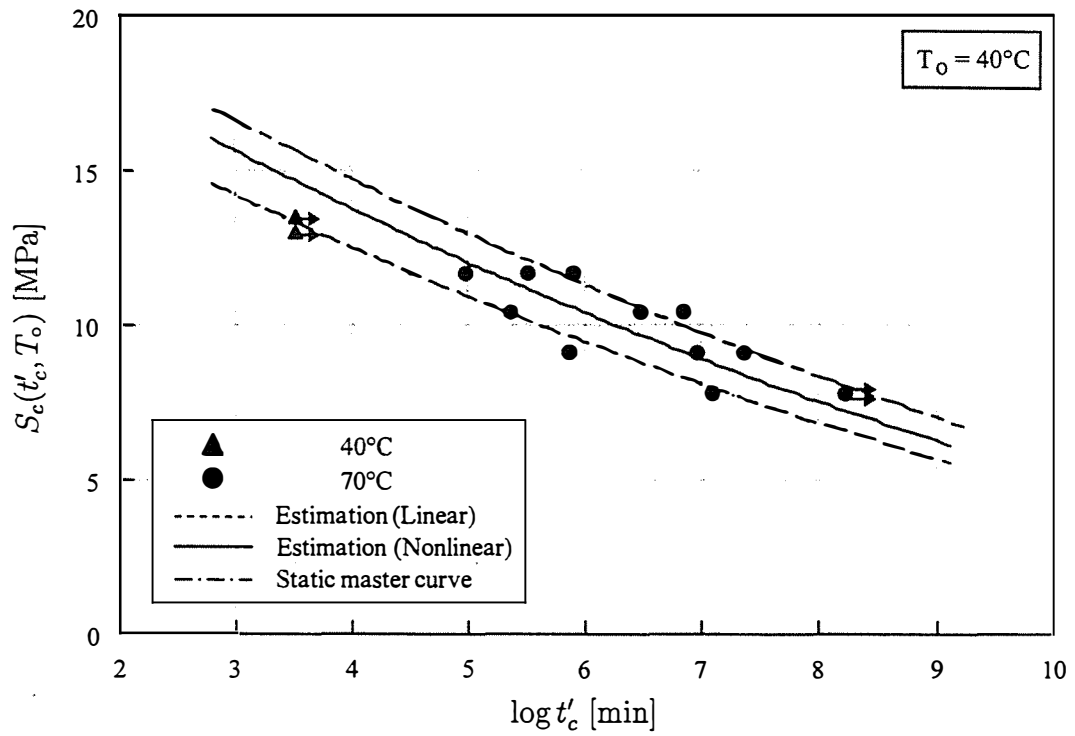


Figure 6.7: Master curve of creep strength at a reference temperature ( $T_o = 40^\circ\text{C}$ ). This master curve is estimated from master curve of static strength by cumulative damage law. A modification in the cumulative damage law makes better agreement with the experimental data at  $70^\circ\text{C}$ .

the dotted and the solid lines represent the master curves of creep strength in the case of linear and nonlinear static loads, respectively. The fatigue data in Series III ( $R_\sigma = 0.95 \approx 1$ , which approximates the creep loading) that were tested at two temperatures (40°C and 70°C) are plotted in the same figure by shifting them with the time-temperature shift factors of the static strength. The two data points for 40°C lie well on the dotted curve, whereas the data points for 70°C follow the solid line fairly well.

The above leads onto the conclusion that the cumulative damage law and the time-temperature equivalence are applicable to the creep behavior of the bonded joint, and that we need to modify the time to creep failure for better estimation in the case of the nonlinear static loadings. Because the creep test is a time-consuming and expensive process, it is an advantage to have such an estimation only by performing the static tests. Furthermore, because we can draw the master curve of creep strength to a time range of  $t'_c = 10^9$  [min] as in the static and fatigue cases, it is possible to estimate the creep life subject to long-term periods of loadings.

## 6.6 Dependence on stress ratio

Figure 5.10 showed that the fatigue behavior of the bonded joint depended on the stress ratio because of the degree of fluctuation, and that the degree of dependency changed with the temperature. Previous work [9] suggested a method to obtain an approximate estimate of the fatigue strength at arbitrary stress ratios by using the master curve of the fatigue strength at zero stress ratio and the master curve of creep strength, obtained in Sections 6.3 and 6.5, respectively. This method is based on the fourth assumption that the fatigue strengths of the bonded joint depend linearly on the stress ratio if the other conditions (such as frequency and temperature) are fixed. Because the creep strength is the same as the fatigue strength at  $R_\sigma = 1$ , we can write this linear dependence as follows:

$$\begin{aligned} S_f(t_f; R_\sigma, f, T) &= S_f(t_f; 1, f, T) \cdot R_\sigma + S_f(t_f; 0, f, T) \cdot (1 - R_\sigma) \\ &= S_c(t_f; T) \cdot R_\sigma + S_{f,0}(t_f; f, T) \cdot (1 - R_\sigma) \end{aligned} \quad (6.16)$$

where  $S_f$ ,  $S_c$  and  $S_{f:0}$  are the fatigue strengths at arbitrary conditions, the creep strength and the fatigue strength at zero stress ratio, respectively. By the time-temperature equivalence, we can replace  $S_c(t_f; T)$  and  $S_{f:0}(t_f; f, T)$  with the ones at the reference temperature,  $S_c(t'_f; T_o)$  and  $S_{f:0}(t'_f; f', T_o)$ , respectively, such that

$$S_f(t_f; R_\sigma, f, T) = S_c(t'_f; T_o) \cdot R_\sigma + S_{f:0}(t'_f; f', T_o) \cdot (1 - R_\sigma) \quad (6.17)$$

where the shifted time-to-fatigue failure ( $t'_f$ ) and the shifted frequency ( $f'$ ) are calculated by

$$f' = a_{T_o}(T) f \quad (6.18)$$

$$t'_f = \frac{t_f}{a_{T_o}(T)} \quad (6.19)$$

When the stress ratio is equal to zero, the first term in Eq. (6.17) diminishes to leave the fatigue strength at zero stress ratio. When the stress ratio is equal to one, the second term diminishes to leave the creep strength. This equation enables us to approximately estimate the fatigue strength at any loading periods, stress ratios, frequencies and temperatures without performing additional tests.

Figure 6.8 shows estimated S-N curves drawn by Eq. (6.17) at  $R_\sigma = 0.5$  for two temperatures of 40°C and 70°C. For comparison, the experimental data and the corresponding K-S-N curves in Series II are also plotted in the figure with dots and dotted lines, respectively. At 40°C, the test data follow the estimated curve fairly well. However, because, at 70°C, the experimental K-S-N curve at  $R_\sigma = 0.5$  is close to that at  $R_\sigma = 0.95$ , the experimental data fail to follow the estimated curve. Because of this disagreement, the fourth assumption cannot be made for the fatigue behavior of the bonded joint. We need additional fatigue tests at intermediate stress ratios to determine the dependence of the stress ratio more accurately.

However, we can observe that the experimental data are scattered and are not plotted far from the estimated curve, and that the error caused by the scatter of the data is bigger than that of the estimation. Furthermore, the estimated curves underestimate the fatigue strength or the fatigue life, which is on the conservative side

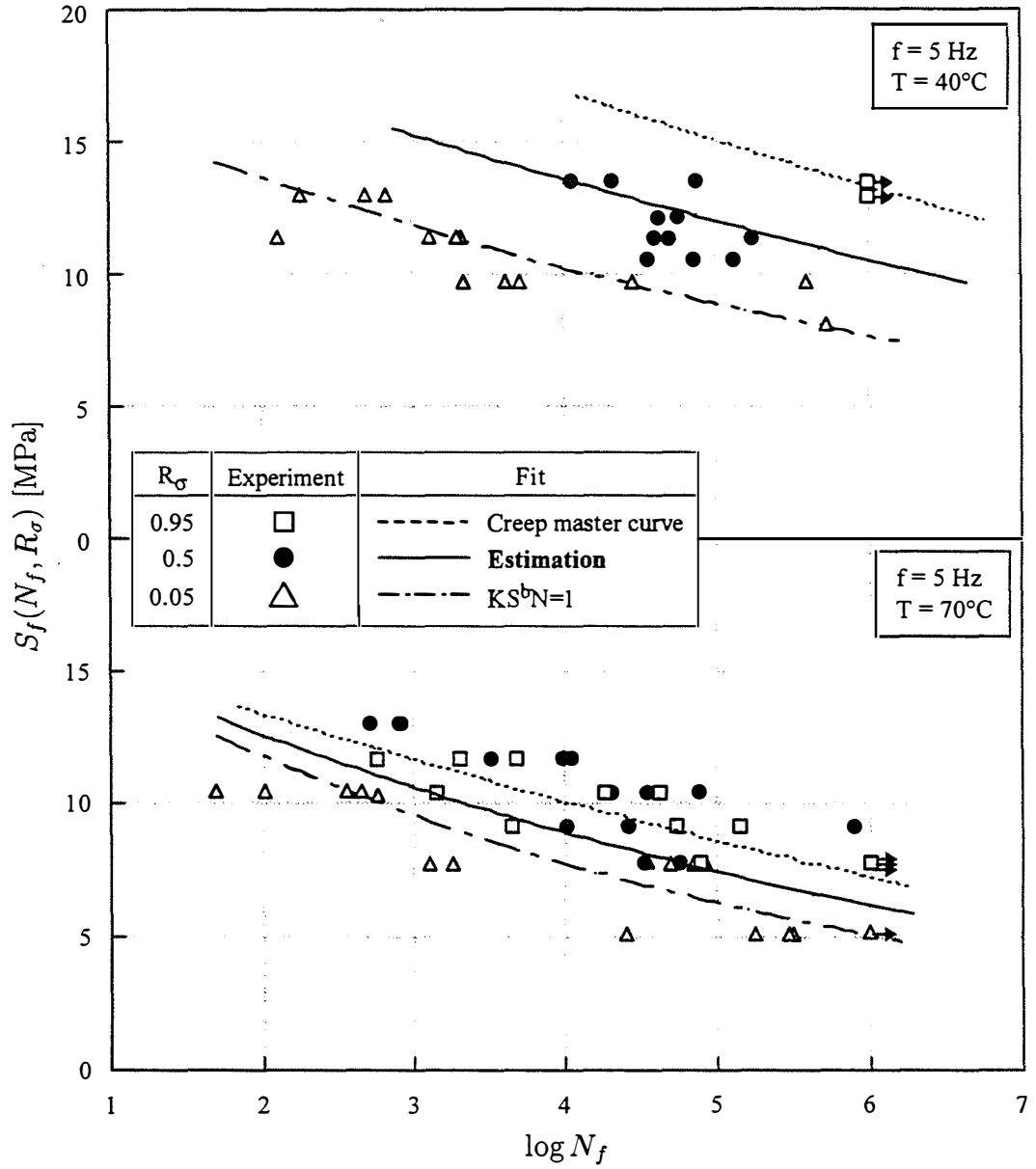


Figure 6.8: Estimated S-N curves drawn by Eq. (6.17) at  $R_\sigma = 0.5$  for two temperatures,  $T = 40^\circ\text{C}$  and  $70^\circ\text{C}$ .

for design. For these reasons, Eq. (6.17) can be used for an approximate estimation of the fatigue behavior of the bonded joint under long-term periods of loading conditions.

## 6.7 Summary

Figure 6.9 shows how to estimate the fatigue and creep lives of the bonded joint. The first step was to perform static tests to measure static strengths at several temperatures and loading rates. With these test data, we drew the master curve of static strength at a reference temperature by applying the time-temperature equivalence. During this step, we calculated time-temperature shift factors of the static strength for the several temperatures at the reference temperature.

Meanwhile, we performed fatigue tests at zero stress ratio at several temperatures and frequencies to measure the fatigue lives at several load levels. Under the first and second assumptions, we applied the time-temperature shift factors of the static strength to the fatigue data to draw the master curve of fatigue strength at zero stress ratio at the reference temperature.

Under the third assumption about the cumulative damage law, we drew the master curve of creep strength by the the master curve of the static strength and Eq. (6.13). Because the creep strength is considered equivalent to fatigue strength at unit stress ratio, we had drawn two master curves of fatigue strength at two stress ratios,  $R_\sigma = 0$  and  $R_\sigma = 1$ .

Finally, under the fourth assumption with Eq. (6.17), we drew the estimated S-N curves at any stress ratios as a first-order of approximation. Because we calculated the time-temperature shift factors at any temperature, we can draw the estimated S-N curves at any temperature, frequency and stress ratio by changing the reference temperature.

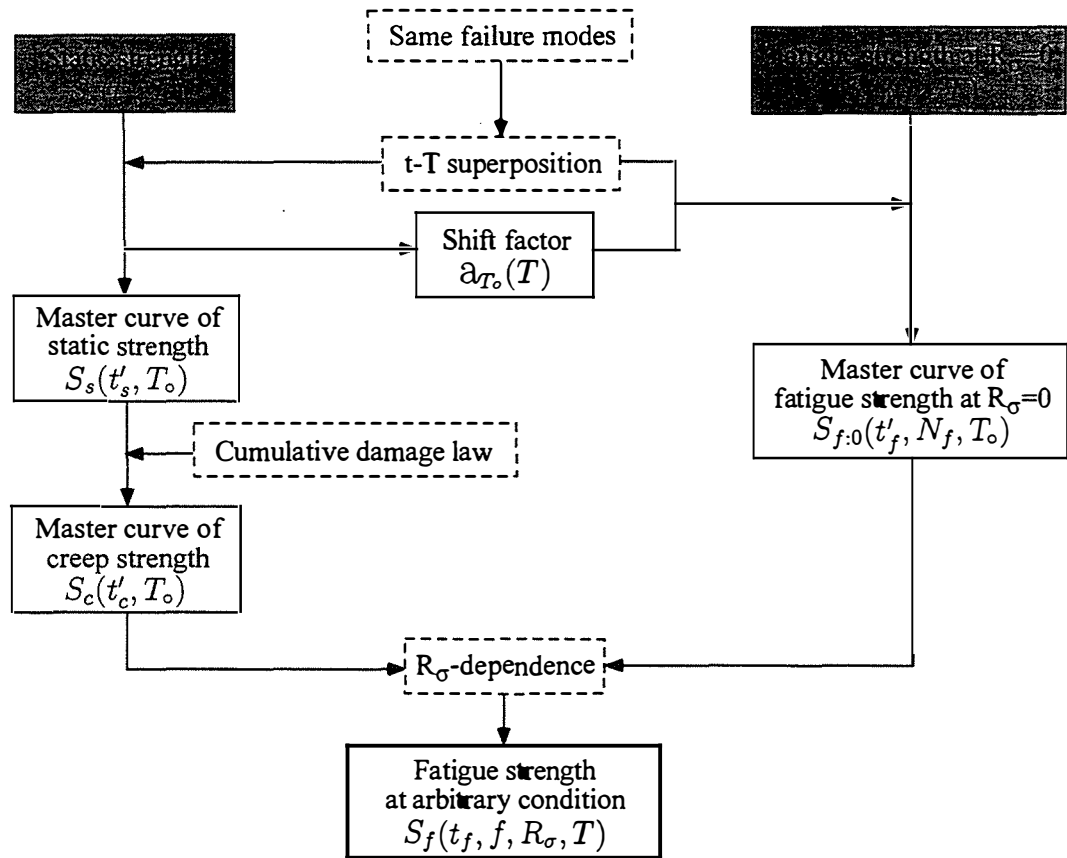


Figure 6.9: Flow chart for the fatigue life estimation method of bonded joints.

## 6.8 Conclusion

In this chapter, we applied a life estimation method, which was previously proposed to apply to the viscoelastic materials, to estimate the fatigue and the creep lives of the bonded-jointed structures. For this method, we needed to make four assumptions. We observed that the same failure mode appeared at the same test conditions regardless of the loadings types—static, creep or fatigue loadings. The time-temperature equivalence was applicable to describe the behavior of the bonded joint because it is significantly affected by the viscoelastic adhesive material.

We also found that the cumulative damage law is applicable to the bonded joint to calculate the time to creep failure. However, we needed to modify the cumulative damage law for better estimation in the case of the nonlinearly increased static loads under highly viscoelastic conditions, such as at high temperatures and low strain-rates.

Even though we failed to prove the linear dependence of the stress ratio on the fatigue strength of the bonded joint, this method is still worth trying to estimate the fatigue behavior of the bonded joint quickly and simply without performing additional tests.

This life estimation method requires us to draw three master curves of static strength, creep strength and fatigue strength at zero stress ratio. We were able to draw long-term ranges of the smooth master curves by shifting the test data performed during the short-term periods. We can then use these master curves for life estimation at arbitrary conditions such as various temperatures, frequencies and stress ratios as a first-order approximation without performing further expensive, time-consuming tests.

# Chapter 7

## Examples

### 7.1 Problem statement

This chapter explains how to apply the life estimation method to a structural design. In Chapter 6, we provided a methodology to estimate life of a structure under a cyclic loading condition by drawing the master curves of static, creep and fatigue strength. When the structure is operated under noncyclic arbitrary loadings, we can still use the master curves by using a *cycle counting method*.

### 7.2 Rainflow cycle counting

The cycle counting [19,20] is a methodology to transform an irregular load history into artificially derived regular cycles. An assumption made on this method is that the regular cycles (artificially defined) do the same amount of fatigue damage as the irregular load history. There are several cycle counting methods, such as *level-crossing counting*, *peak counting*, *simple-range counting* and *rainflow counting*.

For the cycle counting, we need to establish a block of load that repeats in the irregular load history as in Figure 7.1. The load block is a sequence of several peaks and valleys. With this load block, procedure for the rainflow cycle counting method is as follows:



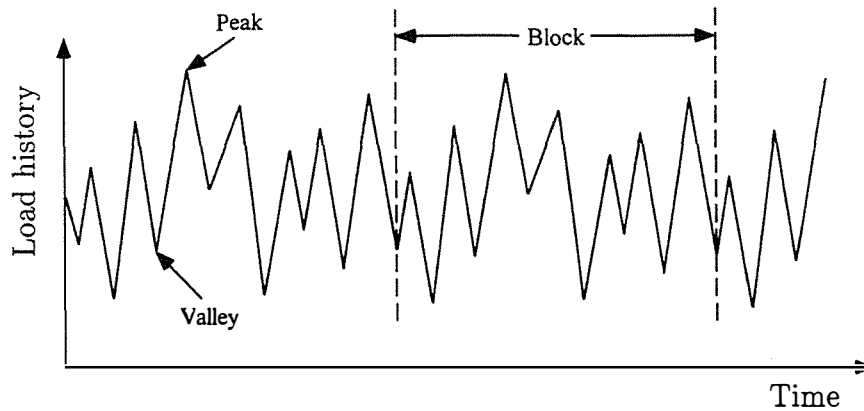


Figure 7.1: An irregular load history.

1. start imaginary water drop with sight at each peak and valley in succession (not simultaneously).
2. track the flow of a given drop. The flow will stop if the drop sees
  - a peak higher than the one from which it starts if it started at a peak, or
  - a valley deeper than the one from which it starts if it started at a valley.
3. flow will stop to avoid colliding with a previously established flow.
4. place the largest magnitude of load first in the block and rearrange other loads in the blocks.
5. leave a few large cycles by filtering out small rainflow cycles.

Suppose we establish a load block as in Figure 7.2(a). Points **a**, **c**, **e** and **g** are peaks, whereas points **b**, **d** and **f** are valleys. The peak **a** has the same magnitude as the peak **g** since the load block will repeat at the point **g**.

Figure 7.2(b) shows how the raindrops flow and stop by following the above procedure. A raindrop starting at a peak **a** will flow downward through points **b** and **d**. Another raindrop starting at the point **d** will flow to the point **g**. These two rainflows form a cycle ( $\mathbf{a} \rightarrow \mathbf{d} \rightarrow (\mathbf{g} = \mathbf{a})$ ).

A raindrop starting at a valley  $\mathbf{b}$  will flow downward through a point  $\mathbf{c}$ , and stop immediately since the drop sees a valley  $\mathbf{d}$  which is deeper than the starting valley  $\mathbf{b}$ . Meanwhile, a raindrop starting at a peak  $\mathbf{c}$  will flow downward and stop immediately at a point  $\mathbf{c}'$  to avoid colliding with the flow starting from the point  $\mathbf{a}$ . These two rainflows form another cycle ( $\mathbf{b} \rightarrow \mathbf{c} \rightarrow (\mathbf{c}' = \mathbf{b})$ ). By a similar way, rainflows starting from a peak  $\mathbf{e}$  and a valley  $\mathbf{f}$  will form another cycle ( $\mathbf{e} \rightarrow \mathbf{f} \rightarrow (\mathbf{f}' = \mathbf{e})$ ).

The rainflow-counted cycles with the peaks and valleys are rearranged by their magnitudes in Figure 7.2(c). After filtering out small cycles (e.g., the third cycle), we can calculate significant damages subject to each cyclic loading using the master curve of fatigue strength. We can then calculate total damage during the load block by linear cumulative damage law (Miner's rule).

A numerical calculation helps to do the rainflow cycle counting for more complex load blocks. Appendix B lists a numerical program running on MATLAB software to calculate magnitudes of peaks and valleys for each cycle.

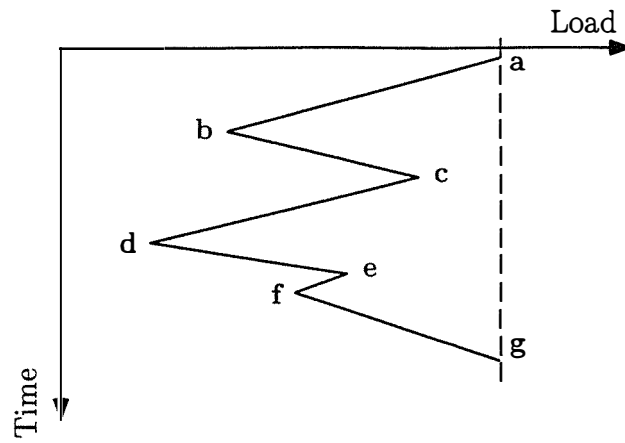
### 7.3 A numerical example

Suppose a bonded-jointed structure is operated at a temperature (40°C) and a frequency (1 Hz). Suppose this structure is under an arbitrary load history, and we can take a load block from the load history, as in Figure 7.3(a). The numbers in this figure represent the shear stresses, which are calculated by

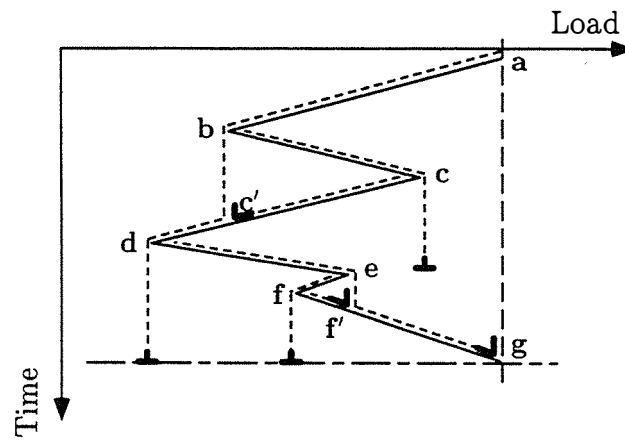
$$\tau = \frac{P}{\pi DL} \quad (7.1)$$

where  $P$  is the load,  $D$  is the diameter of the cast-iron rod and  $L$  is the overlap length of the bonded area in the axial direction. After rainflow cycles counting, we can obtain three cycles with three stress ratios of 0.05, 0.5 and 0.95, as in Figure 7.3(b). Their maximum and minimum stresses with the stress ratios are listed in Table 7.1.

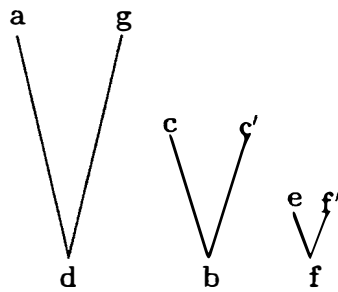
Now we can draw three S-N curves at three stress ratio as follows:



(a) A load block



(b) Trace of rainflow



(c) Counted cycles

Figure 7.2: A sample of a load block and rainflow cycle counting.

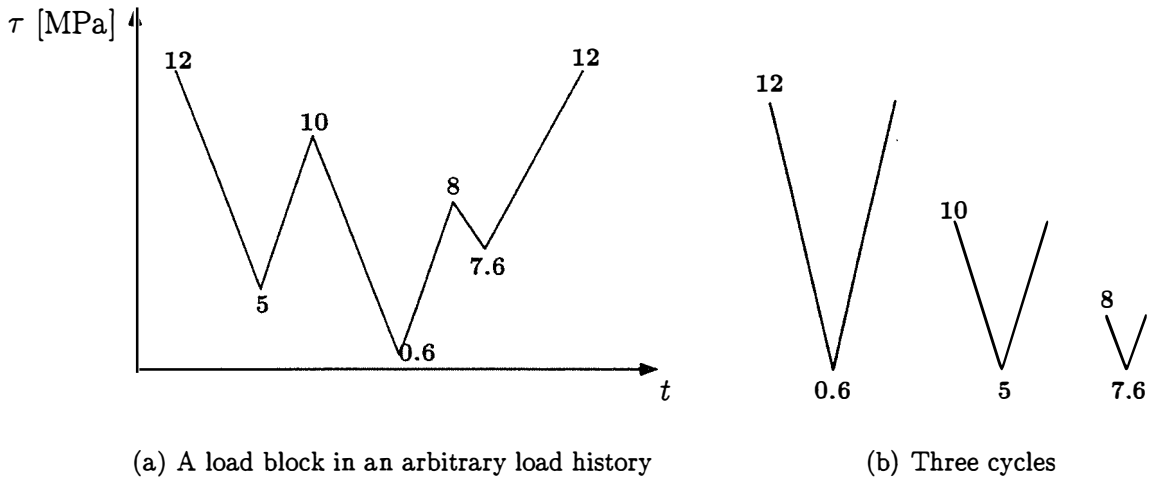


Figure 7.3: An Example of rainflow cycle counting.

1.  $R_\sigma = 0.05 \approx 0$  : At  $f = 1$  Hz and  $T = 40^\circ\text{C}$ , Eq.( 6.1) becomes

$$N_f = t'_f \times f \times a_{T_o}(40^\circ\text{C}) = t'_f \times 1 \times 1 = t'_f \quad (7.2)$$

We can pick points satisfying  $N_f = t'_f$  on the master curve of fatigue strength at zero stress ratio, as in Figure 7.4. By connecting these points, we can obtain a S-N curve at zero stress ratio, as drawn with a dash-dotted line in Figure 7.5.

2.  $R_\sigma = 0.95 \approx 1$  : From the master curve of creep strength in Figure 6.7, we can obtain a S-N curve at unit stress ratio, as drawn with a dotted line in Figure 7.5.
3.  $R_\sigma = 0.5$  : By Eq.( 6.17), a S-N curve at the intermediate stress ratio is drawn with a solid line in Figure 7.5.

In Figure 7.5, horizontal lines starting at each maximum stress level meet the S-N curves at each stress ratio. By reading their  $x$ -axis values, we can obtain three fatigue lives ( $N_f$ ) for the rainflow-counted cycles. The estimated fatigue lives are listed in Table 7.1.

Under an assumption of linear cumulative damage law (Miner's rule), amount of damage to the structure during each  $i$ th load cycle is an inverse of number of cycles to failure, which is  $1/(N_f)_i$ . Then amount of damage during one load block becomes

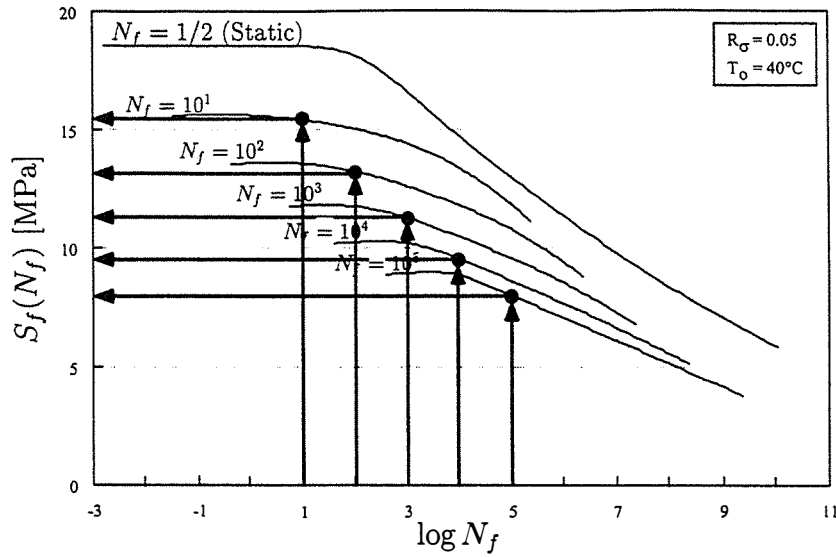


Figure 7.4: Master curve of fatigue strength at zero stress ratio. Solid dots correspond points where  $N_f = t'_f$  at  $f = 1$  Hz.

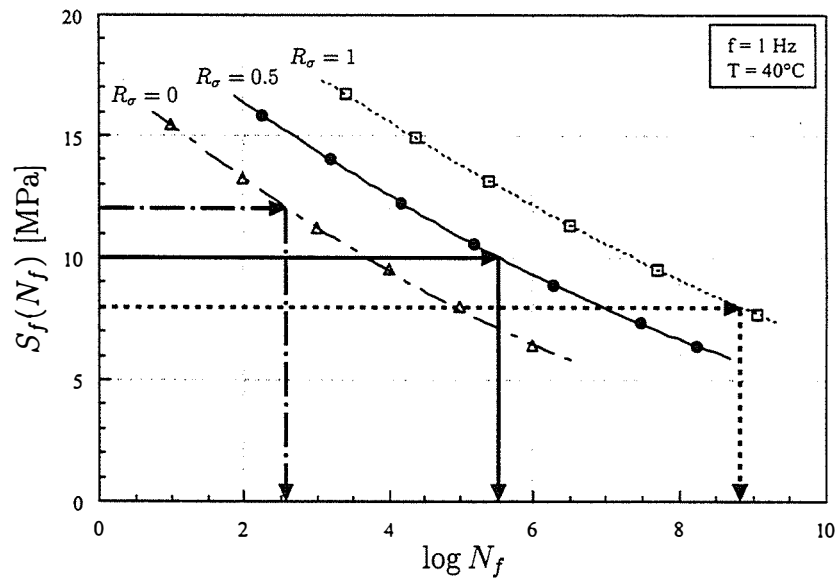


Figure 7.5: Three S-N curves at three stress ratio ( $R_\sigma = 0, 0.5, 1$ ) that are estimated for a case at  $T = 40^\circ\text{C}$  and  $f = 1$  Hz. At each stress ratio, we can obtain lives ( $N_f$ ) of rainflow-counted cycles during a load block.

Table 7.1: Three cycles after rainflow cycles counting.

Cycle	$\tau_{min}$	$\tau_{max}$	$R_\sigma$	$\log N_f$
1	0.6	12	0.05	2.60
2	5	10	0.5	5.52
3	7.6	8	0.95	8.84

a sum of the damage of each cycle in the load block, which leads

$$DM_{block} = \sum_i \frac{1}{(N_f)_i} \quad (7.3)$$

$$= \frac{1}{10^{2.60}} + \frac{1}{10^{5.52}} + \frac{1}{10^{8.84}} \quad (7.4)$$

$$\cong 2.51 \times 10^{-3} \cong \frac{1}{397.6} \quad (7.5)$$

Therefore, we can predict that the structure will fail in 397 load blocks.

# Appendix A

## Viscoelasticity

### A.1 Three descriptions of mechanical behavior

In the mechanics of deformable media, response behavior of an elastic solid is dealt with the realm of the classical theory of elasticity. The most direct description of such response is in accordance with Hooke's law. This law forms the basis of the mathematical theory of elasticity [21]; that is, provided that the occurring deformations are small, the stress is considered to be directly proportional to the strain and independent of the strain-rate. Consequently, such a response is termed as perfectly elastic, or Hookean.

In a simple uni-axial test, the load-deformation curve of the perfectly elastic solid will follow the same path for both increasing and decreasing load. Thus, the material test specimen will regain its original dimensions instantaneously on removal of the load. Under a constant level of loading, the occurring deformation is constant, i.e., time independent. Further, when such a solid is subjected to a sinusoidally oscillating loading, the deformation will also be found to be sinusoidal and practically in phase with the load. All the energy is stored and recovered in each cycle.

On the other hand, the mechanical response of a viscous fluid is dealt with the domain of the classical theory of fluid dynamics. In this case, the most direct description of the response accords with Newton's law, whereby stress is considered to be proportional to the occurring strain-rate but independent of the strain itself. This

occurs when the strain-rate is small. When a Newtonian viscous fluid is subjected to a sinusoidally oscillating load, the deformation will be found to be  $90^\circ$  out of phase with the load.

The classical theories of linear elasticity and Newtonian fluids, though impressively well structured, do not adequately describe the response behavior and flow of most real materials. That is, between the above two described responses of the elastic solid, there are combined response characteristics of these two media. Attempts to characterize the behavior of such real materials under the action of an external phenomenon now labeled *viscoelasticity* are well defined and intended to convey mechanical behavior combining response characteristics of both an elastic solid and a viscous fluid. A viscoelastic material is, thus, characterized by a certain level of rigidity of an elastic solid body, but, at the same time, it flows and dissipates energy by frictional losses as a viscous solid.

When a viscoelastic material is subjected to a constant stress, it does not maintain a constant deformation but continues to flow with time, i.e., it creeps. Immediately, on removal of the load, the specimen is found to have taken an amount of residual strain, the magnitude of which depends on the length of time for which the load is applied and on the level of loading. Following removal of the load, a noticeable reduction in the amount of residual strain gradually takes place with the passage of time. This residual strain may even disappear entirely in the course of time. This phenomenon, which occurs following the removal of the load, is referred to as creep recovery.

A specimen of viscoelastic material, tested as mentioned above, eventually regains its original dimension. Consequently, the creep of such material under load cannot be regarded as a phenomenon of plasticity, as in the case of polycrystalline solids, but rather as a delayed elasticity [22]. In a simple uni-axial test of a viscoelastic material, a load-deformation loop (hysteresis) is obtained, i.e., the descending load curve corresponds to a larger amount of strain than the ascending load curve. Neither of the two curves is completely linear. The shape of the resulting hysteresis loop depends on the magnitude of load, rate of application and removal of the load and temperature.

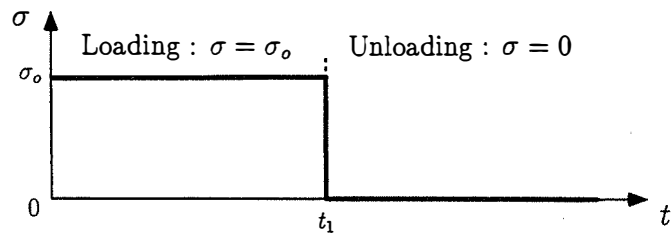


Further, when a viscoelastic material is subjected to sinusoidally oscillating stress, the resulting strain, through sinusoidal, is neither exactly in phase with the stress nor  $90^\circ$  out of phase; it is somewhere inbetween. The magnitude of the strain and the phase angle between the stress and strain are generally frequency- and temperature-dependent. On loading and unloading a viscoelastic material specimen, some of the energy input is stored and recored in each cycle and some of it is dissipated as heat.

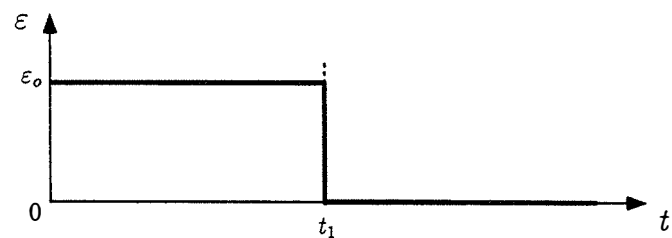
The particular nature of the viscoelastic response considered in the foregoing proves the existence of *passive resistance* in such material. This is in contrast to the instantaneous response and reversibility that usually characterize pure elastic behavior. This passive resistance is of a viscous nature and reflects what is usually called the *hereditary response* of the material. That is, the present state of response depends not only on the present state of loading input but also on the previous states. This property is revealed experimentally in different time-dependent phenomena pertaining to the viscoelastic response, such as creep, stress relaxation and intrinsic attenuation and dispersion of propagating waves.

As discussed above, many engineering materials, such as polymeric and rubber-like materials, and metals at elevated temperatures, flow when subjected to stress or strain. Such flow is accompanied by the dissipation of energy resulting from some internal loss mechanism (for example, bond breakage and bond formation reaction, dislocations, formation of substructures in metals). Materials of this type are viscoelastic in response. The description *viscoelastic* is because of the fact that such materials exhibit both elastic and viscous properties.

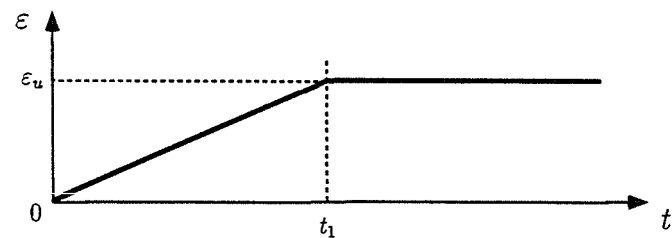
Figure A.1 illustrates the differences in strain response of elastic, viscous and viscoelastic specimens when the three specimens are subjected to a constant stress of unit magnitude. The stress is applied at time,  $t = 0$ , to undisturbed specimens and maintained constant for time duration,  $t_1$ , as Figure A.1(a) shows. As shown in Figure A.1(b), the strain-time response of the elastic specimen has the same form as the applied stress. On application of the load, the strain instantaneously reaches a certain level ( $\epsilon_o$ ) and then remains constant. For the viscous fluid in Figure A.1(c), the material flows at a constant rate and the strain response is proportional to the time. For the viscoelastic specimen in Figure A.1(d), there is a relatively rapid increase in



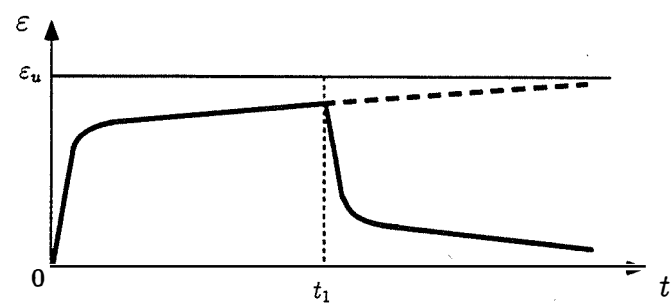
(a) Load input



(b) Elastic response



(c) Viscous response



(d) Viscoelastic response

Figure A.1: Comparison of strain response for elastic, viscous and viscoelastic material specimens under a constant stress of unit magnitude until time,  $t_1$ .

the strain response for small values of time immediately after the application of the load. As  $t$  increases, the slope of the curve decreases, and as  $t \rightarrow \infty$ , the slope may approach zero or finite value provided that the applied stress maintained is constant.

Upon removal of the load at time,  $t_1$ , the strains in the three specimens will recover in the manner shown in Figure A.1. The perfectly elastic solid will recover instantaneously upon removal of the load, as in Figure A.1(b); However, the viscous fluid will not recover, as Figure A.1(c) shows. Meanwhile, upon removal of the load, the viscoelastic specimen will recover its elastic deformation immediately; however, the retarded part of the response will require time for recovery, as in Figure A.1(d).

Under constant stress, the creep strain in viscoelastic material may be divided into the following three components, as shown in Figure A.2:

1. Instantaneous elastic strain,  $\varepsilon_e(0^+)$ . In a polymeric material, for instance, this part of the strain is attributable to bond stretching and bending, including the deformation of weak Van der Waals bonds between the molecular chains. This strain is reversible and disappears on removal of the stress.
2. Delayed elastic strain,  $\varepsilon_d(t)$ . The rate of increase of this part of strain decreases steadily with time. It is also elastic, but, after the removal of the load, it requires time for complete recovery. It is often called primary creep, or elastic aftereffect, among other terms. In a polymeric material, the delayed elastic strain is attributable to, for instance, chain uncoiling.
3. Viscous flow,  $\varepsilon_v(t)$ . It is an irreversible component of strain that may or may not increase linearly with time of stress application. In a polymeric substance, it is characteristic of interchain slipping. It is often referred to as secondary creep of nonrecoverable strain.

On unloading the viscoelastic specimen at  $t_1$ , the instantaneous elastic response recovers immediately and the delayed elastic response recovers gradually, but the viscous flow remains [23].

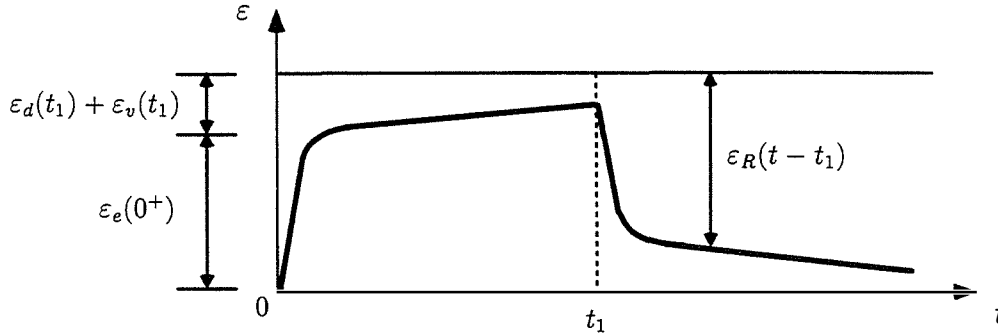


Figure A.2: Creep and recovery of a viscoelastic material specimen subjected to a constant stress of unit magnitude until time,  $t_1$ .

## A.2 Thermoviscoelasticity

The viscoelastic response behavior generally exhibits a very strong dependence on service temperatures. So when one wishes to find the material functions through experiments without making any a priori assumptions about their temperature dependence, we will need a large number of tests for an uni-axial test situation, particularly if the temperature varies in a cyclic or a discrete fashion with time. In this case, one must subject the material specimen to the actual temperature history. This approach turned out to be quite impractical.

There is, however, an experimental evidence which implies that viscoelastic characterization for transient temperature applications may be performed by using tests at a set of different constant temperatures [8]. Hence, the phenomenological viscoelastic response description of a large class of polymeric materials and inorganic glasses under nonisothermal conditions is simplified by the adoption of the so-called *time-temperature equivalence* (also known as the *thermorheologically simple hypothesis*).

Thermorheologically simple materials (TSM) are a special class of viscoelastic materials whose temperature dependence of mechanical properties is particularly responsive to analytical description. This group of materials generally constitutes the simplest and most realistic viscoelastic constitutive equation for which response under

constant temperatures can be used to predict response under transient temperatures.

Following Schapery, the uni-axial creep constitutive relation for thermorheologically simple materials can be expressed as

$$\varepsilon(t) = \int_0^t D_c(t' - \tau) \frac{d\sigma(\tau)}{d\tau} d\tau \quad (\text{A.1})$$

where  $\varepsilon$  is the uni-axial strain due to mechanical stress only (i.e., the total strain less that due to thermal expansion) and  $D_c(t' - \tau)$  is the time- and temperature-dependent creep compliance. In this equation,  $t'$  is called the *shifted time* or *reduced time* parameter and defined by

$$t' = t'(t) = \int_0^t \frac{d\xi}{\partial_{T_o}(\xi)} \quad (\text{A.2})$$

where  $\partial_{T_o} = \partial_{T_o}(T)$  is so-called *time-temperature shift factor*. The latter is dependent on the temperature within the time interval ( $\xi = t' - tau$ ). In the constitutive equation (Eq. (A.1)), it is assumed that  $\sigma = \varepsilon = 0$  when  $t \leq 0$ .

The inverse of Eq. (A.1) (i.e., the relaxation constitutive equation) can be determined by using Laplace transform with respect to shifted time. In this context, it can be shown that

$$\sigma(t) = \int_0^t E_r(t' - \tau) \frac{d\varepsilon(\tau)}{d\tau} d\tau \quad (\text{A.3})$$

where  $E_r(t' - \tau)$  is the time- and temperature-dependent relaxation modulus and the shifted time parameter ( $t'$ ) is as expressed previously by Eq. (A.2).

The experiments for the constitutive equations, Eq. (A.1) and Eq. (A.3), under constant temperature conditions may be performed by considering isothermal creep and isothermal relaxation tests. That is, for the uni-axial creep test ( $\sigma(t) = \sigma_o H(t)$ , where  $\sigma_o$  is the constant stress input and  $H(t)$  is the Heaviside step function), the creep constitutive equation (Eq. (A.1)) yields

$$\varepsilon(t') = D_c(t') \sigma(t)$$

where  $\varepsilon$  is the resulting uni-axial strain due to the stress only. Similarly, for the relaxation test ( $\varepsilon(t) = \varepsilon_o H(t)$ , where  $\varepsilon_o$  is the constant strain input), the relaxation constitutive equation (Eq. (A.3)) yields

$$\sigma(t') = E_r(t')\varepsilon(t)$$

with the understanding that for both types of isothermal tests,

$$t' = \frac{t}{a_{T_o}(T)} \quad (\text{A.4})$$

Eq. (A.4) indicates that the effect of temperature on the mechanical properties,  $D_c(t')$  or  $E_r(t')$ , for a thermorheologically simple material produces only horizontal translations when the property is plotted against  $\log t$ . Conversely, if it is found that the constant-temperature viscoelastic response curves (creep or relaxation) can be superposed so as to form a single curve (master curve) by means of only rigid, horizontal translations, then the associated mechanical property (creep compliance or relaxation modulus) would depend only on time and temperature through the one parameter ( $t'$ ). Such a description is probably a more or less conventional definition of a thermorheologically simple material [8, 24].

# Appendix B

## Rainflow counting

```
%  
% Matlab program for Rainflow Cycle Counting  
%  
  
clear  
  
%  
% input section  
% : Enter magnitudes of peaks and valleys in a load block.  
%  
sNom = [1000 200 800 10 500 400 1000];  
  
%  
% initialize  
%  
sNom2 = [0,sNom];  
delS = [];  
for i = 1:(length(sNom2)-1)  
    delS = [delS, sNom2(i+1)-sNom2(i)];  
end
```

```
ipeak=[];
ivalley=[];
for i = 1:length(delS)-1
    if delS(i) > 0,
        ipeak = [ipeak,i];
    else
        ivalley = [ivalley,i];
    end
end
len = length(ipeak);
cycle = zeros(len,2);

%
% main calculation
%

if ipeak(1) == 1,
    ip = ipeak;
    iv = ivalley;
    isign = 1;
elseif ivalley(1) == 1,
    ip = ivalley;
    iv = ipeak;
    isign = -1;
end

%
% case 1 : if i = 1 (first peak or valley),
%
i=1;
```



```

cycle(i,1) = ip(i);

imax = i;
for j = i+1:len,
    if (-isign * (sNom(iv(imax)) - sNom(iv(j)))) < 0,
        imax = j;
    end
end % end of for j = i+1:len
cycle(i,2) = iv(imax);

%
% case 2 : if i > 1,
%
for i = 2:len,
    cycle(i,1) = ip(i);

    if i < len,
        if (-isign * (sNom(iv(i))-sNom(iv(i-1)))) < 0,
            imax = i;
            for j = i+1:len,
                if (isign * (sNom(ip(i))-sNom(ip(j)))) < 0,
                    break
                else % if (isign * (sNom(ip(i))-sNom(ip(j)))) >= 0,
                    if (-isign * (sNom(iv(imax)) - sNom(iv(j)))) < 0,
                        imax = j;
                    end
                end
            end
        end % end of for j = i+1:len
        cycle(i,2) = iv(imax);
    end
end

```

```

else % if (-isign * (sNom(iv(i))-sNom(iv(i-1)))) ) >= 0
  for j = i-1:-1:1,
    cycle(i,2) = iv(j);
    for k = 1:i-1,
      if cycle(i,2) == cycle(k,2),
        iflag = 0;
        break
      else
        iflag = 1;
      end
    end
  end

  if iflag == 1,
    break
  end

end % end of for j = i-1:1
end % end of if (-isign * (sNom(iv(i))-sNom(iv(i-1)))) ) < 0,

%
% case 3 : if i == ien (last peak or valley)
%
elseif i == len
  if (-isign * (sNom(iv(i))-sNom(iv(i-1)))) ) < 0
    cycle(i,2) = iv(i);
  else
    for j = i-1:-1:1,
      cycle(i,2) = iv(j);
    for k = 1:i-1,
      if cycle(i,2) == cycle(k,2),
        iflag = 0;

```

```
        break
    else
        iflag = 1;
    end
end

if iflag == 1,
    break
end

end % end of for j = i-1:1
end % end of if (-isign * (sNom(iv(i))-sNom(iv(i-1)))) < 0

end % end of if i < len
end % end of for i = 2:len
end % end of if ip(1)==1

%
% print and save rainflow-counted cycles
% : numbers represent order of peaks and valleys of the input load block.
%
cycle = [cycle, cycle(:,1)]
save cycles.out cycle -ascii
```

# Bibliography

- [1] R. D. Adams and N. A. Peppiatt. Stress analysis of adhesive bonded tubular lap joints. *Journal of Adhesion*, 9(1):1–18, 1977.
- [2] D. Chen and S. Cheng. An analysis of adhesively-bonded single-lap joints. *Journal of Applied Mechanics*, 50:109–115, 1983.
- [3] J. D. Whitcomb and K. Woo. Analysis of debond growth in tubular joints subjected to tension and flexural loads. *Computers and Structures*, 46(2):323–329, 1993.
- [4] T. R. Guess and R. Tommy. Testing composite-to-metal tubular lap joints. *Journal of Composites Technology and Research*, 17(2):117–124, 1995.
- [5] E. D. Reedy Jr. Composite-to-metal tubular lap joints: Strength and fatigue resistance. *International Journal of Fracture*, 63(4):351–367, 1993.
- [6] J. K. Choi. Experimental investigation of the static torque transmission capabilities of the adhesively bonded single lap joints. *Journal of Materials Processing Technology*, 48(1-4):341–347, 1995.
- [7] W. T. Kim. Torque transmission capabilities of adhesively bonded tubular lap joints for composite drive shafts. *Composite Structures*, 30(2):229–240, 1995.
- [8] R. A. Schapery. *Viscoelastic behavior and analysis of composite materials*, in *Mechanics of Composite Materials*. Academic Press, New York, 1974.

- [9] M. K. McMurray. *The Time and Temperature Dependencies of Flexural Strength of CFRP Composites*. PhD thesis, Kanazawa Institute of Technology, March 1995.
- [10] R. F. Landel M. L. Williams and J. D. Ferry. The temperature dependence of relaxation mechanisms in amorphous polymers and other glass-forming liquids. *Journal of the American Chemical Society*, 77:3701–3707, 1955.
- [11] J. Gittus. *Creep, Viscoelasticity and Creep Fracture in Solids*. Wiley, New York, 1975.
- [12] James M. Gere and Stephen P. Timoshenko. *Mechanics of Materials*. Brooks/Cole Engineering Division, Monterey, CA, 1984.
- [13] J. N. Yang and M. D. Liu. Residual strength degradation model and theory of periodic proof tests for graphite/epoxy laminate. *Journal of Composite Materials*, 11:176–203, 1977.
- [14] J. N. Yang. Fatigue and residual strength degradation for graphite/epoxy composites under tension-compression cyclic loadings. *Journal of Composite Materials*, 12:19–39, 1978.
- [15] J. N. Yang and S. Du. An exploratory study into the fatigue of composites under spectrum loading. *Journal of Composite Materials*, 17(6):511–526, 1983.
- [16] H. T. Hahn and R. Y. Kim. Proof testing of composite materials. *Journal of Composite Materials*, 9:297–311, 1975.
- [17] H. T. Hahn and R. Y. Kim. Fatigue behavior of composite laminate. *Journal of Composite Materials*, 10:156–180, 1976.
- [18] K. Radhakrishnan. Fatigue and reliability evaluation of unnotched carbon epoxy laminates. *Journal of Composite Materials*, 18(1):21–31, 1984.
- [19] N. E. Dowling. Fatigue failure predictions for complicated stress-strain histories. *Journal of Materials*, 7(1):71–87, 1972.

- [20] S. D. Downing and D. F. Socie. Simplified rainflow counting algorithms. *International Journal of Fatigue*, 4(1):31–40, 1982.
- [21] A. E. Love. *A Treatise on the Mathematical Theory of Elasticity*. Dover Publications, New York, 1944.
- [22] H. Leaderman. *Elastic and Creep Properties of Filamentous and Other High Polymers*. Textile Foundation, Washington, DC, 1943.
- [23] I. M. Ward. *Mechanical Properties of Solid Polymers*. Wiley, New York, 1983.
- [24] Y. M. Haddad. *Viscoelasticity of Engineering Materials*. Chapman and Hall.

# REPORT DOCUMENTATION PAGE

*Form Approved*  
OMB NO. 0704-0188

Public reporting burden for this collection of information is estimated to average 1 hour per response, including the time for reviewing instructions, searching existing data sources, gathering and maintaining the data needed, and completing and reviewing the collection of information. Send comments regarding this burden estimate or any other aspect of this collection of information, including suggestions for reducing this burden, to Washington Headquarters Services, Directorate for Information Operations and Reports, 1215 Jefferson Davis Highway, Suite 1204, Arlington, VA 22202-4302, and to the Office of Management and Budget, Paperwork Reduction Project (0704-0188), Washington, DC 20503.

1.	2. REPORT DATE July 1997	3. REPORT TYPE AND DATES COVERED Subcontractor Report	
4. TITLE AND SUBTITLE  Time- and Temperature-Dependent Failures of a Bonded Joint		5. FUNDING NUMBERS  C: XAF-4-14076-01  TA: WE711210	
6. AUTHOR(S)  Sangwook Sihm, Yasushi Miyano, Stephen W. Tsai		8. PERFORMING ORGANIZATION REPORT NUMBER	
7. PERFORMING ORGANIZATION NAME(S) AND ADDRESS(ES)  Stanford University Department of Aeronautics and Astronautics Palo Alto, California 94503-4035		10. SPONSORING/MONITORING AGENCY REPORT NUMBER  SR-440-22708	
9. SPONSORING/MONITORING AGENCY NAME(S) AND ADDRESS(ES)  National Renewable Energy Laboratory 1617 Cole Blvd. Golden, CO 80401-3393		11. SUPPLEMENTARY NOTES NREL Technical Monitor: Gunjit Bir	
12a. DISTRIBUTION/AVAILABILITY STATEMENT National Technical Information Service U.S. Department of Commerce 5285 Port Royal Road Springfield, VA 22161		12b. DISTRIBUTION CODE  UC-1210	
13. ABSTRACT ( <i>Maximum 200 words</i> ) This report covers time- and temperature-dependent behaviors of a tubular lap bonded joint to provide a design methodology for windmill blade structures. The tubular joint bonds a cast-iron rod and a GFRP composite pipe together with an epoxy type of an adhesive material containing chopped glass fibers. We proposed a new fabrication method to make concentric and void-less specimens of the tubular lap joint with a thick adhesive bondline in order to simulate the root bond of a blade. For a better understanding of the behavior of the bonded joint, we studied viscoelastic behavior of the adhesive materials by measuring creep compliance of this adhesive material at several temperatures during the loading period. We also performed constant-rate of monotonically increased uniaxial tensile tests to measure static strength of the tubular lap joint at several temperatures and different strain-rates. We also performed fatigue tests by applying uniaxial tensile-tensile cyclic loadings to measure fatigue strength of the bonded joint at several temperatures, frequencies, and stress ratios, and to show their dependency. We can estimate the fatigue life of the bonded joint at any load levels at any frequency and temperature with a certain probability. A numerical example shows how to apply the life estimation method to a structure subjected to an arbitrary load history by using rainflow cycle counting.			
14. SUBJECT TERMS  Key words: wind energy, blades		15. NUMBER OF PAGES	
17. SECURITY CLASSIFICATION OF REPORT Unclassified		16. PRICE CODE	
18. SECURITY CLASSIFICATION OF THIS PAGE Unclassified		19. SECURITY CLASSIFICATION OF ABSTRACT Unclassified	
20. LIMITATION OF ABSTRACT  UL			